Spintronics using C_{60} fullerenes: Interface and devices

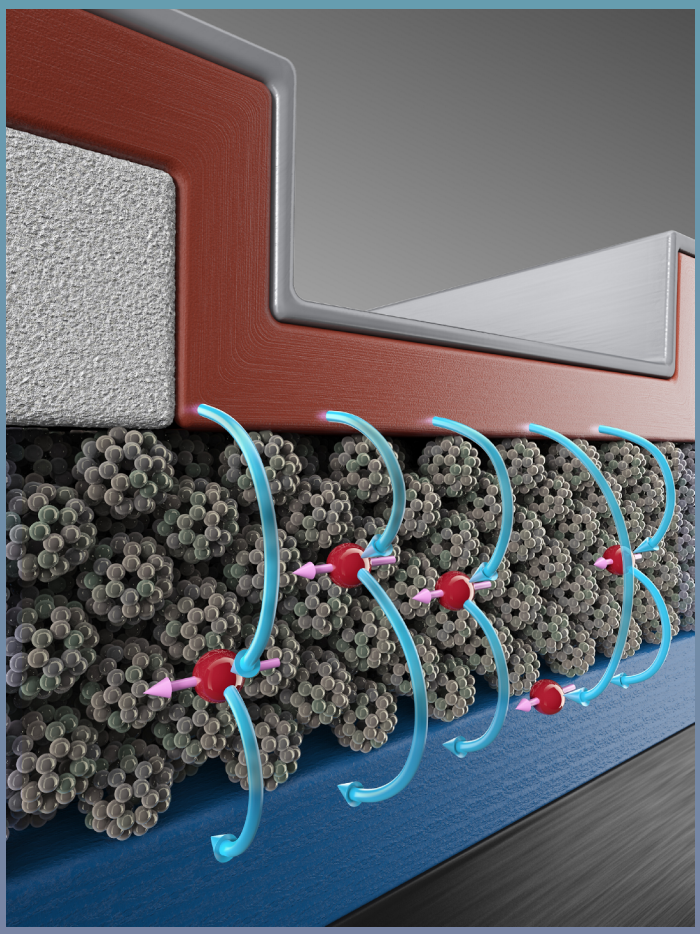

Trần Thị Lan Anh

Spintronics using C_{60} fullerenes: Interface and devices

Trần Thị Lan Anh

Graduation Committee

Chairman and Secretary:

Prof.dr.ir. A. J. Mouthaan	University of Twente

Promotor:

Prof.dr.ir. W.G. van der Wiel	University of Twente

Assistant promotor:

Dr.ir. M.P. de Jong	University of Twente

Members:

Prof.dr. L.E. Hueso	CIC nanoGUNE Consolider, Spain
Prof.dr. B. Koopmans	Eindhoven University of Technology
Prof.dr.ir. E.J. ten Elshof	University of Twente
Prof.dr.ir. A. Brinkman	University of Twente

The research described in this thesis was carried out at the NanoElectronics group at the MESA+ Institute for Nanotechnology, University of Twente, the Netherlands. The project was financially supported by the European project MINOTOR (grant no. FP7-NMP-228424), the NWO VIDI program (grant no. 10246) and the European Research Council (ERC Starting Grant no. 280020).

Printed by Wöhrmann Print Service, Zutphen, the Netherlands, 2013.

ISBN: 978-90-365-1225-1

DOI: 10.3990./1.9789036512251

SPINTRONICS USING C_{60} FULLERENES: INTERFACES AND DEVICES

DISSERTATION

to obtain

the degree of doctor at the University of Twente,

on the authority of the rector magnificus,

prof. dr. H. Brinksma,

on account of the decision of the graduation committee,

to be publicly defended

on Wednesday 4 December 2013 at 16.45

by

Trần Thị Lan Anh

born on 3 August 1980

in Ha Tinh province, Vietnam

This dissertation has been approved by

The promotor: Prof. dr. ir. W. G. van der Wiel

The assistant promotor: Dr. ir. M. P. de Jong

To my parents, parents in law

My beloved husband, my son and my daughter.

Con kính tặng bố mẹ

Tặng chồng yêu và hai con.

CONTENTS

1 Introduction **1**
1.1 Spintronics 2
1.1.1 A brief historical perspective 2
1.1.2 Spin dependent tunnelling 3
1.1.3 Semiconductor spintronics 5
1.1.3.1 Spin injection into semiconductors 7
1.1.3.2 Conductivity mismatch 8
1.1.4 Organic semiconductor spintronics (carbon-based spintronics) 8
1.1.5 Spin relaxation 10
1.2 Ferromagnetic/organic interfaces 12
1.3 Outline of the thesis 13
References 14

2 Experimental methods **19**
2.1 Fabrication techniques and measurement setup 20
2.1.1 Molecular beam epitaxy system 20
2.1.2 Fabrication of C_{60}-based spin valves 21
2.1.3 Magnetotransport measurements 23
2.1.4 Deposition of epitaxial bcc-Fe and C_{60}/bcc-Fe films on MgO substrates 25
2.1.5 Scanning tunneling microscopy 26
2.1.6 Atomic force microscopy 28
2.2 Synchrotron radiation techniques 31
2.2.1 Beamline D1011 at MAX-Lab, Lund, Sweden 31
2.2.2 Photoemission spectroscopy 33
2.2.3 X-ray absorption spectroscopy 37
2.2.4 X-ray magnetic circular dichroism 39
References 41

3 The multi-step tunnelling analogue of conductivity mismatch in organic spin valves **43**
3.1 Introduction 44
3.2 Experiments 45
3.3 Multi-Step Tunnelling Calculations 46
3.3.1 Spin Polarized Tunnelling via an Intermediate State 46
3.3.2 Tunnelling via a Gaussian DOS of Intermediate States 50
3.3.3 Tunnelling via Multiple Intermediate States 52
3.3.3.1 Multiple equidistant tunnelling sites 53
3.3.3.2 Interfacial Tunnelling Sites Connected via a Large Number of Uncorrelated Hops 56
3.4 Magnetotransport experiment results 56

3.4.1 Resistance and JMR versus C_{60} Thickness 56
3.4.2 Temperature Dependence of the Resistance and JMR 62
3.4.3 Bias Voltage Dependent Properties 66
3.5 Conclusions 69
References 70

4 Hybridization-induced oscillatory magnetic polarization of C_{60}-orbitals at the C_{60}/Fe(001) interface 73
4.1 Introduction 74
4.2 Experiments 75
4.3 Results and discussion 76
4.3.1 Electronic structure of C_{60} on Fe(001) 76
4.3.2 The C_{60}-Fe interaction: the hybridization effect at the C_{60}/Fe(001) interface. 82
4.4 Conclusions 87
References 87

5 Magnetic properties of bcc- Fe(001)/C_{60} interfaces for organic spintronics 89
5.1 Introduction 90
5.2 Computational results 91
5.3 Experimental results 94
5.3.1 Sample preparation 94
5.3.2 Spin and orbital magnetic moments of Fe 95
5.4 Discussion 99
5.5 Conclusions 101
References 102

6 Highly ordered C_{60} films on epitaxial Fe/MgO(001) surfaces for organic spintronics 105
6.1 Introduction 106
6.2 Experimental methods 107
6.3 Results and discussion 108
6.3.1 Structural characterization by X-ray diffraction 108
6.3.2 Surface morphology and molecular ordering by scanning tunnelling microscopy 111
6.4 Conclusion 115
References 116

Summary 119

Samenvatting 123

Acknowledgements 127

List of publications 133

CHAPTER 1

Introduction

This introduction presents the main concepts of the emerging field "organic spintronics", which aims to combine advantages of two very successful new technologies, organic electronics and spintronics. The discussion focuses on device concepts, and interface characterization. A brief history of spintronics and the related physical mechanisms are described, to introduce the concepts and challenges of semiconductor-based spintronic devices. We discuss the selection of appropriate carbon-based organic- or, more generally, carbon-based materials (including C_{60} fullerenes) for spintronic applications, and the advantages of using well-defined ferromagnet/organic interfaces in organic spin valves.

1.1 Spintronics

1.1.1 A brief historical perspective

Nowadays, the electronics industry is developing rapidly, as is evidenced in the growing abundance of small, light, fast and low-power electronic devices such as smart phones, digital cameras, laptop computers, etc. In spite of this rapid development, these electronic devices only exploit the most well-known property of electrons (and holes): the electric charge. The operation of such devices is thus based on the transport, manipulation and storage of electrical charge, while other degrees of freedom, such as the spin or valley index, are ignored.

Most of the industry's effort is put in reducing the dimensions of electronic components (e.g. metal oxide field effect transistors (MOSFETs), diodes, capacitors, and bipolar transistors). This improves the costs/performance ratio of integrated circuits, and makes the performance of some devices faster and more efficient. It is clear that this approach cannot continue indefinitely, however, since the device dimensions will reach physical limits eventually. Therefore, alternative solutions are being developed in parallel, including finding entirely new devices with new functionalities.

Spintronics (also called "spin electronics") is a developing field of electronics, based on the spin of electrons.[1] The best known example of a spintronic application is the read head sensor in hard disk drives,[2] based on the giant magnetoresistance (GMR) effect in ferromagnetic multilayers, discovered independently by the Fert group in 1988[3] and the Grunberg group in 1989.[4] The word “giant” is used to distinguish GMR from the anisotropic MR (AMR) effect, found in bulk ferromagnetic metals by William Thomson (known as Lord Kelvin) in 1851.[5] The AMR effect refers to the dependence of the electrical resistance on the angle between the direction of electrical current flow and the orientation of the magnetic field. In contrast, GMR was found in multilayer stacks comprised of very thin layers of ferromagnetic metals (FMs) separated by non-magnetic metals (NMs), which allows electron transport across different layers without being scattered or flipping their spin. When the layer stacks are properly engineered, the GMR effect is much larger than AMR.

With the discovery of GMR, *spin-polarized transport* through a non-magnetic (NM) metal was demonstrated, and the revolution of the field of “spintronics” had begun. The first GMR device, also called “*spin valve”*, was

invented.[6] The spin valve consists of two FM layers with different coercive fields (H_c) separated by a NM interlayer. The NM interlayer is thick enough to decouple the two FM layers magnetically, but thin enough to allow electrons to travel from one FM layer to the other without being scattered. The magnetization of one FM layer is pinned, typically by coupling it to an antiferromagnetic layer resulting in exchange bias, while the magnetization of the layer with smaller H_c can be changed by a small magnetic field. Hence, the magnetization orientation of two FM layers can be changed, for example to be in an antiparallel (AP) or parallel (P) configuration, using a magnetic field. The electrical resistance depends on the relative orientation of the magnetization of two FM layers, due to the different scattering rates for majority versus minority electrons in FMs. The difference in resistance between the AP and P configurations is referred to GMR effect.

Very large MR effects (up to 600% at room temperature[7]) can be observed in *tunnel junctions*, due to spin-polarized tunnelling.[8] Room temperature tunnel magnetoresistance (TMR) has been obtained first by Moodera *et al.* for magnetic tunnel junctions (MTJs), which consist of two ferromagnetic layers separated by a thin insulating tunnel barrier.[9] The large attainable TMR makes MTJs promising candidates for the commercialization of magnetoresistive random access memory (MRAM).[10] The development of MRAM got a strong boost since the discovery of spin transfer torque (STT),[11, 12] which has led to a new generation of MRAM, spin-torque MRAM (ST-MRAM) which was launched in November 2012 by Everspin technologies.[13] STT allows for switching the magnetization of a nanoscale FM by a spin polarized *current* instead of a magnetic field, leading to a vastly improved scalability.

1.1.2 Spin dependent tunnelling

Tunnelling is a quantum mechanical effect. If two metal layers are separated by a very thin insulating film, an electrical current may pass between the metal electrodes upon applying a potential. Electrons have not only particle- but also wavelike properties, and the electron wave function does not vanish immediately at the metal/insulator interface. If the barrier is thin enough, there is a probability for the electron to move through the barrier, which is called tunnelling. The tunnel rate for carriers at a certain energy level is dependent on the product of the carrier densities of states (DOS) in both electrodes at that energy.

Spin dependent tunnelling occurs in a magnetic tunnel junction, (MTJ), where two ferromagnetic electrodes are separated by a thin insulating layer. Spin-polarized carriers from the first electrode can pass through the tunnel barrier and reach the second electrode. Typically, a change in tunnel resistance occurs depending on the relative magnetization orientation of the FM electrodes. This can be understood as follows. A schematic illustration of spin polarized tunnelling in a MTJ is shown in Fig. 1.1.[14] Because of the spin dependent DOS in a ferromagnet due to the exchange interaction, and the spin conservation during tunnelling (electrons can only tunnel from a given spin sub-band in FM1 to the *same* spin sub-band in FM2), the current in the parallel (*P*) configuration (Fig. 1.1a) is (in most cases) higher than in the anti-parallel (*AP*) configuration (Fig. 1.1b).

According to the Jullière model,[15] which was in part based on earlier work by Tedrow and Meservey,[8] the tunnel magnetoresistance (TMR) is obtained by:

$$TMR = \frac{R_{AP} - R_P}{R_P} = \frac{G_P - G_{AP}}{G_{AP}} = \frac{2P_1P_2}{1 - P_1P_2}, \tag{1.1}$$

where $R_{P(AP)}$ is the resistance in the *P* or *AP* configuration, $G_{P(AP)}$ the conductance, and $P_{1(2)}$ the polarization of electrode 1 and electrode 2. The polarization of the FM electrodes is defined as:

$$P_i = \frac{N_{imaj}T_{imaj} - N_{imin}T_{imin}}{N_{imaj}T_{imaj} + N_{imin}T_{imin}}, i = 1,2. \tag{1.2}$$

In equation (1.2) the N_{imaj}, N_{imin} are the number of majority- and minority-spin electrons at the Fermi level, and T_{imaj}, T_{imin} are their transmission probabilities. Even though the (oversimplified) Jullière model may provide a crude physical insight into the origin of the TMR effect, however, it cannot explain the experimental observations. A number of more detailed theoretical descriptions of spin dependent tunnelling have been developed, e.g, by Slonczewski.[16] This model considers important parameters such as the barrier height and barrier width,[17] but cannot explain well the temperature (*T*) and voltage (*V*) dependence of the TMR. Moodera *et al.*,[18] reported that the *T*- dependence of TMR is due to the *T*-dependent surface magnetization of the FM electrodes, while the *V*-dependence is attributed to the creation of magnetic excitations (magnons). The latter produces

spin scattering at the interfaces, leading to the loss of spin signal and reduction of the TMR. In addition, localized electronic defects in the insulating barrier may cause the tunnelling process to proceed not in a direct way (direct tunnelling), but via trap states inside the barrier (two-step tunnelling), reducing the spin polarization of the current and thus the TMR.[19]

A high quality of the tunnel barrier and the FM/insulator interface are required to minimize the *T*- and *V*- dependence of the TMR. Furthermore, very large TMR values can be obtained in crystalline structures, for example CoFeB/MgO/CoFeB spin valves in which a TMR up to 600% at room temperature was obtained.[7] Theoretical studies have shown that the crystalline MgO barrier, in epitaxial structures containing body-centered-cubic Fe, Co, or CoFe films, gives rise to large TMR values, due to the different decay rates of evanescent states in the barrier with different symmetry, leading to a very effective spin-filter effect.[20]

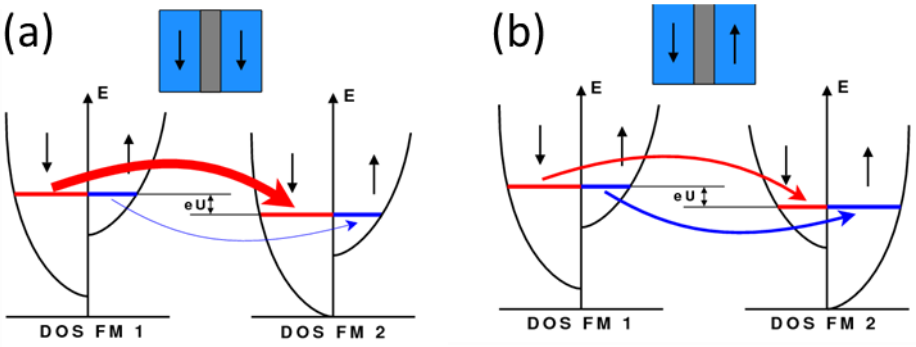

Figure1.1 Schematic illustration of a MTJ, consisting of two FM materials (blue) separated by an insulator (dark grey). (a) parallel and (b) anti-parallel orientation of magnetizations, and the corresponding spin-split sub-bands of the FM materials. Arrows in the two FM regions (upper part of figure) depict the spin orientation of the majority sub-bands, the red and blue curved arrows (lower part) depict the spin conservation. (Ref. 14)

1.1.3 Semiconductor spintronics

Besides metal-based spintronics, semiconductor-based spintronics[21] is also being developed, which combines the functions of semiconductors and ferromagnets. Since semiconductors allow for tuning of the charge carrier concentration via chemical doping or electric field gating, their conductivity can be varied over a large range, making them highly versatile electronic materials. Ferromagnetic materials may serve as a source of spin polarized carriers, to be

injected into the semiconductor. Since ferromagnets typically retain their magnetization for very long times, they may provide non-volatile memory functionality at room temperature. One of the most pursued applications of semiconductor spintronics is to realize a three terminal devices, spin transistors, based on the spin dependent transport in a semiconductor channel with ferromagnetic source- and drain contacts. One of such devices is the spin-MOSFET.[22] However, to realize a spin MOSFET, there are many challenges, for instance, (1) the injection of spin-polarized carriers from a ferromagnet into a semiconductor, (2) transport of such spin polarized carriers through the semiconductor channel without losing their spin orientation, and (3) detection of the spin polarization of the carriers at the drain contact. An obstacle for challenge (1), concerning spin injection from a ferromagnet into a semiconductor, is the conductivity mismatch problem.[23] The conductivity of the FM metal is usually much higher than that of a semiconductor. If the resistance of the device is dominated by the semiconductor channel, the potential drops almost entirely over the semiconductor, leading to a negligible spin polarization of the current. Nowadays, solutions for the conductivity mismatch problem in FM/semiconductor structures have been found, such as the introduction of a large spin-dependent interface resistance.[24, 25] Challenge (2) is to let the injected spins survive for sufficiently long times and travel far enough to transport information from the injection point to the point of detection. This is a significant challenge, since the spin transport is limited by the processes of spin relaxation and spin dephasing. These processes arise from the spin-orbit and hyperfine interactions (which produce spin flips/rotations) which gives an irreversible time evolution of the spin polarization. The spin-orbit interaction is proportional to Z^4 (Z is the atomic number). Therefore in organic semiconductors (OSCs) or carbon-based materials (with small Z) this interaction is much weaker than that in conventional inorganic semiconductor. This aspect makes OSCs particularly interesting for spintronics, since the spin polarization of the carriers can be maintained for long time($\sim$1μs).[26] Finally, challenge (3) regarding the detection of the spins at the drain contact, is perhaps the most difficult to solve. The spin polarization in the semiconductor can be measured electrically,[27] relying on spin-splitting of the chemical potential (spin accumulation). However, the detection of a pure spin valve effect is far from trivial, and depends on the specific electronic band structure and the properties of the interface. In many cases, MR effects come from spurious effects, e.g. Lorentz MR,[28] or magneto Coulomb effects.[29] To detect the pure spin accumulation, the

non-local geometry has been developed.[30] This geometry is unsuited, however, for the realization of a three terminal spin-MOSFET.

1.1.3.1 Spin injection into semiconductors

Consider a prototypical spin injection device, in which two FM electrodes are separated by a semiconductor (SC) spacer. An external magnetic field is used to switch the relative magnetic orientation of the FM electrodes from P to AP, or vice versa. Under certain conditions,[25] such a device may show a different resistance for these two configurations.

In contrast with the magnetic tunnel junctions (MTJs) discussed above, where the spin-polarized carriers pass through the barrier via tunnelling and the TMR scales with the spin asymmetry of the DOS of the FM electrodes, the MR depends on the spin polarization generated in the SC and the spin diffusion length and the thickness of the SC. Fert and Jaffres proposed a spin accumulation model in FM/SC/FM structures in the diffusive transport regime with the flat band approximation (treating the semiconductor as a low conductivity nonmagnetic metal). They showed that the MR can be significant within a fairly narrow range of device- and materials parameters, when introducing a spin dependent resistance (e.g. an insulating (I) tunnel barrier) between FM and SC.[25] The MR of such a system (FM/I/SC/I/FM) is given by Eq. (23) and (25) of Ref.[25], in which the resistance difference (ΔR) between the P and AP configurations saturates to a maximum value, while the resistance of the P configuration (R^P) increases exponentially with the tunnel barrier thickness. The maximum MR is given by:

$$\left[\frac{\Delta R}{R^P}\right]^{MAX} = \frac{\gamma^2}{1-\gamma^2}, \tag{1.3}$$

where γ is the spin asymmetry coefficient of the interface resistance. A significant MR can be obtained in the following range [25]:

$$r_N \frac{t_N}{l_{sf}^N} < r_b^* < r_N \frac{l_{sf}^N}{t_N}, \tag{1.4}$$

where $r_N$is the resistivity of the SC, r_b^* is the interface resistance, l_{sf}^N is the spin diffusion length in the SC, and t_N is the SC channel length. This range depends strongly on channel length, the shorter the channel length the wider the range.

1.1.3.2 Conductivity mismatch

As already mentioned, the conductivity mismatch between FMs and semiconductors forms a limitation for spin injection from a FM into a semiconductor.[23] The conductivity of a semiconductor is usually much lower than that of a metal. Consequently, in a spin valve consisting of two ferromagnetic contacts and a semiconductor channel, the resistance of the device is dominated by the resistance of the semiconductor, which is independent of the carrier spins. Therefore, the resistance change due to the different magnetization orientation in the FM layers is negligible (if no special measures are taken). Several solutions have been used to overcome this problem: (1) using half-metallic FM materials, e.g. LSMO, such that the polarization of the injected current reaches 100% and the MR is recovered,[31] (2) by introducing a large spin-dependent resistance at the interface, e.g. by inserting a tunnel barrier between FM and semiconductor,[24, 25] or (3) by using a ferromagnetic semiconductor as a source/sink for spin polarized carriers, such as Mn-doped GaAs.[32] By using spin tunnel contacts, a robust spin polarization in silicon has been successfully created and detected at room temperature.[33]

1.1.4 Organic semiconductor spintronics (carbon-based spintronics)

Besides the effort in inorganic semiconductor spintronics, organic and carbon-based materials nowadays play an important role in the spintronics community. Organic materials have many advantages, such as mechanical flexibility, chemical tunability, relatively low production costs, and, most important for spintronic applications, potentially very long spin life times.[34, 35] The latter is due to the weak spin-obit coupling intrinsic to these carbon-based materials. In addition, organic semiconductors offer non-stringent requirements for interface formation and film growth, e.g. they can be grown easily on top of ferromagnetic thin films, in contrast to inorganic semiconductors. Therefore, vertical spin valves may be fabricated, with the organic layer sandwiched between two ferromagnetic contacts. Large MR effects have been reported in such carbon-based vertical spin valves,[36] comprising thin films of organic molecules[37] and C_{60} fullerenes.[38-40]

The first report that suggested spin injection into an organic semiconductor was published in 2002 by Dediu *et al.*[41] The device consisted of two LSMO electrodes separated by a sexithienyl (T_6) layer in a lateral geometry. Since the coercive field of the two LSMO electrodes was the same, the magnetization could not be switched from P to AP, rather, the MR of ~30% was estimated based on the different resistance between a random (demagnetized) and P magnetization orientation. By performing experiments on devices with different channel widths, the authors also estimated that the spin relaxation length was about 200 nm, and the spin relaxation time about 1μs. In 2004, Xiong et al.,[36] fabricated the first vertical spin valve based on Alq_3 as a spacer between two FM electrodes, LSMO and Co. The MR was found to be about -40% at 11K, and the spin relaxation length was estimated to be 45 nm. One point to be noted here is that the FM/organic interface, which is discussed in more detail in section 1.2 of this chapter, plays an important role in the device characteristics.[42, 43] The Co/Alq_3 interface in Xiong's device was quite ill-defined, due to interdiffusion/clustering of Co in Alq_3 during growth of the top electrode, and possible pinholes in the Alq_3 layer. The Co/organic interface was later improved by Dediu *et al.*[37] In their devices, with composition LSMO/Alq_3/tunnel barrier/Co, a tunnel barrier (Al_2O_3 or LiF) between Co electrode and Alq_3 was introduced to get a better-defined interface, and room temperature MR was obtained.

The electronic properties of organic semiconductors are rather different than those of inorganic semiconductors. Electrical conduction in (disordered) organic materials normally results from carrier hopping between localized states (molecular orbitals) while in inorganic semiconductors the charge transport typically results from delocalized states (bands). Therefore, theories developed to describe spin-polarized transport mechanisms (spin tunnelling, spin injection, spin relaxation and spin dephasing and the conductivity mismatch problem) in inorganic semiconductor often cannot be applied directly to organic materials. Consequently, the physics underlying spin-polarized transport in organic devices remains somewhat elusive. The motivation of the present work is to shed light on these issues. Due to the lack of hydrogen atoms, C_{60} fullerene is a good candidate for spintronic devices, since hyperfine interactions are very weak (^{12}C, abundance 99%, has no nuclear spin), and high quality thin films can be obtained easily be thermal vapour deposition. Recently reported work on C_{60}-based spin valves (including our own)[38-40] indicates that spin injection in organic spin-valves is limited by a mechanism that is somewhat similar to conductivity mismatch. An

important question here is how spin relaxation and dephasing take place in organic materials, and how it affects the MR. The work by Bobbert *et al*.[44] indicates that the spin precession in the random hyperfine fields of hydrogen nuclei relaxes the spins. This model has been invoked in the context of organic spin valves by Schoonus *et al*.,[45] who suggested that it affects the shape of the MR-versus-field traces. However, this mechanism is expected to be negligible in C_{60} devices, due to the fact that the hyperfine interaction in C_{60} is very weak, as mentioned above. The role of the spin orbit coupling remains less clear. Recent calculations by Yu [46] suggest that spin–orbit coupling, rather than hyperfine coupling, may be mainly responsible for spin relaxation in organic materials.

1.1.5 Spin relaxation

In this section, we will discuss the spin relaxation length and spin relaxation time in semiconductors. The operation of spintronic devices is dependent on the robustness of injection, storage and/or transport of spin polarization. Therefore, besides the spin injection efficiency, the spin relaxation length and -time are important parameters for device performance. The spin relaxation length depends on the carrier mobility and the spin relaxation time.
The spin relaxation length,l_s, is given by [25]

$$l_s = \sqrt{\frac{k_B T \tau_s}{2e^2 \rho_N}} \tag{1.5}$$

Here k_B is the Boltzmann constant, T the temperature, τ_s the spin relaxation time, e the electron charge, n the total number of carriers, and $\rho_N$the resistivity of the SC.
One can distinguish two classes of spin relaxation. The spin relaxation time T_1 is defined as the time it takes for the spins along the longitudinal field direction (up/down quantization axis) to reach equibrium. Therefore, T_1 is related with the relaxation of the average spin polarization. This T_1 can be written as

$$\frac{1}{T_1} = \frac{1}{\tau_{\uparrow\downarrow}} + \frac{1}{\tau_{\downarrow\uparrow}} \tag{1.6}$$

where $\tau_{\uparrow\downarrow}$ is the average time between up-to-down flips, and $\tau_{\downarrow\uparrow}$ the characteristic time for the reverse process. There is a second process, so-called spin dephasing, and the spin dephasing time T_2 is defined as the time it takes for the tranverse spins

(the component perpendicular to the field or quantization axis) to reach equilibrium. It sets the timescale for an ensemble of spins that is initially precessing in phase to lose their phase coherence (hence "dephasing time"). The spin relaxation time and dephasing time are usually described by Bloch equations. Suppose $\boldsymbol{S}$ is the spin of an electron. When we apply a magnetic field along the z direction, the time evolution of the three spin components in the magnetic field $\boldsymbol{B}$ is given by[21]

$$\frac{dS_x}{dt} = \gamma(\boldsymbol{B} \times \boldsymbol{S})_x - \frac{S_x}{T_2} \tag{1.7}$$

$$\frac{dS_y}{dt} = \gamma(\boldsymbol{B} \times \boldsymbol{S})_y - \frac{S_y}{T_2} \tag{1.8}$$

$$\frac{dS_z}{dt} = \gamma(\boldsymbol{B} \times \boldsymbol{S})_z - \frac{S - S_z}{T_1} \tag{1.9}$$

Here γ is the gyromagnetic ratio. A simple model of spin relaxation and spin dephasing in a fluctuating magnetic field is shown in Fig. 1.2.

The mechanisms for spin relaxation in semiconductors stem from spin-orbit and hyperfine interactions. The interaction of the electron spin with its orbital motion around an atomic nucleus is called the spin orbit interaction (SOI). The electric field of the positively charged nucleus produces a magnetic field in the rest frame of the electron, which results in splitting of the states with parallel and antiparallel coupling of the spin- and orbital angular momenta. As the SOI grows strongly with atomic number Z (it scales as Z^4),[21] spin-orbit coupling is expected to be small in organic materials, but not negligible.[46] Hyperfine interaction is the interaction of the electron spins with the nuclear spins of the host material. The nuclear spins in organic materials are mainly due to the isotopes ^{1}H (I=3.2), ^{13}C (I=1/2), ^{14}N(I=2). In carbon, the isotope ^{13}C has ~1% abundancy, while the ^{12}C (99%) has no nuclear spin. The hyperfine interaction has been proposed as the main mechanism limiting the spin lifetime in organic materials.[44] The question of what the dominant spin relaxation mechanism is in organic materials is still controversial.

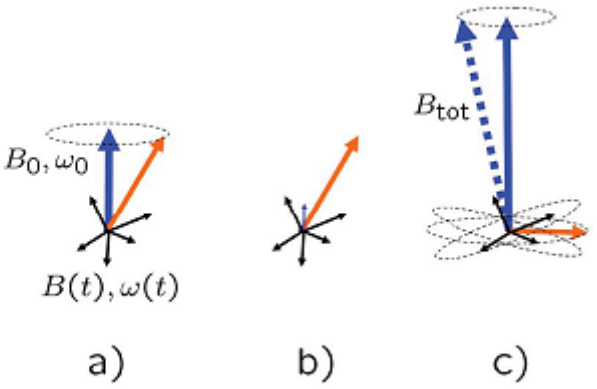

Figure 1.2 Model of spin relaxation and spin dephasing. (a) A spin in the presence of a static magnetic field along the z direction, B_0, giving rise to Larmor precession with angular frequency ω_0. In addition, a randomly fluctuating magnetic field B(t), giving rise to the Larmor frequency ω(t), is considered. (b) If the static field is small, then all the spin components are equal, so that T1 = T2. (c) If the static field is large, transverse fluctuating fields are inefficient in flipping the spin. Reprinted from Ref. 21.

1.2 Ferromagnetic/organic interfaces

In organic spintronic devices, the interfaces are very important.[47-50] The different results obtained for seemingly similar organic spin-valve devices, which consist of two FM electrodes separated by an organic insulator barrier/spacer, are often attributed to different spin behaviour at the interfaces.[36, 37, 47, 51] The chemical interactions between organic molecules and FM metals significantly affect the electronic- and magnetic structure of the FM/organic interface, through spin dependent hybridization effects.[52-56] This can give rise to large MR effects in LSMO/Alq_3/Co nano junctions, as has been shown by Barraud *et al.*[42] and in scanning tunnelling microscopy experiments on Co(111)/H_2Pc/Co(111)-tip systems by Stefan *et al.* [57]These studies suggest that it is possible to obtain a large interfacial spin polarization through *tailoring* the interfacial spin polarization via hybridization effects, an approach that has been coined "spinterface science".[48] Interfaces between carbon-based materials and FM metals usually exhibit charge transfer from/to the ferromagnet to the organic molecules, accompanied by the formation of covalent bonds.[58] Such chemisorption involves the frontier orbitals of

the carbon-based molecules and the FM metal valence band states, and may result in a sizeable interfacial spin polarization of the molecular orbitals, and the possible creation of a large interfacial magnetoresistance effect (IMR) (the work by Raman *et al.*[59] on Co/ZMR (zinc methyl phenalenyl) interfaces). The results mentioned above demonstrate the potential for engineering the interfacial spin polarization by chemical modification of the interfaces. However, in part due to the often *ill-defined* interfaces in devices, the microscopic mechanisms governing the magnetotransport behavior remain poorly understood. The evaporation of FM metals on organic materials could damage the organic materials at the organic/FM interface, and possible cause metal inclusions and metallic shorts in organic devices. The understanding of magnetotransport behaviour in organic spintronic devices may be improved upon exploiting the electronic structure and magnetic properties of *well-defined* interfaces between ferromagnetic electrodes and organic semiconductors.

1.3 Outline of the thesis

This thesis focuses on C_{60}-based structures for spintronics, including spin polarized transport studies of vertical spin valves, and studies of the electronic, magnetic and structural properties of ferromagnetic/C_{60} interfaces.

Chapter 2 describes the main experimental methods used in the thesis work, including fabrication techniques, magnetotransport measurement tools, and materials characterization methods such as synchrotron radiation techniques.

Chapter 3 discusses the spin-polarized transport behaviour in C_{60}-based spin valves. The physical insights into the magnetoresistance effects in the devices has been achieved with model calculations involving multi-step tunnelling.

Chapter 4 deals with the electronic and magnetic structure of C_{60}/bcc-Fe (001) interfaces. Photoemission spectroscopy (PES), and X-ray adsorption spectroscopy (XAS) are used to study the interfacial electronic structure and hybridization effects, e.g. charge transfer and chemisorption of C_{60} molecules on the Fe(001) surface.

In chapter 5, the effect of the C_{60}/Fe interaction on the magnetic moments of Fe surface atoms is described by a combined computational and experimental study. Similar experiments as described in chapter 4 have been done, but this time only three Fe monolayers (ML) were deposited onto a W(001) surface, such that the significant contribution of the Fe bulk atoms to the XAS yield is avoided. We used first-principles density functional theory (DFT) calculations to extract the magnetizations of the Fe surface, and of the C_{60}/Fe interface.

Chapter 6, the crystallinity and molecular ordering of C_{60} films on epitaxial Fe(001)/MgO(001) surfaces, characterised using X-ray diffraction (for thick C_{60} films) and scanning tunnelling microscopy (for demonstrating the local structural ordering of C_{60} molecules at the interfaces) are presented.

References

1. I. Žutić, J. Fabian and S. Das Sarma, Rev. Mod. Phys. **76** (2), 323 (2004).
2. S. Parkin, X. Jiang, C. Kaiser, A. Panchula, K. Roche and M. Samant, Proc. IEEE **91** (5), 661 (2003).
3. M. N. Baibich, J. M. Broto, A. Fert, F. N. Van Dau, F. Petroff, P. Etienne, G. Creuzet, A. Friederich and J. Chazelas, Phys. Rev. Lett. **61** (21), 2472 (1988).
4. G. Binasch, P. Grünberg, F. Saurenbach and W. Zinn, Phys. Rev. B **39** (7), 4828 (1989).
5. W.Thomson, Proc. R. Soc. London 8, 546-550 (1856)
6. B. Dieny, V. S. Speriosu, S. S. P. Parkin, B. A. Gurney, D. R. Wilhoit and D. Mauri, Phys. Rev. B **43** (1), 1297 (1991).
7. S. Ikeda, J. Hayakawa, Y. Ashizawa, Y. M. Lee, K. Miura, H. Hasegawa, M. Tsunoda, F. Matsukura and H. Ohno, Appl. Phys. Lett. **93** (8), 082508 (2008).
8. P. M. Tedrow and R. Meservey, Phys. Rev. B **7** (1), 318 (1973).
9. J. S. Moodera, L. R. Kinder, T. M. Wong and R. Meservey, Phys. Rev. Lett. **74** (16), 3273 (1995).

10. S. Tehrani, J. M. Slaughter, M. DeHerrera, B. N. Engel, N. D. Rizzo, J. Salter, M. Durlam, R. W. Dave, J. Janesky, B. Butcher, K. Smith and G. Grynkewich, Proc. IEEE **91** (5), 703 (2003).
11. J. C. Slonczewski, Phys. Rev. B **71** (2), 024411 (2005).
12. Y. Huai, F. Albert, P. Nguyen, M. Pakala and T. Valet, Appl. Phys. Lett. **84** (16), 3118 (2004).
13. http://www.everspin.com/PDF/ST-MRAM_Technical_Brief.pdf
14. http://en.wikipedia.org/wiki/Tunnel_magnetoresistance
15. M. Julliere, Phys. Lett. A **54** (3), 225 (1975).
16. J. C. Slonczewski, Phys. Rev. B **39** (10), 6995 (1989).
17. W. Wulfhekel, H. F. Ding and J. Kirschner, J. Magn. Magn. Mater. **242–245, Part 1** (0), 47 (2002).
18. J. S. Moodera, J. Nowak and R. J. M. van de Veerdonk, Phys. Rev. Lett. **80** (13), 2941 (1998).
19. J. Zhang and R. M. White, J. Appl. Phys. **83** (11), 6512 (1998).
20. C. Tiusan, F. Greullet, M. Hehn, F. Montaigne, S. Andrieu and A. Schuhl, J. Phys.: Condensed Matter **19** (16), 165201 (2007).
21. J. Fabian, A. Matos-Abiague, C. Ertler, P. Stano and I. Žutić, in *Acta Physica Slovaca. Reviews and Tutorials* (2007), Vol. 57, pp. 565.
22. S. Sugahara, Circuits, Devices and Systems, IEEEProc. **152** (4), 355 (2005).
23. G. Schmidt, D. Ferrand, L. W. Molenkamp, A. T. Filip and B. J. van Wees, Phys. Rev. B **62** (8), R4790 (2000).
24. E. I. Rashba, Phys. Rev. B **62** (24), R16267 (2000).
25. A. Fert and H. Jaffrès, Phys. Rev. B **64** (18), 184420 (2001).
26. V. A. Dediu, L. E. Hueso, I. Bergenti and C. Taliani, Nat. Mat. **8** (9), 707 (2009).
27. M. Johnson and R. H. Silsbee, Phys. Rev. Lett. **55** (17), 1790 (1985).
28. Ö. Mermer, G. Veeraraghavan, T. L. Francis, Y. Sheng, D. T. Nguyen, M. Wohlgenannt, A. Köhler, M. K. Al-Suti and M. S. Khan, Phys. Rev. B **72** (20), 205202 (2005).
29. B. Wästberg, S. Lunell, C. Enkvist, P. A. Brühwiler, A. J. Maxwell and N. Mårtensson, Phys. Rev. B **50** (17), 13031 (1994).
30. M. Weser, Y. Rehder, K. Horn, M. Sicot, M. Fonin and A. B. Preobrajenski, Appl. Phys. Lett. **96**, 012504 (2010).
31. P. K. J. Wong, T. L. A. Tran, P. Brinks, W. G. van der Wiel, M. Huijben and M. P. de Jong, Org. Electron. **14** (2), 451 (2013).

32. H. Ohno, Science **281** (5379), 951 (1998).
33. S. P. Dash, S. Sharma, R. S. Patel, M. P. de Jong and R. Jansen, Nature **462** (7272), 491 (2009).
34. C. B. Harris, R. L. Schlupp and H. Schuch, Phys. Rev. Lett. **30** (21), 1019 (1973).
35. V. I. Krinichnyi, S. D. Chemerisov and Y. S. Lebedev, Phys. Rev. B **55** (24), 16233 (1997).
36. Z. H. Xiong, D. Wu, Z.V. Vardeny and J. Shi, Nature **427**, 821 (2004).
37. V. Dediu, L. E. Hueso, I. Bergenti, A. Riminucci, F. Borgatti, P. Graziosi, C. Newby, F. Casoli, M. P. d. Jong, C. Taliani and Y. Zhan, Phys. Rev. B **78**, 115203 (2008).
38. M. Gobbi, F. Golmar, R. Llopis, F. Casanova and L. E. Hueso, Adv. Mat. **23** (14), 1609 (2011).
39. T. L. A. Tran, T. Q. Le, J. G. M. Sanderink, W. G. van der Wiel and M. P. de Jong, Adv. Funct. Mater. **22** (6), 1180 (2012).
40. R. Lin, F. Wang, M. Wohlgenannt, C. He, X. Zhai and Y. Suzuki, Synth. Met. **161** (7–8), 553 (2011).
41. V. Dediu, M. Murgia, F. C. Matacotta, C. Taliani and S. Barbanera, Solid State Commun. **122** (3-4), 181 (2002).
42. C. Barraud, P. Seneor, R. Mattana, S. Fusil, K. Bouzehouane, C. Deranlot, P. Graziosi, L. Hueso, I. Bergenti, V. Dediu, F. Petroff and A. Fert, Nat. Phys. **6** (8), 615 (2010).
43. A. J. Drew, J. Hoppler, L. Schulz, F. L. Pratt, P. Desai, P. Shakya, T. Kreouzis, W. P. Gillin, A. Suter, N. A. Morley, V. K. Malik, A. Dubroka, K. W. Kim, H. Bouyanfif, F. Bourqui, C. Bernhard, R. Scheuermann, G. J. Nieuwenhuys, T. Prokscha and E. Morenzoni, Nat Mater **8** (2), 109 (2009).
44. P. A. Bobbert, T. D. Nguyen, F. W. A. van Oost, B. Koopmans and M. Wohlgenannt, Physical Review Letters **99** (21), 216801 (2007).
45. J. J. H. M. Schoonus, P. G. E. Lumens, W. Wagemans, J. T. Kohlhepp, P. A. Bobbert, H. J. M. Swagten and B. Koopmans, Physical Review Letters **103** (14), 146601 (2009).
46. Z. G. Yu, Physical Review Letters **106** (10), 106602 (2011).
47. S. Steil, N. Grossmann, M. Laux, A. Ruffing, D. Steil, M. Wiesenmayer, S. Mathias, O. L. A. Monti, M. Cinchetti and M. Aeschlimann, Nat. Phys. **9** (4), 242 (2013).
48. S. Sanvito, Nat. Phys. **6** (8), 562 (2010).

49. P. Ruden, Nat. Mater **10** (1), 8 (2011).
50. V. A. Dediu, Nat. Phys **9** (4), 210 (2013).
51. T. Shimada, H. Nogawa, T. Noguchi, Y. Furubayashi, Y. Yamamoto, Y. Hirose, T. Hitosugi and T. Hasegawa, Jpn. J. Appl. Phys. **47** (2), 1184 (2008).
52. S. Javaid, M. Bowen, S. Boukari, L. Joly, J. B. Beaufrand, X. Chen, Y. J. Dappe, F. Scheurer, J. P. Kappler, J. Arabski, W. Wulfhekel, M. Alouani and E. Beaurepaire, Phys. Rev. Lett. **105** (7), 077201 (2010).
53. N. Atodiresei, J. Brede, P. Lazic, V. Caciuc, G. Hoffmann, R. Wiesendanger and S. Blügel, Phys. Rev. Lett. **105**, 066601 (2010).
54. Y. Zhan, E. Holmström, R. Lizárraga, O. Eriksson, X. LiU, E. Carlegrim, S. Stafström and M. Fahlman, Adv. Mater. **22**, 1626 (2010).
55. T. L. A. Tran, P. K. J. Wong, M. P. de Jong, W. G. van der Wiel, Y. Q. Zhan and M. Fahlman, Appl. Phys. Lett. **98**, 222505 (2011).
56. T. L. Tran, D. Cakir, P. K. Wong, A. B. Preobrajenski, G. Brocks, W. G. van der Wiel and M. P. de Jong, ACS Appl. Mater. Interfaces **5** (3), 837 (2013).
57. S. Schmaus, A. Bagrets, Y. Nahas, T. K. Yamada, A. Bork, M. Bowen, E. Beaurepaire, F. Evers and W. Wulfhekel, Nat. Nano. **6** (3), 185 (2011).
58. M. R. C. Hunt, S. Modesti, P. Rudolf and R. E. Palmer, Phys. Rev .B **51** (15), 10039 (1995).
59. K. V. Raman, A. M. Kamerbeek, A. Mukherjee, N. Atodiresei, T. K. Sen, P. Lazic, V. Caciuc, R. Michel, D. Stalke, S. K. Mandal, S. Blugel, M. Munzenberg and J. S. Moodera, Nat. Mat. **493** (7433), 509 (2013).

CHAPTER 2

Experimental methods

In this chapter, we present the major experimental techniques that are used in this thesis work. The chapter is divided into two sections: Section 2.1 describes the fabrication techniques and measurement methods used in Chapters 3 and 6. Section 2.2 is devoted to the synchrotron radiation techniques that are used in Chapter 4 and 5.

2.1 Fabrication techniques and measurement setup

2.1.1 Molecular beam epitaxy system

The devices and samples discussed in Chapter 3 and Chapter 6 of this thesis have been fabricated using a Metal-600 molecular beam epitaxy (MBE) system from DCA Instruments using shadow masks. The MBE system consists of two vacuum chambers: an evaporation chamber and a smaller load-lock chamber. Substrates are mounted on a sample holder together with a stainless steel plate containing shadow masks. A spring mechanism, which can be triggered using a wobble stick, allows the samples to be rotated relative to the shadow masks, enabling multiple deposition steps onto the same sample through different masks. The sample holder is then loaded into the load-lock chamber (base pressure 10^{-8} mbar), which is pumped down to a pressure of about 10^{-7} mbar (10^{-5} Pa) before the samples are transferred to the evaporation chamber. The base pressure in the ultra-high vacuum (UHV) evaporation chamber is maintained at about 2×10^{-10} mbar using a cryo-pump, based on a closed-cycle He gas refrigerator. During deposition, additional pumping capacity is provided by a liquid nitrogen cooled baffle.

Metals and oxides are deposited using electron beam evaporation from Telemark 568 high voltage (HV) electron beam (e-beam) sources. The film thickness is controlled by quartz crystal monitors, which are installed close to the e-beam sources. The oxidation of Al, which is used to obtain high quality Al_2O_3 tunnel barriers on Co electrodes, is done in the load-lock chamber using an oxygen plasma (in 100 mbar oxygen). For the device fabrication, which is discussed in section 2.1.2, all layers are deposited at room temperature. For some samples, for example containing epitaxial ferromagnetic metals (e.g. body-centered cubic (bcc)-Fe) and crystalline C_{60} films (see Chapter 6), we used a sample holder with an on-board heater. With this holder, the substrate temperature can be controlled, and it is possible to anneal substrates up to 800 ^{o}C during (or prior to) deposition. For deposition of C_{60} molecules, both at room temperature and at elevated temperatures, a Knudsen effusion cell is used. The film thickness is controlled by keeping the temperature of the effusion cell constant while setting the deposition time, using a pre-calibrated (with atomic force microscopy) deposition rate.

Figure 2.1 shows a photograph of the DCA Metal-600 MBE system. Indicated are the UHV chamber, load-lock, C_{60} source, e-beam source, quartz

crystal monitor, oxygen plasma source, and liquid nitrogen (LN_2) lines connecting to the cooling baffle.

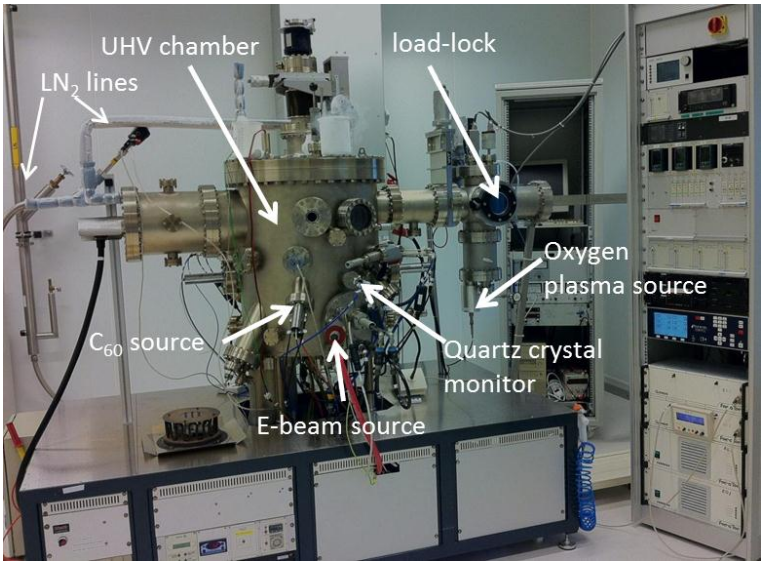

Figure 2.1 Photograph of the DCA Metal-600 MBE system

2.1.2 Fabrication of C_{60}-based spin valves

We prepared a series of vertical spin transport devices, consisting of, from top- to bottom, Al(cap, 2 nm)/NiFe(15 nm)/C_{60}(0-20 nm)/Al_2O_3(2 nm)/Co(8 nm), on single-crystalline (0001) sapphire (Al_2O_3) substrates (11×11 mm^2). Reference magnetic tunnel junctions (MTJs), consisting of Al(cap, 2 nm)/NiFe(15 nm)/Al_2O_3(2 nm)/Co(8 nm) were also prepared. All layers were deposited in a single run in the UHV chamber, using shadow masking to make a cross-bar geometry. Fig. 2.2a shows the shadow masks used for device fabrication, with sample positions 1-12 indicated. The shadow masks are arranged such that cross-bar structures can be obtained on two substrates simultaneously. The layer stack produced during the deposition process is shown in Fig. 2.2b. The fabrication of our devices is carried out in the following steps:

(1) Initially, two single crystalline sapphire substrates are put in positions 5 and 6, where a Co layer is evaporated. The thickness of this layer is 8 nm, and the Co layer is patterned into 5.0 ×2.0 mm^2 features using shadow masks.

(2) Subsequently, the samples are moved to positions 2 and 3, where a 1.5 nm Al layer is deposited over the full area of the samples. This is followed by plasma oxidation for 30 minutes (at a constant oxygen pressure of 100 mTorr). After this process, the aluminum layer is fully oxidized, and has an approximated thickness of 2.0 nm (the thickness of the oxidized Al layer is estimated assuming a 30% expansion of the Al layer upon oxidation into Al_2O_3).

(3) Afterwards, the two samples are moved to position 4 and 3 for C_{60} deposition. Position 4 is "closed" (Fig. 2.2a), such that a C_{60} layer is formed only at position 3. The thickness of this layer is varied between 0 and 20 nm. After this step, we have two different samples with and without a C_{60} layer on top of the Al_2O_3 tunnel barrier. The sample without C_{60} may serve as a reference MTJ in transport studies.

(4) At position 1 and 12, a 30 nm Al_2O_3 layer is deposited. This layer is used to define the junction area, by exposing a 250 μm wide channel on the bottom electrode. It prevents electrical contact between the bottom- and top electrodes outside of the active area. The Al_2O_3 features have an area of 3.3 ×1.4 mm^2.

(5) Finally, the second ferromagnetic layer (15 nm NiFe) is evaporated at position 7 and 8. At the same position, a 2 nm thin Al cap is deposited. This cap prevents the NiFe layer from oxidizing. The area of the NiFe and Al strips is 4.5×0.3 mm^2.

Following this procedure, we have one sample with a C_{60} layer (hybrid junction) and a standard MTJ (without C_{60}) as a reference. Each sample contains 12 junctions (see Fig. 2.2c), and each junction has an area of 0.25 × 0.30 mm^2.

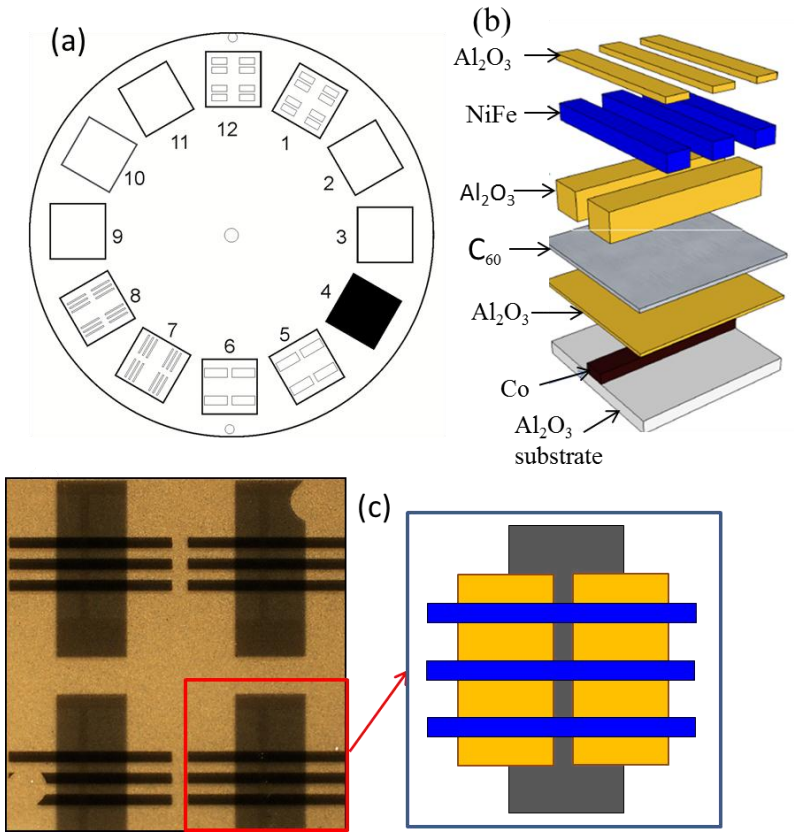

Figure 2.2 (a) Drawing of the shadow masks used for device fabrication, (b) layer stack as deposited in the fabrication process; and (c) optical microscope image of fabricated devices, showing 12 junctions on a single substrate (left panel) and a sketch of a single cross bar structure containing 3 junctions (right panel).

2.1.3 Magnetotransport measurements

The magnetotransport properties of the fabricated devices have been characterized using a measurement setup comprised of a Keithley 2400 source meter, an electromagnet (Bruker Corporation) and a liquid He flow cryostat system (Oxford Instruments) (see Fig. 2.3). The sample, with size of 11x11 mm^2, can be fitted onto a cartridge containing a printed circuit board for wire bonding. This cartridge is introduced into the flow cryostat, which is at the center of the Bruker electromagnet. With this setup, we can measure current versus voltage (*I*-*V*) curves

at different magnetic field strengths/orientations, and current versus magnetic field (*I*-*H*) curves at different applied bias voltages. These measurements can be performed at temperatures between 5 and 300 K. The Bruker electromagnet can generate a magnetic field up to ~1 T. The measurements were performed using a four-point probe technique with the magnetic field applied parallel to the sample surface (Fig. 2.4). The samples were rotated with respect to the magnetic field such that sharp switching behavior was observed in the MR traces, (magnetization along the easy axis of both bottom- and top electrode).

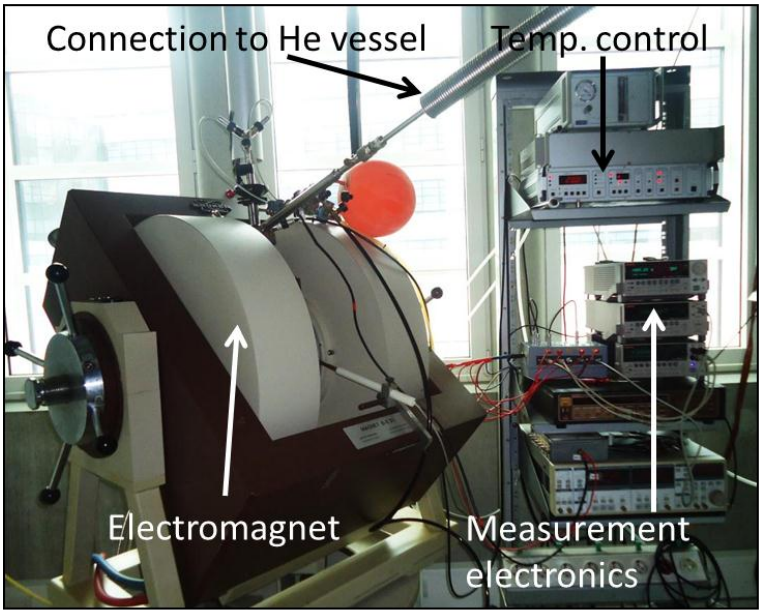

Figure 2.3 Photograph of the measurement setup for characterization of the magneto transport properties of the devices. The setup includes: computer (not shown here), Bruker electromagnet, measurement electronics (Keithley 2400 source meter), temperature controller, He transfer line connecting to the liquid He vessel (not shown) for cooling.

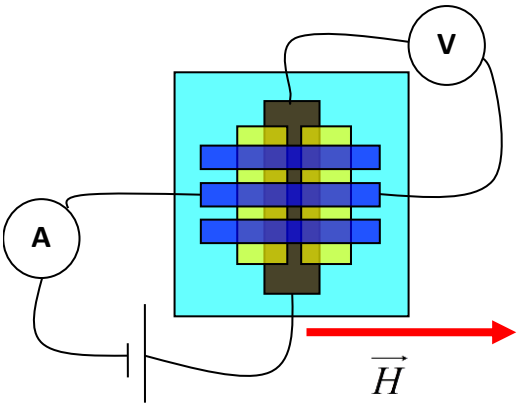

Figure 2.4 Four-probe measurement geometry for magnetotransport measurements

2.1.4 Deposition of epitaxial bcc-Fe and C_{60}/bcc-Fe films on MgO substrates

We prepared epitaxial bcc-Fe and C_{60}/bcc-Fe bilayers on MgO (001) substrates, using the MBE system described above, as well as a mini e-beam evaporator (Tectra, for Fe deposition) and a custom made Knudsen cell (for C_{60} deposition) in the preparation chamber of a scanning tunneling microscope (STM).

Single crystalline MgO(001) substrates (MaTeck GMbH), with a root mean square roughness of 0.15 nm, are employed for the growth of epitaxial Fe. Due to the fairly small lattice mismatch between MgO(001) and bcc-Fe (001) upon rotation of the lattices by 45^{o} (3.8 %), epitaxial bcc-Fe films may be obtained using well-known methods.[1, 2]

For cleaning the MgO substrates, wet chemical rinsing and annealing in UHV are performed. The substrate is first cleaned in acetone, ethanol and isopropanol, for about 20 minutes each at 50^{o}C, to remove contamination from the surface. After loading the sample(s) into the UHV chamber, the substrate is heated to 500^{o}C for 1 hour to remove remaining contamination (e.g carbon containing species) and to allow for surface reconstruction.

In the MBE chamber, every deposition run involved two substrates (10×10 mm^2), which were mounted on a sample holder with built-in heater. First, Fe films were deposited on both MgO substrates. After that, a shadow mask is used to close off one sample to the deposition sources while leaving the second sample exposed. On this exposed sample, a film of 100 nm C_{60} is deposited. Hence, a pair of samples, comprised of an Fe layer and a C_{60}/Fe bilayer, are obtained. The film thickness and surface morphology of these bcc-Fe layers and C_{60}/Fe bilayer films were characterized by atomic force microscope (AFM).

As stated above, similar bcc-Fe films and C_{60}/Fe stacks were deposited using a (custom-made) sample preparation chamber attached to a commercial UHV-STM system (RHK Technology). In order to obtain reliable electrical contact between the deposited films and the sample holder, we deposited (ex-situ) 30 nm thick W strips at two opposing edges of the 5x5 mm^2 MgO (001) substrates using a DC-magnetron sputtering tool. In the STM sample holders, the samples are secured by clamping onto these W-covered regions, providing electrical contact to the top surface. The substrates were cleaned with the wet chemical treatments described above, and introduced into the STM preparation chamber, where a similar heat treatment was carried out prior to the deposition.

2.1.5 Scanning tunneling microscopy

A multipurpose UHV-STM system was used in this work, based on a commercial variable-temperature STM (RHK Technology). The system is equipped with a liquid Helium flow cryostat, enabling constant (low) temperatures (down to <10 K at the sample) during measurements. It comprises several interconnected chambers, including a load lock for fast sample transfer, and a homemade sample preparation chamber, where sample heating up to 600 ºC and thin film depositions of (magnetic) metals and organic molecules are possible. An external magnetic field of up to 200 Oe can be applied for magnetotransport measurements if necessary (not used in this work). In chapter 6 of this thesis, we used STM to investigate the adsorption mechanism and local structural ordering of C_{60} on the epitaxial Fe(001) surface at the molecular scale. The measurements were perfomed in the constant current mode, using mechanically cut Pt-Ir tips at room temperature (RT) with a set-point current of 0.8 nA and a bias voltage of 230 mV.

The STM was developed by Binnig and Rohrer in 1981.[3]The basic components of an STM system are (1) a sharp metal tip (ideally with a single atom at its apex), (2) a piezoelectric scanner, (3) a current amplifier (to detect the small tunnel current), (4) a bias controller (to provide the tip-to-sample bias) and (5) a feedback loop (to keep the tunnel current at a fixed set point by adjusting the tip height with the piezoelectric scanner), see Fig. 2.5. STM operates on the basis of the *quantum mechanical tunneling* effect,[4] which results in a current flow between a metal tip and the surface of a conducting material upon applying a bias voltage, if the tip-to-sample distance is kept at just a few nanometers. The current produced by tunneling (tunnel current) depends exponentially on the distance between the tip and the sample's surface.

In *constant current mode*, the height of the tip above the sample surface is varied in order to keep the tunnel current constant, as the tip is scanned, line by line, over the surface. The tip is mounted on a piezoelectric tube, which controls the tip position in three dimensions relative to the sample. The piezoelectric element that moves the tip towards or away from the sample surface (defined as the z-axis) is controlled by a feedback circuit monitoring the tunnel current while scanning. As the tip is scanned in the x-y plane, the z-position of the tip is recorded by a computer and presented in an image by the STM software. As a result, a map of the surface is obtained, containing information on the physical topography (peaks and valleys on the surface) as well as the electronic properties (local density of states and local nature of the electronic wave function) of the sample.

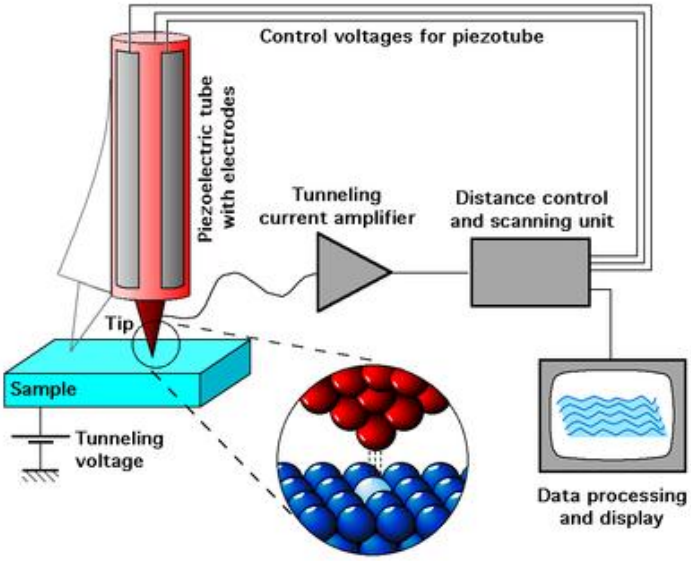

Figure 2.5 The schematic view of an STM (Ref. 3)

2.1.6 Atomic force microscopy

An AFM (Veeco, model DI 3100) was used in our experiments for measuring the thickness of C_{60} films, and the surface roughness of various samples: Co/Al_2O_3 and $Co/Al_2O_3/C_{60}$ on sapphire (see chapter 3), bcc-Fe on MgO, and C_{60}/Fe bilayers on MgO substrates (see Fig. 2.7).

The AFM was developed by Binnig *et al*. (in 1985) to overcome an obstacle of STM, which can only image conducting surfaces. [5]An AFM probe consists of a micro-scale cantilever with a sharp tip that is used to scan the sample surface, using forces between the tip and the surface. These forces may originate from a wide range of physical (and chemical) interactions, including attraction and repulsion due to Van der Waals forces, capillary forces, chemical bonding, electrostatic forces, magnetic forces, etc. There are three most commonly used operational modes of AFM: contact mode, non-contact mode and tapping mode (Fig.2.6b).

In this thesis, all AFM measurements were done in tapping mode. In tapping mode (also called intermittent contact mode), the cantilever oscillates with a

frequency close to its resonance frequency (~300 kHz in our case), while lightly "tapping" the tip on the surface during scanning.

We used AFM tips made from silicon nitride. Tips are attached to a tip holder, which is subsequently placed inside the AFM head. The AFM head, with cantilever/tip, is then placed above the sample by means of 2 tension springs connecting the AFM head to a dovetail groove. The diagram of an AFM is shown in Fig.2.6a. The cantilever deflection is monitored using a laser and photodetector. The laser position is manually adjusted such that the laser beam points directly at the cantilever tip, where it is reflected onto a 4 quadrant photodetector. When the cantilever tip is brought into contact with the sample surface, its scanning motion is conducted by a piezoelectric scanner, which scans the tip in a raster pattern with respect to the sample. The tip-sample interaction, which influences the deflection of the cantilever, is recorded by the reflected laser spot on the photodetector. By detecting the difference in the photodetector output voltages for different quadrants, changes in the cantilever deflection (or oscillation amplitude) are determined. In this way, the laser deflection is used to detect the root-mean-square (RMS) amplitude of cantilever oscillation. A feedback loop maintains constant oscillation amplitude by moving the piezoelectric scanner vertically at every data point. By recording this movement, a topographical image can be obtained.

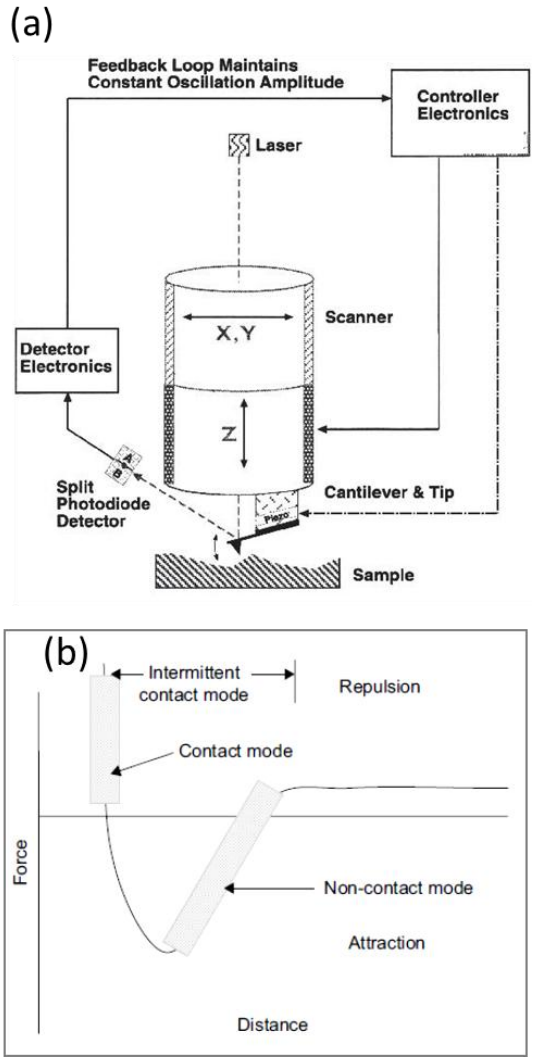

Figure 2.6 (a) Diagram of the operation principles of an atomic force microscope (from Ref. [5]). (b) Diagram of the force regimes for operation of the three most common modes of AFM. Contact mode operation is in the repulsive force regime, where the tip is pressed against the sample surface, causing an upwards deflection of the cantilever. Non-contact mode is operated in the regime of long-range forces experienced prior to actual contact with the surface. For intermittent contact (or tapping) mode, the cantilever oscillates close to the surface, and the tip repeatedly comes into- and out of contact with the surface.

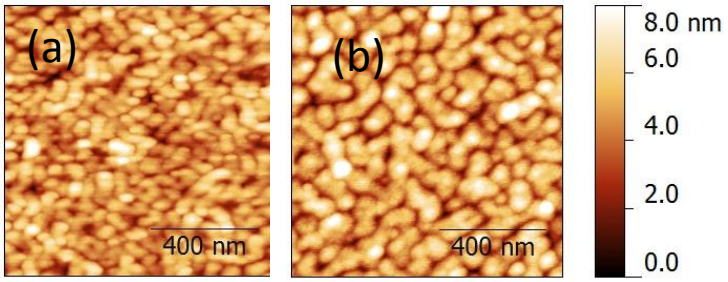

Figure 2.7 AFM images of two different surfaces, (a) a bcc-Fe(001) film on MgO, and (b) a C_{60}/bcc-Fe(001) bilayer on MgO, respectively. Details on sample preparation are given in section 2.1.4.

2.2 Synchrotron radiation techniques

2.2.1 Beamline D1011 at MAX-Lab, Lund, Sweden

The electromagnetic radiation emitted when charged particles are accelerated radially is called **synchrotron radiation**. The synchrotron radiation techniques that were used in this thesis work are photoemission spectroscopy (PES), x-ray absorption spectroscopy (XAS), and x-ray magnetic circular dichroism (XMCD). All measurements were performed at Beamline D1011 of MAX-Lab, Lund University, Sweden.[6] D1011 is a bending magnet beamline, covering a photon energy range of about 100 to 1800 eV. It is suitable for performing PES and XAS using linearly polarized light. Moreover, an adjustable local "bump" of the electron beam (steering the beam out-of-plane where the emitted radiation is extracted) provides out-of-plane radiation with circular polarization, which makes XMCD measurements possible.

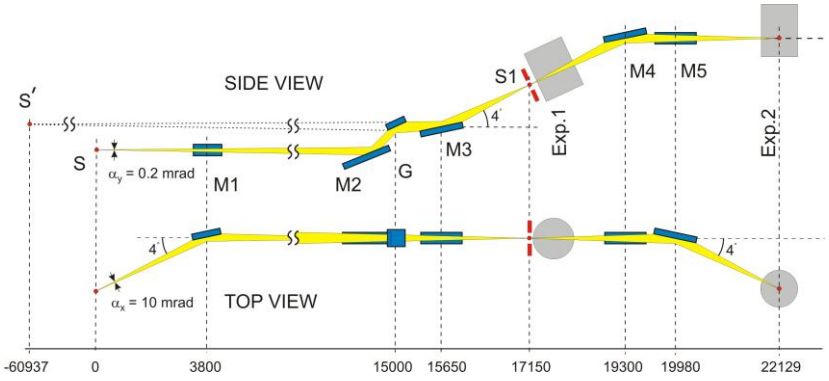

Figure 2.8 Diagram of beamline D1011, consisting of virtual monochromatic source (S´), source (dipole magnet, S), horizontally focusing spherical mirror (M1), plane mirror (M2), grating (G, 1200 lines/mm), vertically focusing plane elliptical mirror (M3), exit slit of the monochromator (S1), front experimental station (Exp.1), vertically re-focusing spherical mirror (M4), horizontally re-focusing spherical mirror (M5), and back experimental station (Exp.2). Reprinted from Ref. 6.

There are two experimental stations at beamline D1011 placed in series, which we refer to as "front station" and "back station". The front station is positioned directly after the exit slit of the monochromator, while the back station is mounted further down-stream and receives radiation passing through the front station via re-focusing mirrors (M4 and M5 in Fig. 2.8). The front station consists of separate analysis- and preparation UHV chambers, and a load-lock chamber. Sample transfer between the analysis- and preparation chambers is achieved via a long-travel manipulator. The analysis chamber is equipped with a SCIENTA SES200 (upgraded) electron energy analyzer, for PES measurements, and an MCP detector for XAS measurements in the partial electron yield (PEY) mode. Therefore we could use the front station for both PES, XAS and XMCD measurements. However, there is no electromagnet in the front station, samples can be magnetized instead by approaching the sample with a permanent magnet, mounted on a linear drive in the preparation chamber. This is quite cumbersome for XMCD experiments, which typically require the magnetization of the sample to be flipped. For our experiments, we used the front station for PES and XAS, and the back station for XAS and XMCD measurement in the total electron yield (TEY) mode. The back station is especially designed for XMCD measurements. It consists of a load lock and a single UHV preparation/analysis chamber, with an electromagnet installed in-situ. The electromagnet provides a field strength up to about 300 Oe, allowing for XMCD measurements while applying a constant

magnetic field, and also for measuring hysteresis loops. In both stations, facilities for sample preparation, a sample transfer system, provisions for sample heating and cooling, a gas inlet system, an Ar sputter gun, a low energy electron diffraction (LEED) system, which allows to examine the crystal structure of the sample surface, and a mass spectrometer for residual gas analysis are available.

2.2.2 Photoemission spectroscopy

Photoemission spectroscopy (also known as photoelectron spectroscopy (PES)) probes the electronic structure of matter. PES is based on the photoelectric effect, in which electrons are emitted from a sample after absorption of light. This is a quantum phenomenon discovered by Heinrich Rudolf Hertz in 1887, and explained by Einstein in 1905. [7]The sample under investigation is irradiated with (monochromatic) light and, due to the photoelectric effect, electrons are emitted from the sample. The kinetic energy of these emitted electrons is subsequently determined, using for example an electrostatic analyzer. In our case, a hemispherical analyzer is used. Thus, if the energy of the impinging photon $h\nu$, the kinetic energy of the photoelectron E_K, and (for solid samples) the work function Φ of the sample are known, the binding energy E_B of the state from which the photoelectron originates is determined as:

$$E_B = h\nu - \phi - E_K \tag{2.1}$$

In this expression, the binding energy is given with respect to the vacuum level E_{VAC}, which is usually done for spectroscopy of free atoms and molecules. However, for experiments on solids (which is the case here) it is common practice to choose the Fermi level as the reference point for binding energy determinations. The Fermi level is a natural reference for solid-state samples, because the spectrometer and the (conducting) sample will have a common Fermi energy when in contact. This avoids the necessity to deal with (often unknown) work functions Φ.

The different excitation sources used in photoelectron spectroscopy cover a wide spectrum of photon energies. Historically, different acronyms were used for PES, according to the photon energy used. (1) Ultravoilet photoelectron

spectroscopy (UPS) for an energy range of several eV up to about 100 eV, i.e. using vacuum UV radiation, to examine valence levels. (2) X-ray Photoelectron spectroscopy (XPS) for an energy range of 200-2000 eV, i.e. using soft x-rays, to study core levels. With the advance of synchrotron radiation, this distinction has become less meaningful. At Beamline D1011, light is available with a continuous tunability over a wide range (from 100 to 1800 eV), which makes it possible to cover both valence band PES (or UPS) and core level PES (or XPS). In XPS, an atom in a molecule or solid absorbs the x-ray photon, leading to ionization and the emission of a core electron. In UPS the photon interacts with valence electrons of the molecule or solid, leading to ionization by removal of one of these valence electrons (see Fig.2.9).

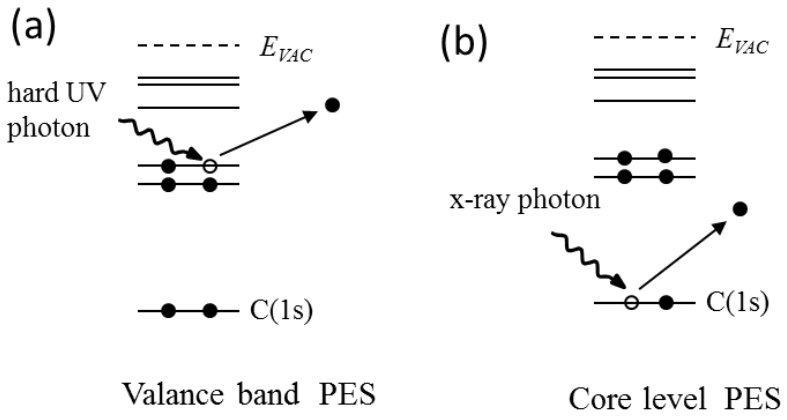

Figure 2.9 Schematic representation of the final electronic states reached in valence band PES (a) and core level PES (b) of a sample containing carbon atoms. The horizontal bars indicate the energy levels, open (solid) circles represent holes (electrons).

Inelastic Mean Free Path

The electron inelastic mean free path (IMFP, [8]which is related to the electron escape depth) is an important parameter for describing the surface sensitivity of PES and related electron spectroscopies, such as XAS and XMCD. It determines the depth below the surface (measured along the sample normal) from which photoelectrons still manage to reach the analyser and hence contribute to the measured signal. Electrons traveling through a solid may lose part of their kinetic

energy due to electron-electron (excitation of plasmons in metals and semiconductors, creation of electron-hole pairs) and electron-phonon interactions. The longer the distance that electrons travel, the higher the probability for an energy loss event. The IMFP is the mean distance between such inelastic events. Once the photoelectron has undergone an inelastic scattering event, its kinetic energy has decreased by a certain amount, and it no longer contributes to a photoelectron peak, but to the background instead. Information regarding the IMFP is needed for determination of e.g. film thickness, and for estimating the surface sensitivity. The IMFP is a measure of the probability for an electron originating from a certain depth (not) to be inelastically scattered, determined by the following equation:

$$P(d) = \exp(-d/\lambda), \tag{2.2}$$

Where $P(d)$ is the probability of the electron travelling a distance d through a solid without undergoing scattering, and λ is IMFP of the electrons at energy E. The IMFP depends on (1) the initial kinetic energy of the electron and (2) the nature of the solid, in particular the electron density. Since most metals have comparable electron densities, they show a similar IMFP versus energy relationship.

Fig. 2.10 is the universal curve (IMFP as a function of kinetic energy), giving the electron escape depth for metallic samples. The IMFP exhibits a minimum for the electrons with a kinetic energy of 50-100 eV.

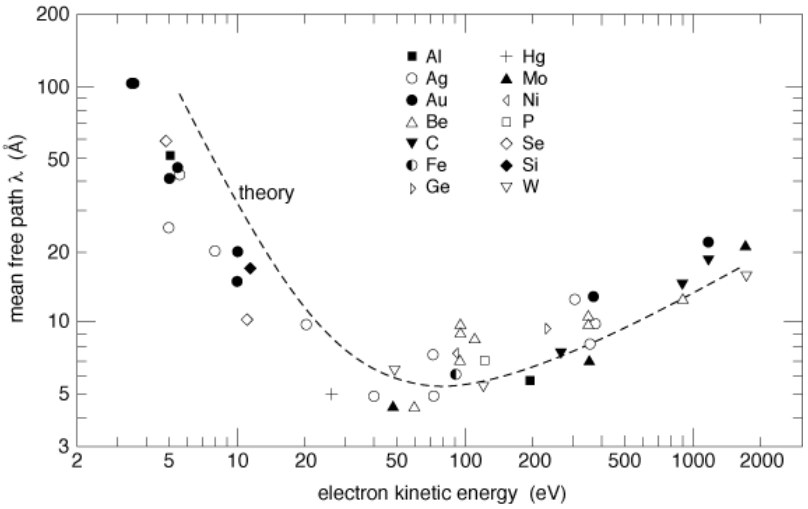

Figure 2.10 Universal curve of the inelastic mean free path of electrons, valid for metallic samples. Measured values are indicated by closed circles (Ref.8).

If the IMFP is known, we can estimate the thickness of a layer covering a substrate by evaluating the suppression of signals originating from the substrate. In our case, we estimated the thickness of C_{60} layers on Fe surfaces, and the thickness of Fe films on MgO substrates by comparing the intensity of the PES/XAS signal before- and after deposition of the top layer. The PES/XAS signal from the substrate (e.g Fe) is attenuated (e.g. reduced in intensity) due to the inelastic scattering of photoelectrons when they travel through the top layer (e.g C_{60}). The probability that electrons pass through the C_{60} layer without any inelastic scattering is given by equation (2.2), by replacing d by the thickness of the C_{60} layer (t). Therefore, the thickness t can be determined by the following equation:

$$I=I_0 \exp(-t/\lambda), \tag{2.3}$$

Where I_0 and I are the intensity of the Fe signal detected without and with C_{60} layer, respectively, and λ is IMFP of electrons (originating from Fe) at a certain kinetic energy.

2.2.3 X-ray absorption spectroscopy

X-ray absorption spectroscopy (XAS)[9] is an important synchrotron radiation tool for the characterization of the electronic structure of materials. Because it involves excitations of core level electrons, it is an element specific probe, and useful for fundamental studies of atoms, molecules, absorbates, and solid samples. XAS spectra are obtained by scanning the photon energy, in our case using a plane grating monochromator, to a range where core electrons of the elements of interest can be excited into unoccupied states (usually from 100 eV to 100 000 eV photon energy).

When a sample is hit by an incident x-ray beam with intensity I_0, the oscillating electric field of the electromagnetic radiation interacts with the electrons in the sample. The radiation may be scattered by these electrons, or absorbed by exciting the electrons into states with higher energy (Fig. 2.11a).

In contrast with the PES technique, where the photon energy is fixed and the electron intensity is measured as a function of electron kinetic energy, in XAS the x-ray energy is scanned and the absorbed x-ray intensity is measured. XAS spectra can be recorded in two common ways, (1) x-ray transmission or (2) fluorescence- or electron yield measurements. In the transmission technique (Fig. 2.11b), the intensity of the x-ray beam is measured before (I_0) and after passing through a sample (I_x), for example using an ionization chamber detector. Since this technique requires thin samples such that x-rays may pass through, it has limited use. Instead, fluorescence- or electron yield measurements rely on the detection of x-rays or electrons that are emitted *after* the initial x-ray absorption events, when the excited electrons decay back to their ground states. In this work, we used electron yield measurements. Two modes can be distinguished: total electron yield (TEY), and partial electron yield (PEY). The TEY mode (Fig.2.11c) can be described as follows. The incident x-rays create core holes that are filled shortly after the excitation events, emitting Auger electrons. These Auger electrons may scatter on their way to the sample surface, leading to a collision cascade, in which a large number of low-energy electrons is produced. All emitted electrons (hence total yield) are measured by a picoammeter connecting the sample to ground. The resulting "drain current" signals are proportional to the x-ray absorption intensity. In a PEY measurement, low energy electrons are discarded, usually by using a grid at a fixed retarding potential in front of an electron multiplier (f.e. a microchannel

plate detector). Since low energy electrons, produced in collision cascades, may escape from a relatively large depth, the PEY mode is more surface sensitive than the TEY mode.

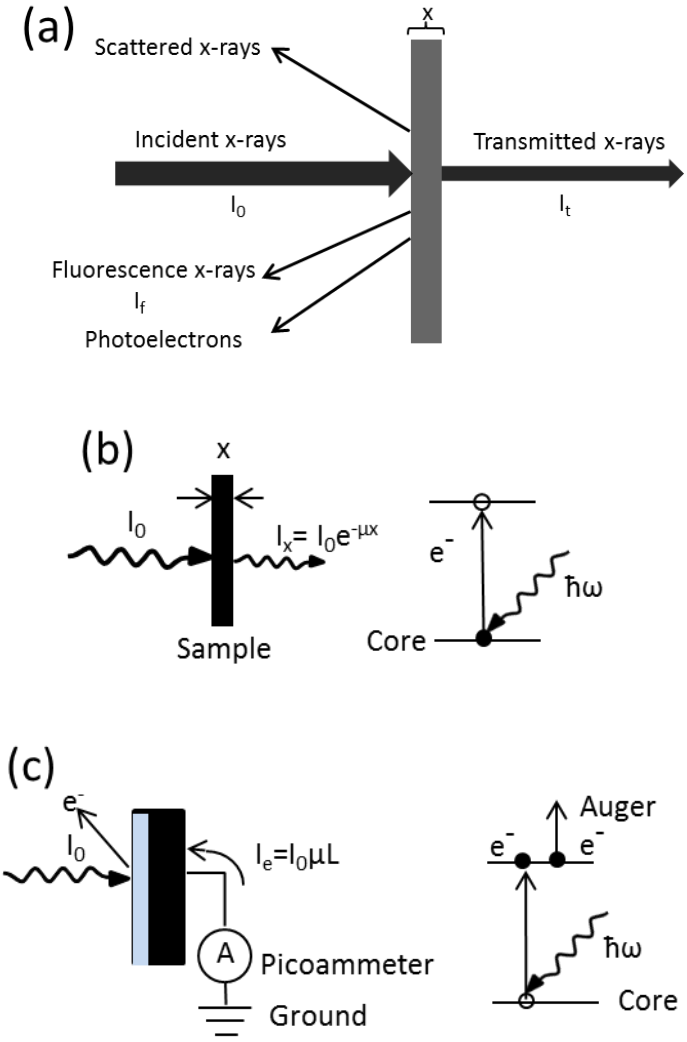

Figure 2.11 (a) The sketch of X-ray absorption. Two methods of XAS measurement (b) transmission, and (c) total electron yield detection, where L is the sampling depth (typically a few nanometers).

At certain energies, the x-ray absorption probability increases drastically, giving rise to so-called absorption edges. The onset of such an edge occurs when

the energy of the incident photon is just sufficient to cause excitation of a core electron of the absorbing atom into the bottom of the conduction band (for solid samples), or the lowest unoccupied orbital for atoms and molecules. At higher photon energy, core electrons are excited into higher lying unoccupied states, and eventually into the vacuum when the photon energy lies above the ionization threshold. The photon energies at which absorption edges occur correspond to the binding energies of electrons in the K, L, M, shells; hence they are labeled as K-, L_1-, L_2-, L_3-, M_1-edges, etc., corresponding to the excitation of electrons in the 1s, 2s, $2p_{1/2}$, $2p_{3/2}$, 3s orbitals, etc., respectively.

2.2.4 X-ray magnetic circular dichroism

X-ray magnetic circular dichroism (XMCD) is used for probing element specific magnetic properties of matter. An XMCD spectrum is obtained by taking a difference spectrum of two XAS measurements recorded with different alignment between the magnetization vector and the (circular) polarization of the light. This can be done, for example, by fixing the magnetization using a magnetic field, while taking a spectrum with left circularly polarized light, and another one with right circularly polarized light. Alternatively, the polarization may be kept fixed, while the magnetization is varied via the applied magnetic field. The principle of XMCD is based on magneto-optical effects.[9] As described above, x-ray absorption is the process of x-ray induced excitation of core electrons to unoccupied levels (or to the vacuum). Ferromagnetic materials have a spin-dependent density of states (DOS). If the x-ray absorption process is spin dependent, the difference of the absorption intensity reflects the spin polarization of the unoccupied DOS. Circularly polarized light is used, such that the photons carry an intrinsic angular momentum of -/+ $\hbar$ (left/right circular polarization). This angular momentum is also called the photon spin. Fig. 2.12 shows a schematic diagram illustrating the principle of XMCD.

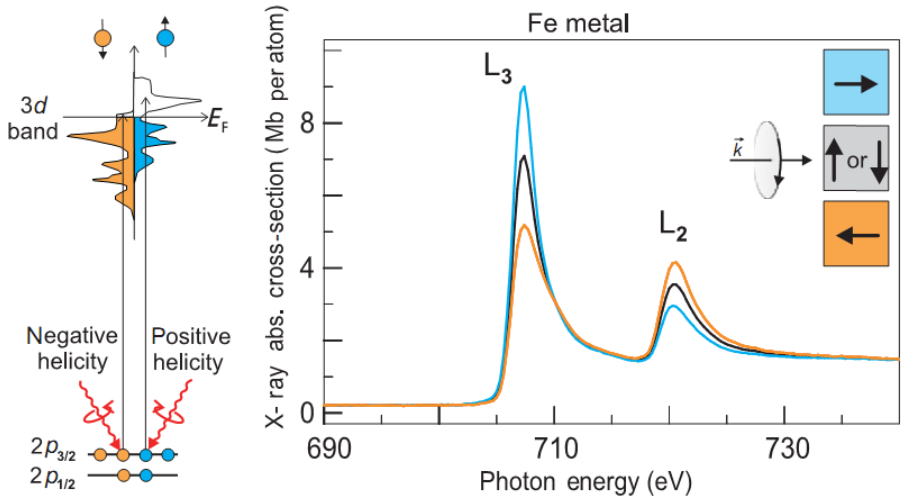

Figure 2.12 Illustration of an XMCD measurement, for L-edge absorption of a 3d transition metal. [9, 10] The left panel is explained in the text. The right panel shows Fe L-edge XAS spectra obtained with right-circularly polarized x-rays for different orientations of the magnetization (arrows inside the squares) relative to the photon helicity.

The principle of XMCD stems from the conservation of angular momentum. As shown in Fig.2.12, a right-circularly polarized photon (labeled "positive helicity" in the figure), which has angular momentum $+\hbar$, excites a core electron and transfers its angular momentum to it. Hence, the angular momentum of the electron has to change, leading to the well-known selection rules for optical transitions. The photon angular momentum is transferred to the orbital motion of the electrons, leaving the electron spin unchanged. However, if the electron is initially in a spin-orbit split state, for example a $2p_{1/2}$ (L_2-edge) or $2p_{3/2}$ (L_3-edge) core level, the angular momentum of the photon can be transferred partly to the spin of the electron via spin-orbit coupling. Hence, the excited electrons are spin polarized. For the $2p_{3/2}$ (L_3-edge) core level, the absorption of right-circularly polarized photons produces excited electrons with mostly spin up. This is illustrated by the arrow indicating a transition into the unoccupied spin up subband in the left panel of Fig. 2.12. The left-circularly polarized photon ("negative helicity"), which has opposite angular momentum ($-\hbar$), transfers the opposite angular momentum to the electrons, resulting in excited electrons with opposite spin polarization. Since the $2p_{1/2}$ (L_2) and $2p_{3/2}$ (L_3) levels have opposite spin-orbit coupling ($m_j = m_l - m_s$ and $m_j = m_l + m_s$, respectively), the spin polarization of the

excited electrons is also opposite at the two edges. For transition metal ferromagnets, with a 3d band that is spin polarized, this 3d band acts as a spin detector. If the excited electrons have a spin polarization for which the unoccupied DOS is high (low), a strong (weak) absorption signal results. This difference in the detected absorption between left- and right circularly polarized light (or opposite magnetization directions) produces the XMCD signal (left panel of Fig.2.12).

References

1. C. Boubeta, J. Costa-Kramer and A. Cebollada, J. Phys-Condens. Mater. **15**, R1123 (2003).
2. J. F. Lawler, R. Schad, S. Jordan and H. van Kempen, J. Magn. Magn. Mater. **165** (1-3), 224 (1997).
3. G. Binnig, H. Rohrer, C. Gerber and E. Weibel, Phys. Rev. Lett. **49** (1), 57 (1982).
4. I. Giaever, Phys. Rev. Lett. **5** (4), 147 (1960).
5. G. Binnig, C. F. Quate and C. Gerber, Phys. Rev. Lett. **56** (9), 930 (1986).
6. https://www.maxlab.lu.se/node/38
7. T. C. Chiang and F. Seitz, Annalen der Physik **10** (1-2), 61 (2001).
8. C. J. Powell and A. Jablonski, J. Phys. Chem. Ref. Data 28 19 (1999).
9. *Magnetism* (Springer Berlin Heidelberg, 2006), Vol. 152, pp. 351.
10. C. T. Chen, Y. U. Idzerda, H. J. Lin, N. V. Smith, G. Meigs, E. Chaban, G. H. Ho, E. Pellegrin and F. Sette, Phys. Rev. Lett. **75** (1), 152 (1995).

CHAPTER 3

The multi-step tunneling analogue of conductivity mismatch in organic spin valves

We present an experimental study of C_{60}-based spin valves and model their behaviour with spin-polarized tunnelling via multiple intermediate states with a Gaussian energy distribution. We show that, analogous to conductivity mismatch in the diffusive regime, the magnetoresistance decreases with the number of intermediate tunnel steps, regardless of the value of the spin lifetime. This mechanism has been largely overlooked in previous studies of organic spin valves. In addition, using measurements of the temperature and bias dependence of the magnetoresistance, we identify inhomogeneous magnetostatic fields resulting from interfacial roughness as a source for spin relaxation and dephasing. These findings constitute a comprehensive understanding of the processes underlying spin-polarized transport in these structures, and shed new light on previous studies of organic spin valves.

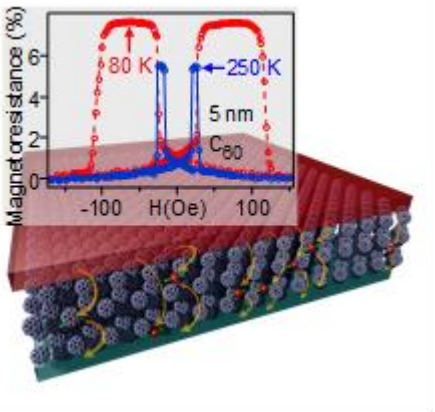

This chapter has been published, in slightly modified form, as T.L.A. Tran, T.Q. Le, J.G.M. Sanderink, W.G. van der Wiel, and M.P. de Jong, Adv. Funct. Mater. 22 (2012) 1180.

3.1 Introduction

Controlling and probing charge carrier spin polarization via electrical means is an attractive route towards the development of practical semiconductor spintronic devices,[1, 2] which are expected to have a strong impact on future information processing and storage technologies. Considerable success has been obtained over the last number of years in the field of *inorganic* semiconductor spintronics, with the demonstration of, for example, the creation and detection of a robust spin polarization in silicon at room temperature.[3] Key to this success is the growing understanding of the physical mechanisms that govern the spin-dependent behaviour of charge carriers in ferromagnetic-metal/semiconductor heterostructures,[2] and in particular of the practical limitations[4] for spin-polarized charge carrier injection and detection using ferromagnetic metal contacts, *e.g.* conductivity mismatch in the diffusive transport regime.[5]

The field of *organic* semiconductor spintronics[6-8] is lagging behind considerably in this respect, as the physics underlying spin-polarized transport in organic devices remains somewhat elusive. This is unfortunate, since carbon-based, organic semiconductors offer a number of unique advantages,[6, 7] such as potentially very long spin lifetimes,[9, 10] bottom-up fabrication relying on self-assembly, and non-stringent requirements for interface formation and film growth, which allow for, for example, vertical stacks comprising alternating layers of ferromagnetic metals and molecular semiconductors. Large magnetoresistance effects have been reported in such organic-based vertical spin valves,[11] comprising *e.g.* thin films of organic molecules[7] and fullerenes,[12-14] in several cases also at room temperature.[12, 15] As is fairly well established by now, the electronic structure of the hybrid interfaces plays an important role.[16, 17] It remains unclear, however, if the limitations for spin-polarized charge injection and detection in inorganic semiconductors are applicable to organic spin valves as well, since these often show electrical characteristics that are indicative of multi-step tunnelling.[7, 18, 19] In this regime, charge carriers tunnel via a limited amount of steps involving localized intermediate states in the organic semiconductor,[19] and a description in terms of diffusive transport fails. Nevertheless, the junction magnetoresistance (JMR) is found to be very sensitive to the thickness of the organic semiconductor layer, and the suppressed JMR in the transition from tunnelling transport to a regime limited by bulk hopping conduction has been attributed to “conductivity mismatch” by

several authors.[13, 18, 20] Another issue that remains subject to debate is how spin relaxation and dephasing take place in the organic semiconductor, and how this affects the JMR. Spin precession in the random hyperfine fields of hydrogen nuclei has been shown to play an important role in the phenomenon of organic magnetoresistance,[21] and has been proposed to affect the JMR of organic spin valves.[19]

In this chapter, we address these important issues using a joint experimental and modelling study of vertical spin valves comprising ultrathin (up to 20 nm) C_{60} layers. We show that multi-step tunnelling leads to a behaviour analogous to conductivity mismatch,[5] in the sense that the inclusion of an increasing number of intermediate tunnelling steps results in a more and more spin-independent junction resistance, regardless of the spin lifetime and spin diffusion length. This previously overlooked fact places numerous published studies on organic spin valves in an entirely new light, including those on similar junctions based on C_{60}.[12, 13] Moreover, it explains the salient features of such devices, namely a strong dependence of the JMR on the organic layer thickness and on temperature, and reconciles the expectation of very long spin lifetimes in organic semiconductors with the relatively short length scales over which a finite JMR is observed.[7] Regarding these potentially long spin lifetimes, C_{60} is an attractive choice: Since C_{60} molecules are purely composed of carbon, and the 99% predominant ^{12}C isotopes have zero nuclear spin, the effects of the above mentioned hyperfine fields are very small and may be neglected.[22, 23] Here we show, however, that spin relaxation and dephasing nevertheless play a role, and propose that inhomogeneous magnetic fields due to finite interfacial roughness are the cause of this.

3.2 Experiments

Our devices were prepared *in-situ* in an ultra-high vacuum chamber (base pressure 10^{-10} mbar). Metals were deposited by e-beam evaporation (rate ~1 Å s^{-1}), and C_{60} was evaporated from a Knudsen cell at ~400°C (rate ~0.25 Å s^{-1}). The layer stacks were grown onto single-crystalline Al_2O_3 substrates (11×11 mm^2) held at room temperature. Twelve identical junctions, with an area of 0.25×0.3 mm^2, were fabricated on each substrate in a cross-bar geometry using shadow masks (please refer to section 2.1.2 in Chapter 2 for detail . The junctions consisted of the following layer stack: Co(bottom electrode, 8 nm)/Al_2O_3(2 nm)/C_{60} (d_C

nm)/$Ni_{81}Fe_{19}$(15 nm). Reference magnetic tunnel junctions, without C_{60}, were fabricated in parallel with C_{60}-containing junctions in every run (the apparatus allows for parallel fabrication of several devices with different layer structure using shadow masks). The Al_2O_3 tunnel barriers were formed by depositing 1.5 nm Al, followed by oxidation in an oxygen plasma at 100 mTorr, without breaking vacuum. The film thickness was monitored by quartz crystal oscillators, and verified with atomic force microscopy (AFM) measurements. The surface morphology was also characterized by AFM.

Junction resistances versus magnetic field (*R–H*) at different bias voltages, and current – voltage (*I–V*) measurements at constant applied magnetic field (corresponding to parallel- and antiparallel magnetization of top- and bottom electrodes) were measured using a four-point probe technique with a Keithley 2400 source meter. The magnetic field was applied parallel to the sample surface. The samples were rotated with respect to the magnetic field such that sharp switching behaviour was observed in the MR traces, (magnetization along the easy axis of both bottom- and top electrode). The measurements were performed within a temperature range that extended from room temperature down to 5K, using a liquid He flow cryostat.

3.3 Multi-Step Tunnelling Calculations

We will proceed now with a description of our model, and then turn to a comparison with our experimental results. When the C_{60} thickness d_C is well below 10 nm, the charge transport can be described in a fairly straightforward manner, in terms of a superposition of direct- and two-step tunnelling. We use the model as developed by Schoonus *et al.*[19] as a starting point, with several additions as outlined below.

3.3.1 Spin Polarized Tunnelling via an Intermediate State

The model of Schoonus *et al.*[19] considers two-step tunnelling processes, in our case involving intermediate states in the C_{60} layer, in addition to direct tunnelling across a composite Al_2O_3/C_{60} barrier. In a two-step process (see Fig.3.1), electrons tunnel from the first ferromagnetic (FM) electrode (0), with tunnel spin polarization (TSP) p_0, into an intermediate state (1) within the C_{60} layer with time-

averaged occupation numbers $n\uparrow$ / $n\downarrow$ for spin up / down electrons, and subsequently into the second FM electrode (2), with TSP p_2. Back-tunnelling processes are also considered, assuming a Fermi-Dirac distribution $f(E)$ and constant density of states (DOS) for the FM metals (this is a somewhat oversimplified but reasonable approximation for low bias voltages). The occupation number of a certain intermediate state in the C_{60} layer is determined by the equality of the inbound- and outbound tunnelling rates under steady state conditions, $J_{01} = J_{12} = J_{two\text{-}step}$. The parameters that enter the model are p_0 and p_2, the thickness d_A and d_C of the Al_2O_3 and C_{60} layers, respectively, and the extinction coefficients of evanescent states κ (for Al_2O_3) and γ (for C_{60}). The extinction coefficients depend in turn on the barrier height U and the effective mass m_e in the evanescent state, via *e.g.* $\gamma = 2\sqrt{2m_e U}/\eta$, where $\hbar$ is the reduced Planck constant. Further details can be found in Ref. [19].

The effects of two-step tunnelling via an intermediate state on the magnetotransport properties of the junctions can be described as follows. Considering a parallel magnetization alignment for electrodes (0) and (2), the tunnel current density $J_{01\uparrow P}$ (with the label "*P*" for parallel magnetization) of majority spin (up) electrons flowing out of the FM contact (0) into the intermediate state (1) at a distance d from the Al_2O_3/C_{60} interface, is given by:

$$J_{01\uparrow P} \propto \tfrac{1}{2}(1+p_0)(1-n_{\uparrow P})e^{-(\kappa d_A+\gamma d)} f(E_F) - \tfrac{1}{2}(1+p_0)n_{\uparrow P}e^{-(\kappa d_A+\gamma d)}(1-f(E_F)), \quad (3.1)$$

which is composed of a forward tunnelling current proportional to (1- $n_{\uparrow P}$) and a back tunnelling current proportional to $n_{\uparrow P}$, while $\tfrac{1}{2}(1+p_0)$ represents the fraction of the total current (due to both spin up and spin down electrons) consisting of spin up electrons tunnelling out of the FM contact (0) at E_F. Here, the transmission of electrons through the Al_2O_3 and C_{60} layers, with thickness d_A and d_C, scales with the extinction coefficients for evanescent states κ and γ, respectively. The extinction coefficients, which depend on the barrier height and the effective mass in the evanescent state, can be estimated from measurements of

the tunnel resistance (in the low bias, Ohmic regime) as a function of layer thickness.

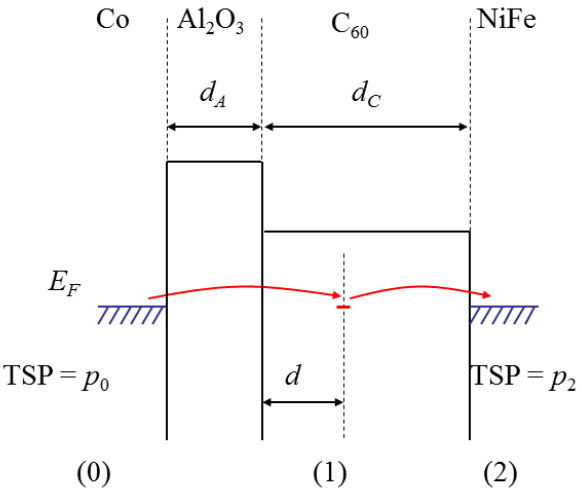

Figure 3.1 A two-step tunnelling event, involving an electron tunneling out of the Co electrode (0) into an intermediate state (1) in the C_{60} layer and subsequently into the NiFe counter electrode (2).

For a certain bias voltage V applied over the junction (with a polarity such that electrons tunnel from electrode (0) via intermediate sites (1) into electrode (2)), the current density $J_{12\uparrow P}$ of carriers flowing out of the localized site in the C_{60} layer into FM contact (2), with TSP p_2, is

$$J_{12\uparrow P} \propto \tfrac{1}{2}(1+p_2)n_{\uparrow P}e^{-\gamma(d_C-d)}(1-f(E_F+eV))- \tfrac{1}{2}(1+p_2)(1-n_{\uparrow P})e^{-\gamma(d_C-d)}f(E_F+eV), \quad (3.2)$$

where e is the electron charge. Under steady state conditions, $J_{01\uparrow P} = J_{12\uparrow P} = J_{\uparrow P}$, which yields $n_{\uparrow P}$ such that the current density for tunnel processes involving intermediate sites at a distance d from the Al_2O_3 electrode can be evaluated:

$$n_{\uparrow P} = \frac{\tfrac{1}{4}(1+p_0)e^{-(\kappa d_A+\gamma d)} + \tfrac{1}{2}(1+p_2)e^{-\gamma(d_C-d)}f(E_F+eV)}{\tfrac{1}{2}(1+p_2)e^{-\gamma(d_C-d)} + \tfrac{1}{2}(1+p_0)e^{-(\kappa d_A+\gamma d)}}. \quad (3.3)$$

Similar expressions can be obtained for the minority spin current $J_{01\downarrow P}$ related to $n_{\downarrow P}$, upon replacing p_0 with $-p_0$ and p_2 with $-p_2$, and for the antiparallel (AP) magnetization configuration, upon setting p_0 = -p_0 while keeping p_2 unchanged (or *vice versa*). The JMR, for tunnelling via an intermediate site at a distance d within the C_{60} layer, can then be evaluated as JMR(d) = (J_P - J_{AP})/ J_{AP} , (note that this is equivalent to ($R_{AP} - R_P$)/R_P, where R is the resistance) with J_P = $J\uparrow_P + J\downarrow_P$, and $J_{AP} = J\uparrow_{AP} + J\downarrow_{AP}$.

After determining the equations for the spin polarized two-step tunnelling currents as a function of the distance d of the intermediate site from the Al_2O_3/C_{60} interface, the JMR resulting from tunnelling via en ensemble of states with a spatially homogeneous distribution is found by integrating the expressions for the current densities with respect to d. The magnetoresistance that results is considerably lower than that due to *direct* tunnelling of electrons between contacts (0) and (2), given by $2p_0p_2/(1- p_0p_2)$. The reason for this is that, in addition to the TSPs of the electrodes, the spin dependent occupation numbers also determine the tunnelling rates.

Let us discuss a specific hypothetical case that illustrates this effect, and for which the analysis is especially simple. Consider a symmetric system, consisting of two identical FM electrodes with $p_0 = p_2 = p$, and a single localized state in the barrier, located exactly halfway between the electrodes. The spin dependent occupation numbers of the intermediate state are determined by the balance between inbound- and outbound tunnelling events. Due to the symmetry of the system when the magnetization configuration is *parallel*, the transmission probabilities for tunnelling into and out-of the localized state are equal. If we disregard back tunnelling, and set the bias voltage to zero, the equations for the tunnelling rates in the parallel magnetization configuration are:

$$J_{01\uparrow P} \propto \tfrac{1}{2}(1+p)(1-n_{\uparrow P})e^{-\gamma d} = J_{12\uparrow P} \propto \tfrac{1}{2}(1+p)n_{\uparrow P}e^{-\gamma(d_C-d)} = J_{\uparrow P}, \qquad (3.4)$$

$$J_{01\downarrow P} \propto \tfrac{1}{2}(1-p)(1-n_{\downarrow P})e^{-\gamma d} = J_{12\downarrow P} \propto \tfrac{1}{2}(1-p)n_{\downarrow P}e^{-\gamma(d_C-d)} = J_{\downarrow P}. \qquad (3.5)$$

Since the intermediate state is located exactly halfway between the electrodes, *i.e.* (d_C – d)= d, the exponential terms are equal. Therefore, since $J_{01\uparrow P}=J_{12\uparrow P}$ and $J_{01\downarrow P}=J_{12\downarrow P}$, it follows that $n\uparrow_P = n\downarrow_P = ½$, for any value of p<1. In the case p=1 the spin down tunnelling rates are equal to zero, and hence $n\uparrow_P = ½$, $n\downarrow_P = 0$. When the electrodes are magnetized in the *antiparallel* configuration, the equations are:

$$J_{01\uparrow AP} \propto ½(1-p)(1-n_{\uparrow AP})e^{-\gamma d} = J_{12\uparrow AP} \propto ½(1+p)n_{\uparrow AP}e^{-\gamma(d_C-d)} = J_{\uparrow AP}, \quad (3.6)$$

$$J_{01\downarrow AP} \propto ½(1+p)(1-n_{\downarrow AP})e^{-\gamma d} = J_{12\downarrow AP} \propto ½(1-p)n_{\downarrow AP}e^{-\gamma(d_C-d)} = J_{\downarrow AP}, \quad (3.7)$$

where the magnetization of electrode (0) has been flipped. It follows that $n\uparrow_{AP} = ½(1-p)$ and $n\downarrow_{AP} = ½(1+p)$, for p<1. For p=1, the current in the antiparallel configuration is always equal to zero, due to the terms (1-p) in Eqs.3. 6 and 7. In addition, $n\uparrow_{AP}$ =0, $n\downarrow_{AP}$=1 for p=1, since electrode (0), now magnetized in the opposite direction, contains no spin up electrons at the Fermi level. Hence the magnetoresistance for p=1 is infinite, as is the case for direct tunnelling between to 100% polarized electrodes. However, for p < 1, inserting the spin dependent occupation numbers into Eqs. 3.4 - 7 for the tunnelling rates gives a magnetoresistance $(J_P - J_{AP})/ J_{AP}$, with $J_P = J\uparrow_P + J\downarrow_P$ and $J_{AP} = J\uparrow_{AP} + J\downarrow_{AP}$, proportional to $p^2/(1-p^2)$, *i.e.* half that of direct tunnelling between the two electrodes (as was also pointed out by Schoonus *et al.*[19]).

3.3.2 Tunnelling via a Gaussian DOS of Intermediate States

We consider two-step tunnelling via a Gaussian DOS of intermediate C_{60}-derived states, centred at the LUMO of C_{60}, in contrast to the uniform energetic distribution of states in the model of Schoonus *et al.* A similar picture is used routinely to describe charge transport in the hopping regime in (disordered) organic solids.[24, 25] From previous experiments, the position of the LUMO with respect to E_F is well known: The high electron affinity of solid C_{60}, equal to 4.0 eV,[26-28] leads

to Fermi level pinning on metallic substrates with a work function of 4.5 eV or smaller,[29] as is the case for the present electrodes, Co/Al_2O_3 and NiFe.[30] We set the Gaussian width, determined by inhomogeneous broadening, to a realistic value of 0.3 eV (full width at half maximum) via the parameter σ (see Eq. 1), while the energy difference E_F - E_{LUMO} is set to 0.5 eV. Figs. 3.2a and 3.2b show schematic representations of two-step tunnelling processes via a Gaussian DOS of intermediate states. Applying a bias voltage tilts the potential within the C_{60} layer, such that the DOS of intermediate states aligned with E_F of the electrode from which electrons are expelled becomes a strong function of d. Correspondingly, the current flowing under different bias conditions will involve two-step (or multistep at sufficiently large C_{60} thickness) tunnelling via states that are distributed differently within the C_{60} layer. The two-step tunnel current density $J_{two\text{-}step}$ as a function of d and bias voltage V is:

$$J_{two-step}(V) = J_{two-step}(0) e^{-\left((E_F - E_{LUMO}) - |eV|\frac{d}{d_A + d_C}\right)^2 / \sigma}, \tag{3.8}$$

for electrons tunnelling from the left (Co/Al_2O_3 electrode) to the right (NiFe electrode), meaning under application of a negative potential in our experiments. For the opposite bias polarity, we substitute ($d_C - d$) for d. $J_{two\text{-}step}(0)$, *i.e.* the two-step tunnel current density at zero bias, is calculated using equations 3.1, 3.2 and 3.3.

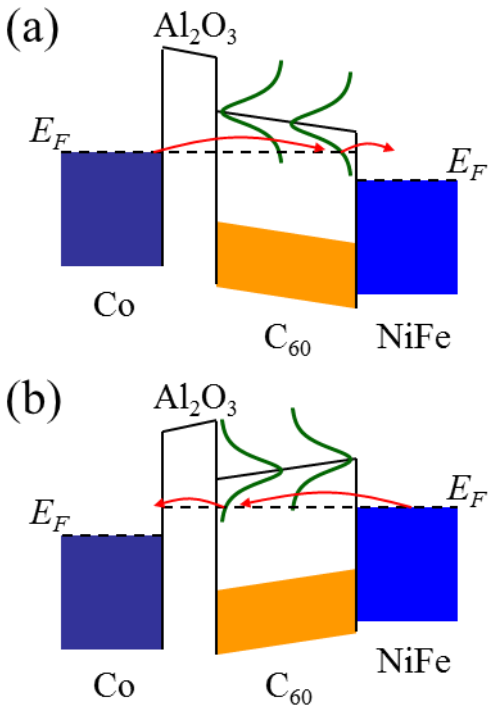

Figure 3.2 Two-step tunnelling via intermediate states with a Gaussian energy distribution centered on the LUMO of C_{60}. Under application of a negative bias voltage (**a**), electrons tunneling out of the Co electrode at E_F encounter an increasing density of intermediate states at an increasing distance from the Al_2O_3 surface. A positive bias (**b**) results in an increased amount of states close to the Al_2O_3 surface for electrons tunneling out of the NiFe electrode.

3.3.3 Tunnelling via Multiple Intermediate States

For increasing C_{60} thickness, the contribution of tunnelling events that involve *more than one* intermediate site in the C_{60} layer will increase, as the transmission probability for individual tunnelling processes drops exponentially with the tunnelling distance. For the sake of illustrating the main effects of tunnelling via multiple intermediate sites on the magnetoresistance, we limit ourselves in the discussion below to two simple cases that can be evaluated easily: (1) that of up to 4 intermediate tunnelling sites within the barrier with *equal*

probability for inbound versus outbound tunnelling (*i.e.* equidistantly placed sites within the barrier), and (2) that of two sites near both electrodes (at the same distance from each electrode) connected via an arbitrary number of uncorrelated "hops" within the C_{60} layer.

3.3.3.1 Multiple equidistant tunnelling sites

When back tunnelling is not taken into account, and only a single barrier (corresponding to the C_{60} layer) is considered, we can easily evaluate the case of equidistant tunnelling events (with the same transmission probability) involving a limited number *i* of intermediate states. The problem to be solved, for arbitrary *i*, is that of the following set of equations:

$$\begin{aligned} & J_{0\uparrow P} \propto \alpha\left(1-n_{1\uparrow P}\right)= \\ & \ldots \\ & J_{i-2,i-1\uparrow P} \propto n_{i-2\uparrow P}\left(1-n_{i-1\uparrow P}\right)= \\ & J_{i-1,i\uparrow P} \propto n_{i\uparrow P}\alpha \end{aligned} \tag{3.9}$$

where the TSP of both electrodes is taken to be equal to *p*, and we define $\alpha = \frac{1}{2}(1+p)$, and $\beta = \frac{1}{2}(1-p)$. To avoid unnecessary complication, we have set the exponential tunnel transmission probability connecting each of the states $n_{\ldots}$ equal to 1, since it drops out of the expression for the JMR anyway. Equivalent sets of equations can be formulated for spin down electrons (substituting $\alpha \rightarrow \beta$ for both electrodes), as well as the antiparallel magnetization configuration (substituting $\alpha \leftrightarrow \beta$ for only one electrode).

It is easy to see that a solution that fulfils $0 < n < 1$ for the antiparallel configuration is $n_{\ldots\uparrow AP} = \beta$, and $n_{\ldots\downarrow AP} = \alpha$, for an arbitrary number of sequential tunnelling events (here we use the convention that the sign of the TSP of electrode (0) is changed when changing from a parallel to an antiparallel configuration). In fact, it turns out that this is the *only* solution for the AP configuration. Regardless of the amount of tunnel steps, the AP currents thus become $J_{\uparrow AP} = J_{\downarrow AP} \propto \alpha\beta$. The

solutions for $n_{\ldots P}$ are more complicated, but can nevertheless be evaluated analytically for $i \leq 3$, while we use a simple graphical procedure for $i = 4$ to solve the equation for $n_{\ldots P}$ including terms $(n_{\ldots P})^3$. The so obtained curves for J_P and J_{AP} as a function of the tunnel spin polarization p of the electrodes are shown in Fig. 3.3a, while the JMR as a function of the number of tunnelling steps for $p = 0.3$ is shown in Fig. 3.3b.

These calculations show that the magnetoresistance continues to drop upon the inclusion of additional tunnelling steps, as may be intuitively expected. This leads to an overall junction resistance that becomes more and more spin-independent, which is qualitatively similar to the conductivity mismatch problem in the diffusive regime.[5] In a more realistic approach, one should consider also events with *unequal* transmission coefficients for inbound and outbound tunnelling, as well as back-tunnelling events, which will further strongly reduce the JMR. It is important to note at this point that we have not yet included any effects of a finite spin lifetime in the intermediate states (which certainly plays a role in reality); the reduction of the magnetoresistance discussed above is *solely* due to the requirement of continuity of the tunnel current, which determines the spin-dependent occupation numbers, and therefore the JMR.

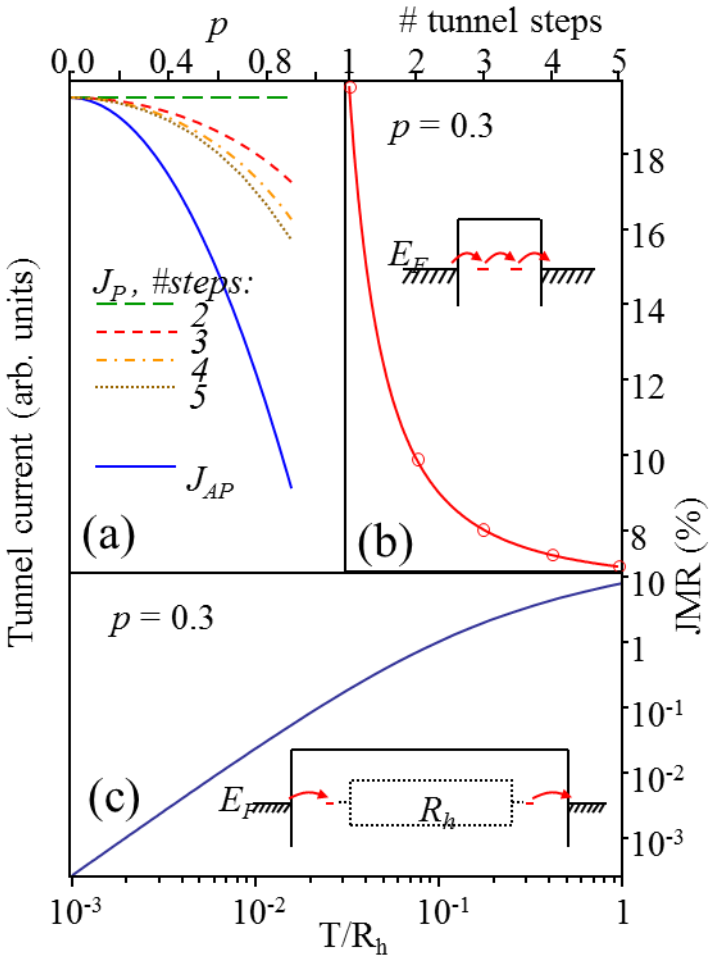

Figure 3.3 (**a**) Calculated relative tunnel currents in the parallel (J_P) and antiparallel (J_{AP}) magnetization configuration for different numbers of tunneling steps as a function of the tunnel spin polarization p in both ferromagnetic electrodes. (**b**) JMR as a function of the number of tunnel steps for p=0.3. The solid line is a guide to the eye, and the inset depicts a three-step tunneling process. (**c**) JMR versus the ratio of the transmission probability T for tunneling into/out-of interfacial states, and the dimensionless constant R_h proportional to the bulk hopping resistivity.

3.3.3.2 Interfacial Tunnelling Sites Connected via a Large Number of Uncorrelated Hops

We consider the case of two sites n_1 and n_2 at a distance d from each opposing FM electrode (both electrodes having a TSP equal to p), connected via different pathways involving a large number of (uncorrelated) hops via localized sites in the C_{60} layer. If we allow (thermally activated) hopping via a large number of different sites, electrons will travel via an ensemble of random paths, and keeping track of the spin dependent occupation numbers of neighbouring sites is no longer very meaningful. Instead, we may model the transmission between the sites as $1/R_h$, with R_h a dimensionless constant that is proportional to the (spin independent) electrical resistivity of the C_{60} layer in the hopping transport regime. The set of equations to be solved for obtaining the n's and J's then becomes:

$$\begin{aligned} J_{01\uparrow P} &\propto \alpha\left(1-n_{1\uparrow P}\right)T = \\ J_{12\uparrow P} &\propto n_{1\uparrow P}\left(1-n_{2\uparrow P}\right)\,1\!\!\diagup\!\!R_h = \\ J_{23\uparrow P} &\propto n_{2\uparrow P}\alpha T, \end{aligned} \tag{3.10}$$

where $T = e^{-\gamma d}$ denotes the transmission probability for tunnelling into/out-of states n_1 and n_2. Again, similar equations should be solved for the different spin currents and magnetization configurations. Since only tunnelling to/from the sites close to the barrier is spin dependent, the JMR continues to drop upon increasing R_h (see Fig. 3.3c).

3.4 Magnetotransport experiment results

3.4.1 Resistance and JMR versus C_{60} Thickness

Upon increasing the C_{60} thickness stepwise from 0 to 7 nm, the resistance of our junctions increases strongly, as expected for devices in which transport is limited by tunnelling. Above a thickness of 2-3 nm, the resistance increase with d_C levels off, as two-step tunnelling via an intermediate state in the C_{60} layer becomes the dominant transport mechanism instead of direct tunnelling between the Co and NiFe electrodes (see Fig. 3.4). The solid line is obtained by a fit in which the

current is composed of a weighted average of direct tunnelling and two-step tunnelling contributions (Eq. (1) of Ref. 19). For the Al_2O_3 barrier, we estimate an extinction coefficient of evanescent states $\kappa \approx 3$ nm^{-1}, based on measurements of the resistance area product as a function of thickness of similar Al_2O_3 tunnel contacts,[31] while the thickness of the barrier d_A is 2 nm. These parameters are inserted into the fit function, which yields $\gamma \approx 1.36$ nm^{-1} for the extinction coefficient in C_{60}, and $N = 4.6 \cdot 10^{-4}$ nm^{-1} for the weighting factor that determines the relative contributions of direct- and two-step tunnelling events. The latter is proportional to the density of intermediate states within the C_{60} layer (hence the dimension nm^{-1}), via which two-step tunnelling may proceed. These parameters are used below in calculations of, *e.g.*, the JMR. The *I-V* and conductance $G = dI/dV$ characteristics (see insets in Fig. 3.4 for room-temperature measurements), as well as their temperature dependence (Fig.3.5), are consistent with tunnelling being the limiting mechanism for charge transport.

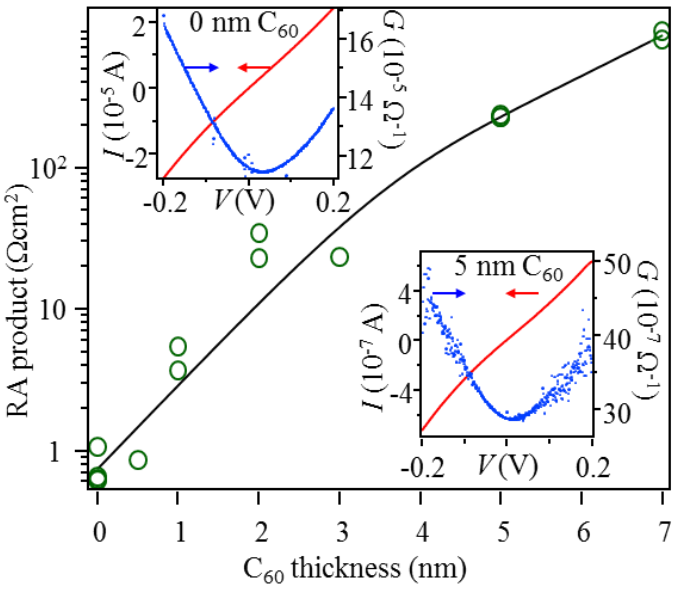

Figure 3.4 RA product (open circles) of a set of junctions with increasing C_{60} thickness measured at room temperature and 20 mV bias voltage. The insets show room temperature *I-V* and conductance (*G*) curves of a reference device without C_{60} interlayer (upper left corner) and a junction with a 5 nm thick C_{60} layer (lower right corner).

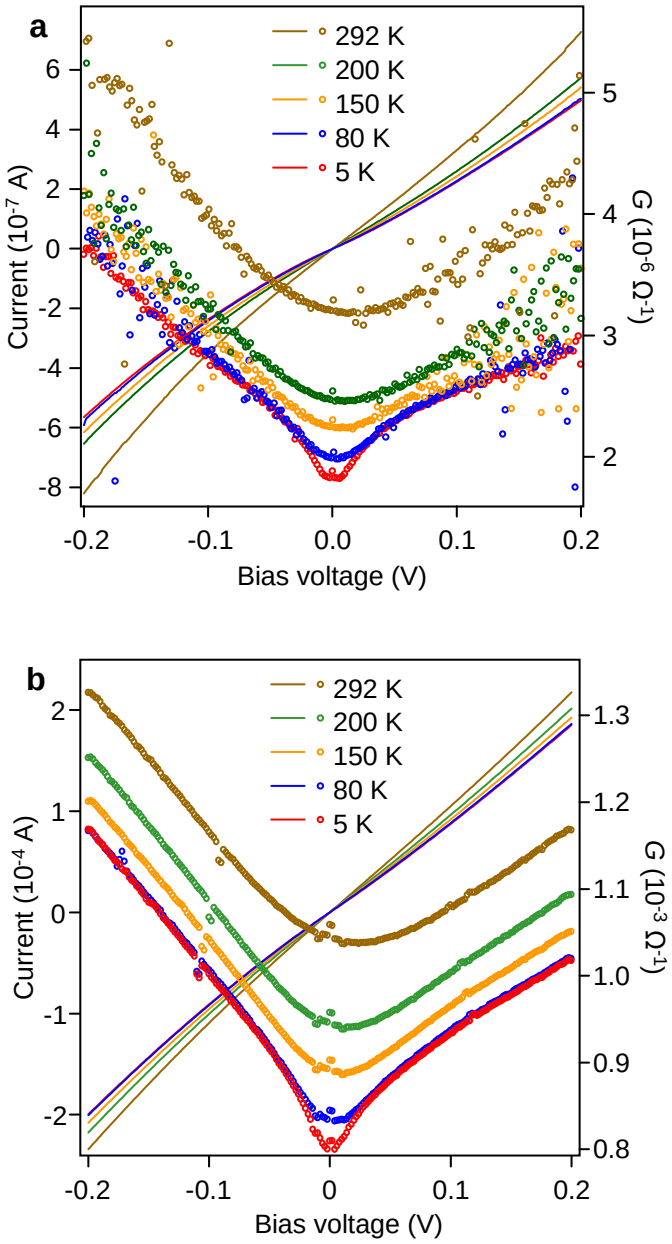

Figure 3.5 Temperature dependent *I-V* curves (solid lines) and conductance *G* versus voltage curves (open circles) of a junction with 5 nm C_{60} (**a**) and a junction without C_{60} (**b**).

The magnetoresistance of the junctions, measured at room temperature (293 K) and 5 K at a bias voltage of 20 mV, is plotted versus the C_{60} thickness in Fig. 3.6. The inset shows traces of the resistance versus the magnetic field of a device with 5 nm C_{60} measured at 250 K and 80 K. Also shown are calculated JMR curves for a superposition of direct- and two-step tunnelling (dashed line), and 2-step tunnelling only (dash-dotted line). In the calculations, we have set the tunnel spin polarization (TSP) for both ferromagnetic electrodes equal to 0.3, which is close to the experimentally obtained values for Co/Al_2O_3 and $NiFe/Al_2O_3$.[31-33] It is evident that the inclusion of a C_{60} layer in the MTJ stack leads to a reduction of the JMR, due to tunnelling via intermediate states in the C_{60} for $d_C \geq 2$, and a somewhat reduced TSP at the $NiFe/C_{60}$ interface compared to that of $NiFe/Al_2O_3$, leading to a modest reduction of the JMR even for C_{60} layers as thin as 1 nm. Junctions with 0.5 nm C_{60}, well below the threshold for closed-layer formation, show a JMR identical to that of reference MTJs without C_{60}, which is to be expected since the tunnel current will flow predominantly in those regions of the junction where the C_{60} is absent. For C_{60} layers with a thickness above 1 nm, the reduced JMR thus indicates that tunnelling of electrons across a composite Al_2O_3/C_{60} is the dominant transport mechanism.

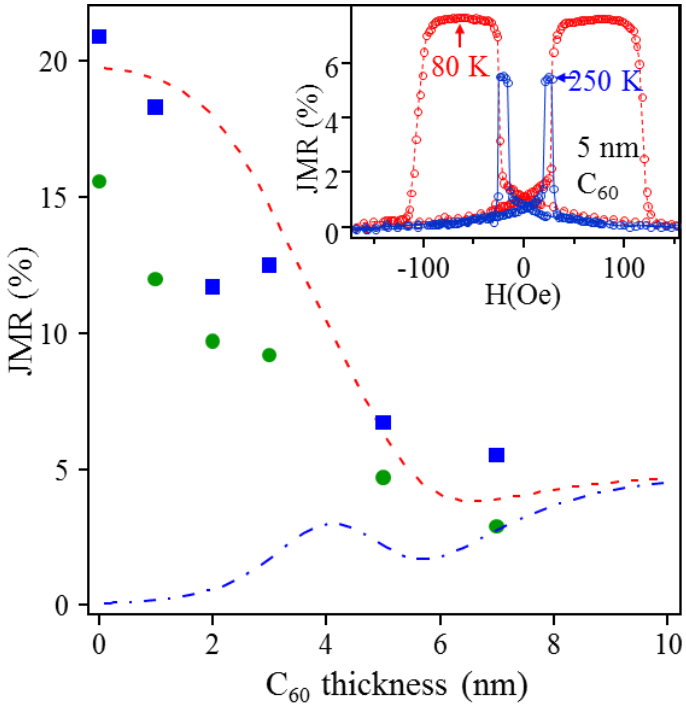

Figure 3.6 JMR as a function of C_{60} thickness. Data points are shown for measurements performed at room temperature (solid circles) and 5 K (solid squares). The dashed line is the calculated JMR for a combination of direct- and two-step tunneling, while the dash-dotted line corresponds to two-step tunneling only. The inset shows traces of the resistance versus magnetic field of a junction with 5 nm C_{60} (plotted as a JMR value), measured at 250 K (blue) and 80 K (red).

The calculated JMR curves in Fig. 3.6 predict a reduction of the magnetoresistance by about a factor of 4 in the two-step tunnelling regime (d_C = 5 and 7 nm) as compared to direct tunnelling across an Al_2O_3/C_{60} barrier ($d_C \leq 1$ nm), which is fairly consistent with the experimental data. The calculated JMR due to two-step tunnelling alone (the dash-dotted line in Fig. 3.6) shows some additional features. The very low JMR for small C_{60} thickness is due to the fact that the tunnel current via the intermediate site is determined by the transmission through the Al_2O_3 barrier, such that the site occupation numbers are always fairly similar regardless of the electron spin or the magnetization configuration (parallel or antiparallel).[19] The dip in the two-step JMR curve at intermediate thickness is due to back-tunnelling processes, which lead to a significantly higher forward tunnelling rate in the antiparallel state than the parallel state for sites close to the Al_2O_3 electrode for intermediate C_{60} thickness (see Fig. 3.7a,b).

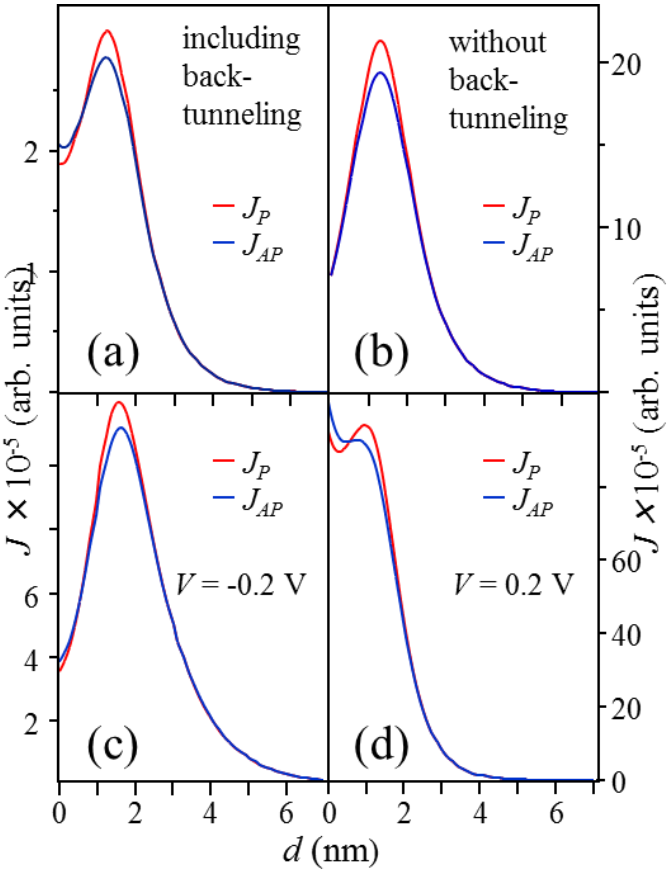

Figure 3.7 Calculated relative two-step tunneling current densities as a function of the distance *d* of the involved intermediate states from the Al_2O_3 barrier, for a 7 nm thick C_{60} layer. (**a**) Two-step tunneling current density including back tunneling. (**b**) As **a**, but without back tunneling. (**c**) Two-step tunneling current density calculated with a Gaussian energy distribution of intermediate states and a negative bias voltage of 200 mV. (**d**) As **c**, but with a positive bias voltage of 200 mV.

We have also studied junctions comprising considerably thicker C_{60} interlayers, with d_C = 10 and 20 nm. These devices exhibit strongly non-linear *I-V* curves (Fig.3.8), similar to those observed previously for C_{60}-based spin valves with relatively high C_{60} thickness,[12, 13] which is indicative for transport limited by bulk hopping conduction instead of tunnelling via a small number of intermediate steps. We do not observe any (room-temperature) magnetoresistance in these devices, consistent with calculations of the JMR as a function of an increasing amount of intermediate tunnelling steps (see Fig. 3.3a,b), and with the notion that the JMR becomes negligible when the hopping resistivity dominates charge

transport across the junction (see Fig. 3.3c). A very important conclusion is that the observation of a vanishing magnetoresistance at a certain thickness of an organic interlayer cann*ot* be simply used to estimate the spin diffusion length in that layer. Even for an *infinitely long* spin diffusion length, our analysis shows that the JMR will decay to negligible values if the number of tunnelling steps becomes sufficiently large.

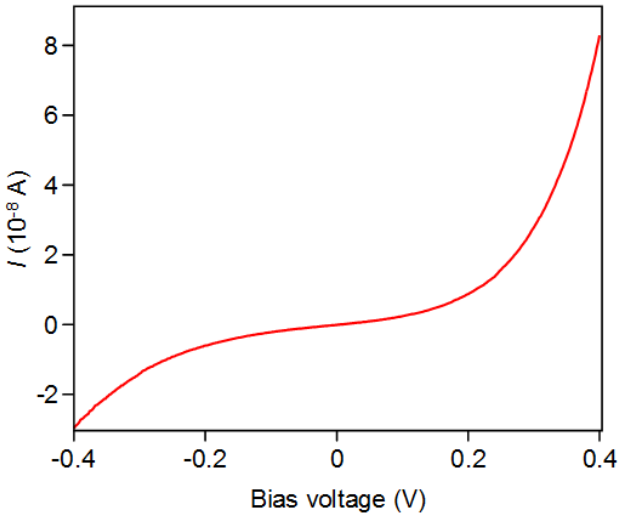

Figure 3.8 *I-V* curve of a junction with 10 nm C_{60}.

3.4.2 Temperature Dependence of the Resistance and JMR

The normalized device resistance as a function of temperature is shown in Fig. 3.9a. The stronger temperature dependence of the resistance and JMR for junctions with larger d_C shows that thermal activation becomes more important in those junctions, consistent with tunnelling via one or more intermediate states. Interestingly, the JMR of junctions with $d_C \geq 2$ nm shows a *non-monotonic* dependence on temperature (see Fig. 3.9b); in particular for the junctions with d_C equal to 5 and 7 nm, the JMR shows a clear maximum at 50 K. This suggests that the temperature dependence of the JMR is affected by competing mechanisms. The first mechanism, responsible for the decreasing JMR with T for $T > 50$ K, is ascribed to the larger contribution of thermally activated two- (or multi-) step

tunnelling processes with increasing temperature. For the second mechanism, spin relaxation and dephasing during occupation of the intermediate site in the C_{60} layer is the most probable candidate. The outbound tunnelling frequency from the intermediate state can be estimated as $\nu_0 \exp\left(-2d\sqrt{2m_eU}/\eta\right)$, where ν_0 is the (material dependent) phonon attempt frequency, U is the barrier height, d is the barrier width, and m_e the effective mass. The effective barrier height is reduced when the electrons gain thermal energy in the intermediate state. This leads to a higher tunnelling frequency, analogous to hopping transport in organic semiconductors.[25, 34] The dwell time of the electrons in the intermediate states will thus increase as the temperature is reduced, which affects the spin relaxation and dephasing in the intermediate site(s). As discussed above, hyperfine interactions are very small in C_{60},[22, 23] and are thus unlikely to play an important role. The importance of spin orbit (SO) coupling for spin relaxation in organic semiconductors is currently under hot debate. Up until recently, the consensus was that SO interactions, which scale with the fourth power of the atomic number, are too weak to be of major importance in organic materials. However, recent theoretical studies have cast doubts on this view.[35, 36] In the work of Yu,[36] the SO coupling was found to be strongly dependent on the molecular structure. To our knowledge, no computational studies of the SO coupling strength in C_{60} are available at this time, such that a quantitative estimate of the associated spin relaxation effects cannot be given.

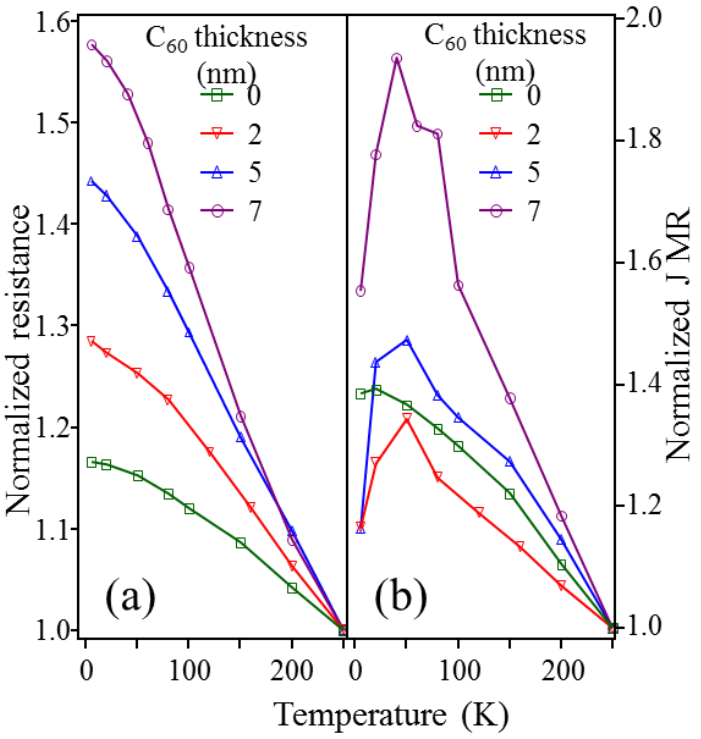

Figure 3.9 Temperature dependence of the resistance and JMR. (**a**) Normalized resistance versus temperature of junctions with different C_{60} thickness between 0 and 7 nm. (**b**) Normalized JMR of the same junctions as in (**a**).

Here, we propose a third mechanism that may limit the spin polarization in the intermediate states, namely spin precession in local, inhomogeneous magnetostatic fields arising from the finite roughness at the interfaces with the ferromagnetic electrodes.[37, 38] Such fields are well known to affect the switching behaviour of metal/insulator/metal magnetic tunnel junctions, in what is usually referred to as Néel or "orange peel" coupling.[39, 40] In addition, it has been suggested recently that roughness-induced fields play a significant role in spin relaxation at interfaces between ferromagnet/tunnel-barrier contacts and silicon.[38] Since the fields are inhomogeneous in magnitude as well as in direction, the resulting random precession of electron spins will lead to a decay of the spin polarization in the intermediate state, if the (temperature-dependent) two-step tunnelling frequency becomes comparable to the Larmor spin precession frequency. The latter

is equal to $g\mu_B B/h$ s^{-1} where g is the spin gyromagnetic ratio, μ_B is the Bohr magneton, B is the inhomogeneous magnetostatic field, and h is Planck's constant.

In our junctions, the intermediate sites involved in two-step (or multistep) tunnelling are located at several nm from the interfaces with the ferromagnets. For a peak-to-peak roughness amplitude of 0.5 to 1 nm, similar to the interfacial roughness in our devices (see Fig. 3.10), calculations by Dash *et al.*[38] show that the local magnetostatic fields are of the order of 100 mT at a distance of up to 10 nm away from the interface. It should be pointed out in passing that in our case not one but *two* ferromagnetic interfaces are present, such that the local magnetic fields, and the associated precession frequency, might be even higher than for the Si-based devices studies by Dash *et al.* The corresponding Larmor precession frequency is of the order of 10^9 Hz. It is interesting to compare this precession frequency, which sets the timescale for spin relaxation in local roughness-induced fields, to an estimate of the tunnelling frequency. The two-step tunnelling processes in our devices involve a distribution of intermediate sites with different tunnelling distances d, resulting in a distribution of different tunnelling rates (see Fig. 3.7). For junctions with 7 nm C_{60}, the peak of the tunnelling rate distribution occurs for intermediate sites located about 1 nm from the Al_2O_3/C_{60} interface. The corresponding tunnelling rate ν_{tun} can be estimated as $\nu_{tun} = \nu_0 \exp(-\gamma d)$, where $d \approx 6$ nm is the outbound tunnelling distance, γ = 1.36 nm^{-1} is the extinction coefficient in C_{60} obtained from the fit in Fig. 3.4, and ν_0 is the phonon attempt frequency. The latter can be estimated as 10^{13} Hz, based on studies of the frequencies of vibrational modes that couple to the LUMO orbitals of C_{60}.[41, 42] Hence, we find a tunnelling frequency of the order of 10^9 Hz, similar to the precession frequency associated with the local roughness-induced fields. For junctions with 5 nm C_{60}, two-step tunnelling occurs mostly for intermediate states close to the Al_2O_3/C_{60} interface, such that the relevant outbound tunnelling distance is about 5 nm, and $\nu_{tun} \approx 10^{10}$ Hz. Since the timescales for two-step tunnelling and relaxation are similar, and the effective barrier height depends on temperature as discussed above, the scenario sketched above is entirely consistent with our observation of a maximum in the temperature dependence of the JMR.

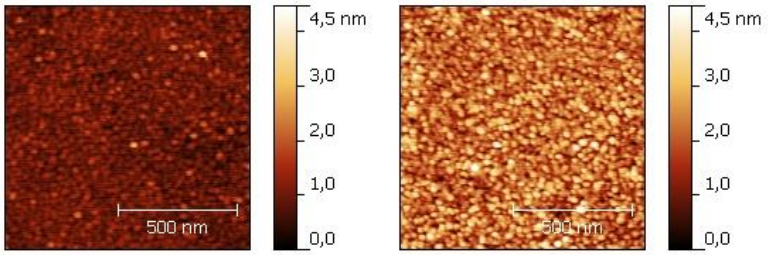

Figure 3.10 AFM images of a Co(8 nm)/Al_2O_3(2 nm) surface (left), with RMS roughness ~0.25 nm, and a Co(8 nm)/Al_2O_3(2 nm)/C_{60}(7 nm) surface (right), with RMS roughness ~0.5 nm.

3.4.3 Bias Voltage Dependent Properties

We now address the evolution of the JMR versus bias voltage for junctions with different C_{60} thickness between 0 and 7 nm (see Fig. 3.11), obtained from *I-V* curves measured in the parallel and antiparallel magnetization configurations. For the junctions with 5 and 7 nm C_{60}, applying larger *negative* bias voltages (electrons tunnelling from Co to NiFe) results in a considerably faster reduction of the JMR as compared to junctions with thinner C_{60} layers. This suggests that two-step tunnelling via intermediate sites in the C_{60} layer, which contributes more strongly for thicker layers, affects the JMR significantly for negative bias voltages, but not for positive bias voltages. Note that since the JMR-versus-bias curves are all similar for junctions with thin (≤3 nm) C_{60} layers, these effects cannot be due solely to changes in the spin-polarized interfacial density of states introduced by replacing the Al_2O_3/NiFe interface with C_{60}/NiFe, which would also influence the JMR of direct tunnelling events.

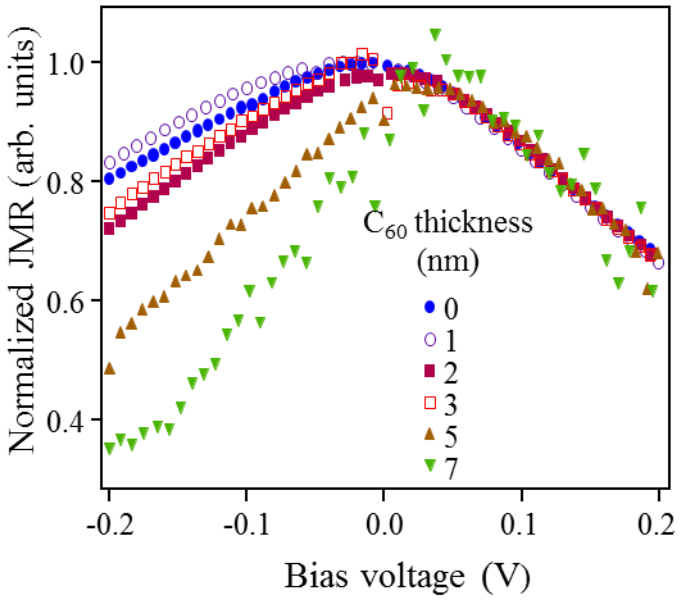

Figure 3.11 Bias dependence of the JMR. Normalized JMR measurements are shown, measured at T = 200 K, as a function of bias voltage for junctions with different C_{60} interlayer thickness

As shown in Fig. 3.7c,d, changing the bias voltage from -0.2 V to 0.2 V introduces a significant asymmetry in the spatial distribution of the intermediate states via which the two-step tunnelling transport takes place, due to the Gaussian energy distribution of states in the gap of C_{60} (see also Fig. 3.2a,b). At negative (positive) bias voltages, the distribution of intermediate states that participate considerably to two-step tunnelling shifts away from (towards) the Al_2O_3 interface. This influences the precession of spins in the inhomogeneous magnetostatic fields resulting from the finite roughness at the ferromagnetic interfaces. Since the C_{60}/NiFe interface has a considerably larger roughness amplitude (see Fig.3.10) than the Co/Al_2O_3 interface, the redistribution of the active two-step tunnelling sites towards the C_{60}/NiFe interface at sufficiently high negative bias might result in higher spin precession frequencies, and thus a larger reduction of the spin polarization in the intermediate state. To test this hypothesis, we have measured magnetoresistance hysteresis loops at T = 5 K and at different bias voltages between -0.2 and 0.2 V for a junction with 5 nm C_{60} (Fig. 3.12a,b).

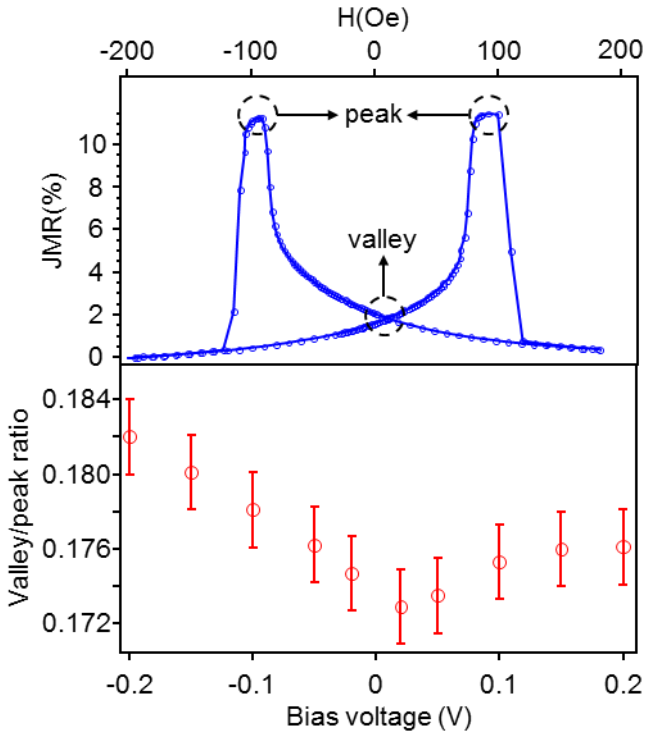

Figure 3.12 Bias voltage dependence of the MR traces. (**a**) MR curve of a junction with 5 nm C_{60} measured at T = 5 K and a bias voltage of 20 mV, where the valley- and peak values are indicated by arrows. (**b**) Valley to peak ratio versus bias voltage. The error bars give a conservative estimate of the uncertainty of determining the valley- and peak values.

Upon application of an external magnetic field aligned with the magnetization direction of the ferromagnets, and thus with the spin polarization of the tunnelling electrons, the initially random spin precession axis will rotate in the direction of the spin polarization vector, since the spins precess around the vector sum of the applied field and the local magnetostatic field. Hence, spin precession in inhomogeneous local fields should be suppressed at sufficiently large external field strengths. This affects the JMR curves of the junctions in a similar way as described earlier for spin precession in local hyperfine fields (Fig. 4 of Ref. 19). Small changes in the shape of the JMR curves of the junction with 5 nm C_{60} were observed upon varying the bias voltage stepwise from -0.2 to 0.2 V, which indeed points to stronger local inhomogeneous magnetostatic fields resulting in more pronounced spin precession effects.

3.5 Conclusions

We have presented a joint experimental and modelling study of C_{60}-based spin valves, and interpreted their behaviour using a superposition of direct and multi-step tunnelling via a Gaussian DOS of intermediate states. We find that, analogous to conductivity mismatch in the diffusive regime, the JMR drops continuously as the amount of intermediate tunnelling steps increases, irrespective of the spin lifetime and spin diffusion length. Consequently, these parameters cannot be extracted simply from the thickness dependence of the JMR of organic spin valves, as has been common practice in the past (see Refs. 6, 7 and references therein). Previously reported values of the spin diffusion length in organic semiconductors thus may have been strongly underestimated.

In addition to the intrinsic loss of the JMR due to multi-step tunnelling, our temperature- and bias dependent measurements of the magnetotransport properties indicate that spin relaxation and dephasing in the intermediate states on the C_{60} molecules also affect the JMR. We propose that the mechanism that underlies this is spin precession in the inhomogeneous magnetostatic fields that arise from finite roughness at the ferromagnetic interfaces, which is supported by measurements of JMR versus magnetic field, recorded at different bias voltages.

Our findings are widely applicable to organic spin valves operating in the multi-step tunnelling regime, with a not too large amount of intermediate hops. Indeed, even for devices with relatively large organic layer thickness (on the order of 100 nm), this description may be a good starting point for modelling the device behaviour. Such devices unexceptionally show a very strong temperature dependence of the magnetoresistance, which is most probably related with the reduction of the hopping rate, and hence the number of hops involved in transport, at low temperature. We expect that further theoretical analysis, for example using Monte Carlo / master equation approaches, will provide additional insights into the operation of these fascinating and promising devices.

References

1. I. Žutić, J. Fabian and S. Das Sarma, Rev. Mod. Phys. **76** (2), 323 (2004).
2. J. Fabian, A. Matos-Abiague, C. Ertler, P. Stano and I. Žutić, in *Acta Physica Slovaca. Reviews and Tutorials* (2007), Vol. 57, pp. 565.
3. S. P. Dash, S. Sharma, R. S. Patel, M. P. de Jong and R. Jansen, Nature **462** (7272), 491 (2009).
4. A. Fert and H. Jaffrès, Phys. Rev. B **64** (18), 184420 (2001).
5. G. Schmidt, D. Ferrand, L. W. Molenkamp, A. T. Filip and B. J. van Wees, Phys. Rev. B **62** (8), R4790 (2000).
6. W. J. M. Naber, S. Faez and W. G. v. d. Wiel, J. Phys. D: Appl. Phys. **40**, R205 (2007).
7. V. Dediu, L. E. Hueso, I. Bergenti and C. Taliani, Nature Mater. **8**, 707 (2009).
8. V. Dediu, M. Murgia, F. C. Matacotta, C. Taliani and S. Barbanera, Solid State Commun. **122** (3–4), 181 (2002).
9. C. B. Harris, R. L. Schlupp and H. Schuch, Phys. Rev. Lett. **30**, 1019 (1973).
10. V. I. Krinichnyi, S. D. Chemerisov and Y. S. Lebedev, Phys. Rev. B **55**, 16233 (1997).
11. Z. H. Xiong, D. Wu, Z. V. Vardeny and J. Shi, Nature **427**, 821 (2004).
12. M. Gobbi, F. Golmar, R. Llopis, F. Casanova and L. E. Hueso, Adv. Mater. **23** (14), 1609 (2011).
13. R. Lin, F. J. Wang, M. Wohlgenannt, C. Y. He, X. F. Zhai and Y. Suzuki, Synth. Met. **161** (7-8), 553 (2011).
14. T. D. Nguyen, G. Hukic-Markosian, F. Wang, L. Wojcik, X.-G. Li, E. Ehrenfreund and Z. V. Vardeny, Synth. Met. **161** (7–8), 598 (2011).
15. V. Dediu, L. E. Hueso, I. Bergenti, A. Riminucci, F. Borgatti, P. Graziosi, C. Newby, F. Casoli, M. P. de Jong, C. Taliani and Y. Zhan, Phys. Rev. B **78** (11), 115203 (2008).
16. C. Barraud, P. Seneor, R. Mattana, S. Fusil, K. Bouzehouane, C. Deranlot, P. Graziosi, L. Hueso, I. Bergenti, V. Dediu, F. Petroff and A. Fert, Nat Phys **6** (8), 615 (2010).
17. A. J. Drew, J. Hoppler, L. Schulz, F. L. Pratt, P. Desai, P. Shakya, T. Kreouzis, W. P. Gillin, A. Suter, N. A. Morley, V. K. Malik, A. Dubroka, K. W. Kim, H. Bouyanfif, F. Bourqui, C. Bernhard, R. Scheuermann, G. J. Nieuwenhuys, T. Prokscha and E. Morenzoni, Nat. Mater. **8**, 109 (2009).
18. R. Lin, F. Wang, J. Rybicki, M. Wohlgenannt and K. A. Hutchinson, Phys. Rev. B **81** (19), 195214 (2010).
19. J. J. H. M. Schoonus, P. G. E. Lumens, W. Wagemans, J. T. Kohlhepp, P. A. Bobbert, H. J. M. Swagten and B. Koopmans, Phys. Rev. Lett. **103** (14), 146601 (2009).

20. J. S. Jiang, J. E. Pearson and S. D. Bader, Phys. Rev. B **77** (3), 035303 (2008).
21. P. A. Bobbert, T. D. Nguyen, F. W. A. van Oost, B. Koopmans and M. Wohlgenannt, Phys. Rev. Lett. **99** (21), 216801 (2007).
22. D. Zhang, J. R. Norris, P. J. Krusic, E. Wasserman, C. C. Chen and C. M. Lieber, J. Phys. Chem. **97** (22), 5886 (1993).
23. T. D. Nguyen, Y. Sheng, M. Wohlgenannt and T. D. Anthopoulos, Synth. Met. **157** (22–23), 930 (2007).
24. B. Hartenstein and H. Bässler, J Non-Cryst Solids **190** (1–2), 112 (1995).
25. R. Coehoorn, W. F. Pasveer, P. A. Bobbert and M. A. J. Michels, Phys. Rev. B **72**, 155206 (2005).
26. P. Rudolf, M. S. Golden and P. A. Bruhwiler, J. Electron Spectrosc. Relat. Phenom. **100**, 409 (1999).
27. S. Braun, W. R. Salaneck and M. Fahlman, Adv. Mater. **21** (14-15), 1450 (2009).
28. R. W. Lof, M. A. van Veenendaal, B. Koopmans, H. T. Jonkman and G. A. Sawatzky, Phys. Rev. Lett. **68** (26), 3924 (1992).
29. W. Osikowicz, M. P. de Jong and W. R. Salaneck, Adv. Mater. **19**, 4213 (2007).
30. M. Popinciuc, H. T. Jonkman and B. J. van Wees, J. Appl. Phys. **101** (9), 093701 (2007).
31. B. C. Min, Ph. D thesis, University of Twente, 2007.
32. T. S. Santos, J. S. Lee, P. Migdal, I. C. Lekshmi, B. Satpati and J. S. Moodera, Phys. Rev. Lett. **98**, 016601 (2007).
33. B. C. Min, K. Motohashi, J. C. Lodder and R. Jansen, Nature Mater. **5**, 817 (2006).
34. A. Miller and E. Abrahams, Phys. Rev. **120** (3), 745 (1960).
35. S. Bandyopadhyay, Phys. Rev. B **81** (15), 153202 (2010).
36. Z. G. Yu, Phys. Rev. Lett. **106** (10), 106602 (2011).
37. S. Demokritov, E. Tsymbal, P. Grünberg, W. Zinn and I. K. Schuller, Phys. Rev. B **49** (1), 720 (1994).
38. S. P. Dash, S. Sharma, J. C. Le Breton, J. Peiro, H. Jaffrès, J. M. George, A. Lemaître and R. Jansen, Phys. Rev. B **84** (5), 054410 (2011).
39. J. C. S. Kools, W. Kula, D. Mauri and T. Lin, J. Appl.Phys **85** (8), 4466 (1999).
40. B. D. Schrag, A. Anguelouch, S. Ingvarsson, G. Xiao, Y. Lu, P. L. Trouilloud, A. Gupta, R. A. Wanner, W. J. Gallagher, P. M. Rice, S. S. P. Parkin and 77, Appl. Phys. Lett. **77**, 2373 (2000).
41. D. S. Bethune, G. Meijer, W. C. Tang, H. J. Rosen, W. G. Golden, H. Seki, C. A. Brown and M. S. de Vries, Chem. Phys. Lett. **179** (1–2), 181 (1991).
42. J. Laflamme Janssen, M. Côté, S. G. Louie and M. L. Cohen, Phys. Rev. B **81** (7), 073106 (2010).

CHAPTER 4

Hybridization-induced oscillatory magnetic polarization of C_{60}-orbitals at the C_{60}/Fe(001) interface

We have studied the electronic and magnetic properties of the interface between C_{60} molecules and a Fe(001) surface. X-ray absorption spectroscopy and x-ray magnetic circular dichroism studies of C_{60} monolayers on Fe(001) surfaces show that hybridization between the frontier orbitals of C_{60} and continuum states of Fe leads to a significant magnetic polarization of C_{60} π^*-derived orbitals. The magnitude and also the sign of this polarization were found to depend markedly on the excitation energy. These observations underline the importance of tailoring the interfacial spin polarization at the Fermi level of ferromagnet/organic semiconductor interfaces for applications in organic spintronics.

This chapter has been published, in slightly modified form, as T.L.A. Tran, P.K.J. Wong, M.P. de Jong, W. G. van der Wiel, Y. Q. Zhan, and M. Fahlman, Appl. Phys. Lett. 98 (2011) 222505.

4.1 Introduction

The main attractive attributes of organic and, more generally, carbon-based materials for spintronics are the weak spin orbit coupling and hyperfine interactions, such that the spin polarization of the carriers can potentially be maintained for a long time.[1-3] Promising results involving spin-dependent electronic transport in devices comprising organic, carbon-based materials have been obtained for vertical, current-perpendicular-to-plane (CPP) geometries (notable exceptions being graphene[4] and carbon nanotubes[5]) for which clear spin-valve signals have been observed in lateral devices). In such vertical devices, organic semiconductors are used either as a tunnel barrier[6, 7] or charge/spin transport spacer[7-9] placed between two ferromagnetic electrodes. Although spin-valve behavior has been consistently observed in devices encompassing several different organic semiconductors, *e.g.* tris(8-hydroxy-quinolinato)aluminium (Alq_3),[7, 8] pentacene,[10] and rubrene[11] and C_{60},[12-14] the microscopic mechanisms governing the magnetotransport behavior remain poorly understood, in part due to the often ill-defined hybrid interfaces in the devices. The understanding of magnetotransport behavior in such organic spintronic devices may be improved upon exploiting the electronic structure and magnetic properties of *well-defined* interfaces between ferromagnetic electrodes and organic semiconductors.[7, 15, 16] Among these organic materials, C_{60} molecules are especially interesting for organic spintronics because of the absence of hydrogen nuclei and the associated spin-dephasing mechanism by hyperfine coupling[17] (the 99% predominant ^{12}C isotopes have zero nuclear spin).

In this chapter , we investigated the electronic and magnetic structure of the C_{60}/Fe (001) interface using electron spectroscopic techniques. Photoemission spectroscopy (PES), and X-ray adsorption spectroscopy (XAS) are used to study the interfacial electronic structure and hybridization effects e.g. charge transfer and chemisorption of C_{60} molecules on the Fe(001) surface. By using x-ray magnetic circular dichroism (XMCD, we could determine the magnetic polarization, of C_{60} orbitals at the C_{60}/Fe(001) interface and the effect of hybridization between Fe 3d states and C_{60} orbitals on the spin-dependent electronic structure of the Fe surface atoms.

4.2 Experiments

The experiments have been done at beam line D1011 of the MAX-Laboratory in Lund, Sweden (base pressure 10^{-10} mbar). MgO(001) substrates were annealed (450 ^{o}C, 1 hour) to obtain clean and restructured surfaces,[18, 19] on top of which a Fe film of several nm thick was grown at 150 ^{o}C, using a mini e-beam evaporator. The epitaxial growth of Fe(001) is verified with low energy electron diffraction (LEED, see Fig. 1(a)). The LEED pattern in Fig. 1(a) of Fe(001) on MgO(001) reveals a well-ordered (1×1) spot pattern, without any additional distinct features of *e.g.* a granular structure, indicating a high degree of structural order in the Fe film due to a good lattice match of MgO (a=4.213Å) and Fe (a=2.866Å) upon a 45^{o} in-plane rotation of the Fe layer.[20] The reader is referred to Chapter 5 of this thesis, or Ref. [15], for more details concerning the growth of epitaxial bcc-Fe (001) on MgO(001) substrates, where the films were grown under similar conditions as described here and characterized by x-ray diffraction (XRD) and scanning tunneling microscopy (STM). C_{60} molecules were deposited *in-situ* onto Fe(001) at room temperature by thermal evaporation from a simple custom-built Knudsen-cell. The thickness of C_{60} was controlled by the deposition time while the effusion cell temperature was kept constant. We examine the electronic properties for three different C_{60} layers on Fe(001), hereafter referred as sample A, B, and C: (A) an as-grown ultrathin film with a coverage of approximately 1 ML, (B) an as-grown multilayer exhibiting bulk-like properties, and (C) a monolayer obtained by annealing a multilayer sample at 280 ^{o}C for one minute, such that weakly bound overlayers are desorbed. These different cases are depicted in Fig. 1(b).

The electronic- and magnetic structure of Fe and C_{60} on Fe films were analyzed by photoemission spectroscopy (PES), x-ray absorption spectroscopy (XAS) and x-ray magnetic circular dichroism (XMCD). The XAS and XMCD spectra were measured at room temperature in the total electron yield (TEY) mode. The angle of incidence of the photon beam was set to 70^{o} relative to the sample normal. XMCD spectra were recorded by reversing the helicity of the circularly polarized photons with respect to the (in plane) magnetization (in remanence, after applying a magnetic field pulse of 250 Oe) of the Fe layers. All the XAS and XMCD measurements were normalized to the incident photon flux using the TEY

of a gold grid, onto which a fresh layer of gold was deposited prior to the measurements.

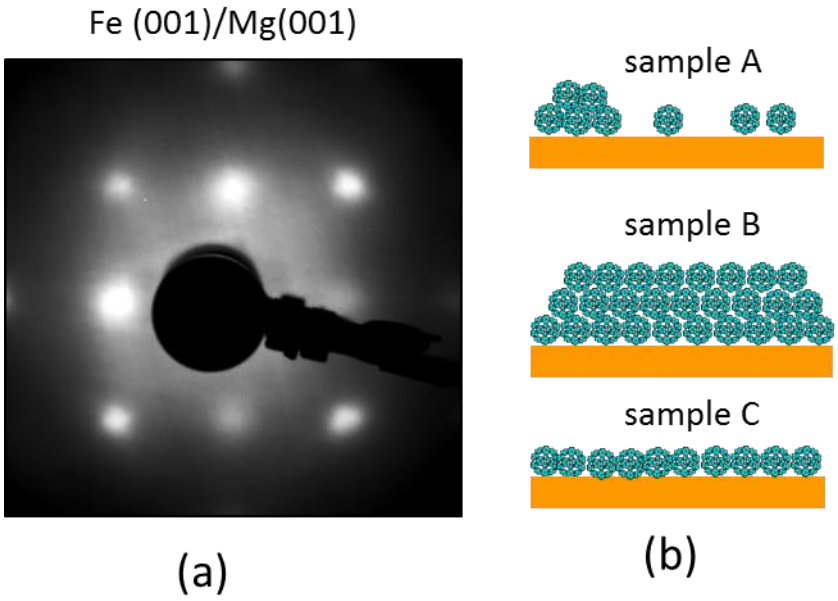

Figure 4.1 (a) LEED pattern of an epitaxial bcc-Fe (001) film on MgO(001); (b) sketch of C_{60} molecules on the Fe surface for samples A, B, and C.

4.3 Results and discussion

4.3.1 Electronic structure of C_{60} on Fe(001)

In this section, we describe the characterization of the electronic structure of C_{60} on Fe, for samples A, B, and C, by means of PES and C K-edge XAS measurements. For sample A, obtained by depositing molecules at room temperature, the coverage of C_{60} is estimated to be ~1 ML, by comparing the intensity of the C K-edge XAS features (signal to background ratio) to that of sample C, where only a chemisorbed monolayer is retained on the surface after weakly bound overlayers have been annealed off. It is noted here that at room

temperature, layer-by-layer growth is not expected *a priori*. Instead, it is possible that C_{60} forms islands, which will be discussed in some detail below. The C_{60} multilayer, sample B, which was also deposited at room temperature, exhibited bulk-like electronic structure similar to that of other thin C_{60} films reported in the literature [see e.g. Ref 22].

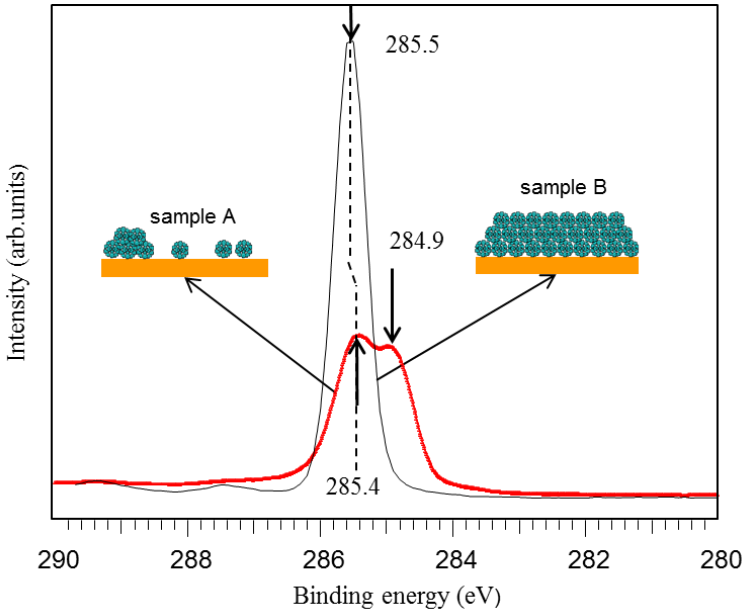

Figure 4.2 C(1s) photoemission spectra (hν=400 eV) of sample A (red) and B (black).

Figure 4.2 shows the PES C(1s) (hν=400 eV) spectra of sample A and sample B. The C(1s) spectrum of the multilayer (sample B) contains only one component (one sharp peak at a binding energy of 285.5 eV), as expected for bulk C_{60}, while that of sample A contains two peaks, at 284.9 and 285.4 eV, respectively. In general, core level binding energy shifts are caused by two effects: initial state and final state effects. The initial state effect results from a different chemical environment, which influences the electron density in the carbon atoms, such that the C(1s) energy level shifts up or down; chemisorption will generally cause such a shift. Final state effects, on the other hand, are due to screening of the core hole

created by photoemission by other electrons. Since a metal is highly polarizable, the screening is very effective and the binding engery will be generally lower due to this effect for molecules adsorbed on metals. Therefore, the peak at 284.9 eV (that is 0.6 eV smaller than the binding engery of the C(1s) line of the C_{60} multilayer) is assigned to C_{60} molecules that are adsorbed on Fe surface. The screening by the metal substrate will be reduced for the second layer (and even more so for further overlayers) of C_{60} molecules, such that the binding engery shift may be expected to be smaller. Initial state effects due to chemisorption, i.e. hybridization with Fe bands, is of course also absent for these molecules. Accordingly, the peak at 285.4 eV (exhibiting a small energy shift of 0.1 eV compared to the C(1s) line of the C_{60} multilayer) is assigned to C_{60} molecules sitting on top of other molecules. The C(1s) spectrum of sample A, exhibiting two peaks, is thus consistent with an interpretation involving contributions from (i) C_{60} molecules that are chemically bonded to the Fe substrate, and (ii) additional contributions from C_{60} overlayers. The approximately equal contributions of the two peaks to the C(1s) spectrum may erroneously suggest that these different species of molecules are present in equal amounts, however it has to be taken into account that the signal from the first layer of molecules on Fe is suppressed if other molecules sit on top.

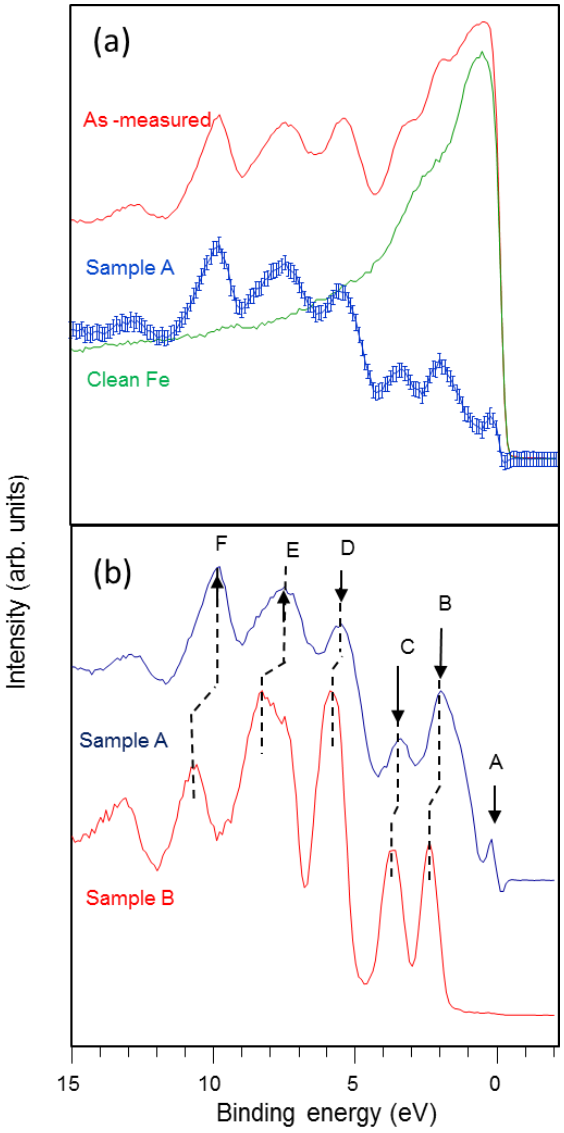

Figure 4.3 (a) Valence band PES spectra, recorded with a photon energy of 110 eV, of sample A and a clean Fe (001) film. A spectrum of sample A after (weighted) subtraction of the Fe contribution, taken as the difference between the as- measured spectra and a weighted spectrum of clean Fe, is also shown; (b) Comparison of the valence band PES spectra of sample A (from (a)) and B.

Figure 4.3(a) shows a valence band PES spectrum of sample A, as well as a clean Fe (001) spectrum, recorded at a photon energy of 110 eV. The difference spectrum was obtained by subtraction of a weighted contribution of the clean Fe surface. Figure 4.3 (b) shows the so-obtained valence band spectrum of the C_{60} adsorbates in sample A, and the C_{60} multilayer (sample B) for comparison. It is clear that the C_{60} molecular orbital structure is modified upon adsorption on the Fe surface. The peaks due to different (sets of) molecular orbitals, labeled as B, C, D, E and F in the graph broaden and shift as compared to their counterparts of the C_{60} multilayer. As can be seen in the Fig. 4.3(b), not all peak shifts are the same. Peaks B and C shift by about 0.4 eV, while peaks D, E and F peaks shift by approximately 0.7 eV. Such differential peak shifts are consistent with chemisorption, where hybridization between molecular orbitals and metal continuum states affects different orbitals in different ways. The C(1s) spectra clearly indicated the presence of different species, i.e. C_{60} molecules bonded to the Fe surface as well as molecules in overlayers, for which hybridization with Fe states does not occur. The valence band spectra do not allow for such a clear distinction. In part, this may be related to the reduced screening of the more delocalized valence band holes (as compared to C(1s) core holes) by the metallic substrate, producing a smaller binding energy shift. A small but significant peak near the Fermi level is also revealed after subtracting the Fe contribution from the valence band spectrum. This peaks is assigned to the partially filled lowest unoccupied molecular orbital (LUMO), (labeled as A in the graph) where the partial filling is due to charge transfer from the Fe substrate to the C_{60} molecules. This observation is similar to the previously reported case of C_{60} adsorbed on noble metals.[21]

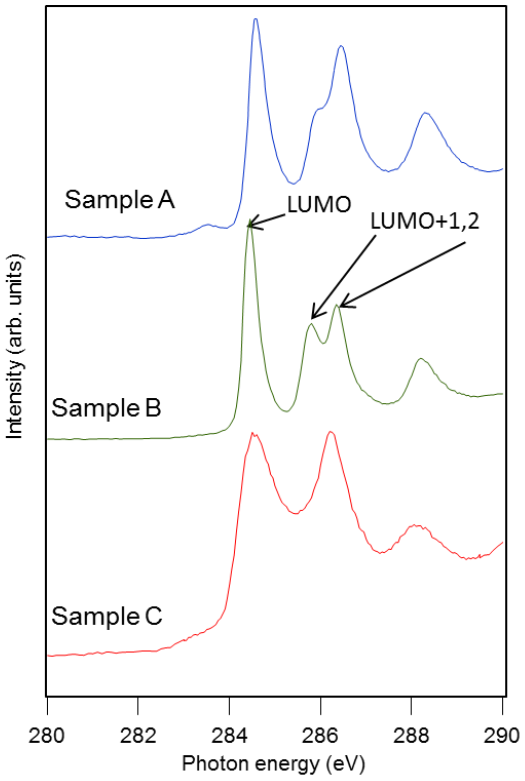

Figure 4.4 C K-edge XAS spectra of samples A, B, and C. The peaks represent various core-excited states derived from virtual (i.e. unoccupied) molecular orbitals. The first peak, at 284.45 eV excitation energy, is related to the lowest unoccupied molecular orbital (LUMO). Consequently the second peak (for sample B) at 285.80 eV, and the third peak at 286.35 eV are related to the LUMO+1 and LUMO+2 orbitals, respectively.

Figure 4.4 shows the C K-edge XAS spectra of samples A, B, and C. The peaks in the XAS spectra represent various core-excited states derived from virtual molecular orbitals. The C_{60} multilayer XAS spectrum (sample B) reflects the corresponding spectrum of bulk C_{60}.[22] The first peak at 284.45 eV excitation energy is related to the lowest unoccupied molecular orbital (LUMO). In the core-excited state, the three-fold degeneracy of the LUMO is lifted by the presence of the core-hole, such that the $5t_{1u}$ level (in icosahedral, I_h, symmetry) splits into three

levels with slightly different energy eigenvalues. However, as has been shown by theoretical modeling,[17] only one of these states contributes significantly to the C K-edge spectrum due to the large difference in oscillator strengths. Essentially the same holds for the LUMO+1 and LUMO+2 orbitals, which give rise to peaks at 285.80 and 286.35 eV photon energy, respectively.

The spectrum of sample C is dominated by two considerably broadened peaks compared multilayer spectrum, indicating orbital hybridization at the interface. Similar hybridization-induced spectral changes, including the merging of the LUMO+1 and LUMO+2 resonances into a single peak and a shift to higher energy of the LUMO peak, have been observed for C_{60} adsorbed on *f.e.* Al and Au.[22] The peak broadening and LUMO-shift, from 284.45 eV (multilayer) to 284.55 eV (ML), which have previously been found to scale with the bond strength,[22] indicate strong interfacial bonding between C_{60} and Fe. We also note a small but clearly visible shoulder in the C_{60} sub-ML and ML XAS spectra at about 284.5 eV, which we attribute to (partial) occupation of the LUMO due to electron transfer from Fe to C_{60}, in agreement with valence PES spectra in Fig. 4.3 and in analogy with previous reports for C_{60} on Cu(111).[19]

The XAS spectral features of sample A resemble a combination of those of samples B and C. The LUMO+1 and LUMO+2 peaks are not completely merged into one peak, but a minor peak remains at the LUMO+1 energy position. These features are consistent with the presence of chemisorbed species as well as molecules residing in overlayers, which is in agreement with the C1s PES spectra in Fig. 4.2.

4.3.2 The C_{60}-Fe interaction: the hybridization effect at the C_{60}/Fe(001) interface.

Recently published theoretical and experimental results[11, 14, 23, 24] show that the hybridization between the orbitals of organic molecules (or graphene[6]) and ferromagnetic metal (3*d*) valence band states can lead to sizeable interfacial magnetic moments and spin polarization of π-conjugated states in carbon-based systems. For graphene on Ni(111),[6] a particularly strong C K-edge XMCD signal of about 5% of the XAS intensity has been observed, reflecting the significant degree of mixing between C p_z and Ni 3*d* derived states at the interface.[22, 25] To investigate the magnetic properties of the interface between the C_{60} and Fe, we

analyze the XMCD spectra of both the Fe $L_{2,3}$-edge and C K-edge. Here we focus on the XMCD spectra of a chemisorbed C_{60} MLC_{60} on Fe(001), obtained by desorption of weakly bound molecules by annealing. Such a system is characterized by strong hybridization effects as discussed section 4.4.1. The Fe $L_{2,3}$ -edge XMCD spectra show strong dichroism, similar to that of clean Fe (001) (Fig. 4.5 a). From Fig. 4.5b, we can also observe a significant dichroic signal (of about 3% of the XAS intensity) at the C K-edge of the ML C_{60}/Fe(001) system. This strong XMCD signal indicates a sizeable magnetic moment on the C_{60}–Fe hybridized orbitals. K-edge magnetic dichroism, involving *s* to *p* dipole transitions, is attributed to the orbital moment in the final state (see Ref. [26] and references therein), which in turn depends on spin-orbit coupling. Therefore, even though the C K-edge XMCD probes orbital polarization, it is intimately connected to the spin polarization of the hybrid states. Depending on the excitation energy, an inversion of the polarization of the C_{60} derived π^* states with respect to that of the Fe layer is evident from the change of sign of the XMCD signal across the $C(1s)\rightarrow\pi^*$ resonance. In particular, the LUMO-related transition has an XMCD signal that is opposite to that of the Fe L_3-edge (Fig. 4.5a), corresponding to a magnetic polarization of the LUMO-derived orbital that is also opposite to that of the Fe surface.

Our results might be interpreted in terms of an oscillatory interfacial spin polarization, induced by the hybridization between carbon p_z orbitals and Fe 3*d* majority and minority bands. Such a scenario is similar to the recently published theoretical and experimental (spin-polarized scanning tunneling microscopy) results on the complex, energy-dependent spin polarization of aromatic molecules on Fe/W(110).[23] For these systems, *viz.* benzene (C_6H_6), cyclopentadienyl radicals (C_5H_5), and cyclo-octatetraene (C_8H_8) on 2 ML Fe/W(110) substrates, first-principles density functional theory calculations show that the hybridization of out-of-plane π- and π^*-orbitals with metal *d*-states leads to an oscillatory behavior of the spin polarization versus binding energy of electronic states on the molecules with respect to that of the metal substrate bands. Our experimental observations tentatively support a similar picture for C_{60} on Fe(001), and underline the crucial role played by the hybridization effects between different molecular π^* (and π) orbitals and metal 3*d* surface bands in determining the magnetic properties of the interfaces. These effects may be exploited to tune the interfacial spin polarization, and thereby influence spin-polarized charge carrier injection, at properly

engineered, structurally and electronically well-defined organic/ferromagnetic metal interface.

It is an interesting question whether the hybridization of C_{60} orbitals with Fe 3*d* states significantly affects the spin-dependent electronic structure of the Fe surface atoms. If so, one would expect to observe a change in the orbital and/or spin moments in the Fe L-edge XMCD spectra upon adsorption of C_{60} onto Fe. However, such effects are difficult to observe in samples comprising several nm thick Fe films, due to the significant contribution of bulk Fe atoms to the XAS yield (even for partial electron yield measurements the probing depth is several nm), obscuring effects due to bonding between C_{60} and the Fe surface. Accordingly, additional samples incorporating a low coverage of Fe (significantly less than 1 ML) on Co(several nm)/MgO(001) were prepared, such that the majority of Fe atoms (if not all) will reside at the surface. Since the magnetic moments of the Fe atoms are aligned with the magnetization of the Co layers, such samples can be easily magnetized in-plane and characterized in remanence.

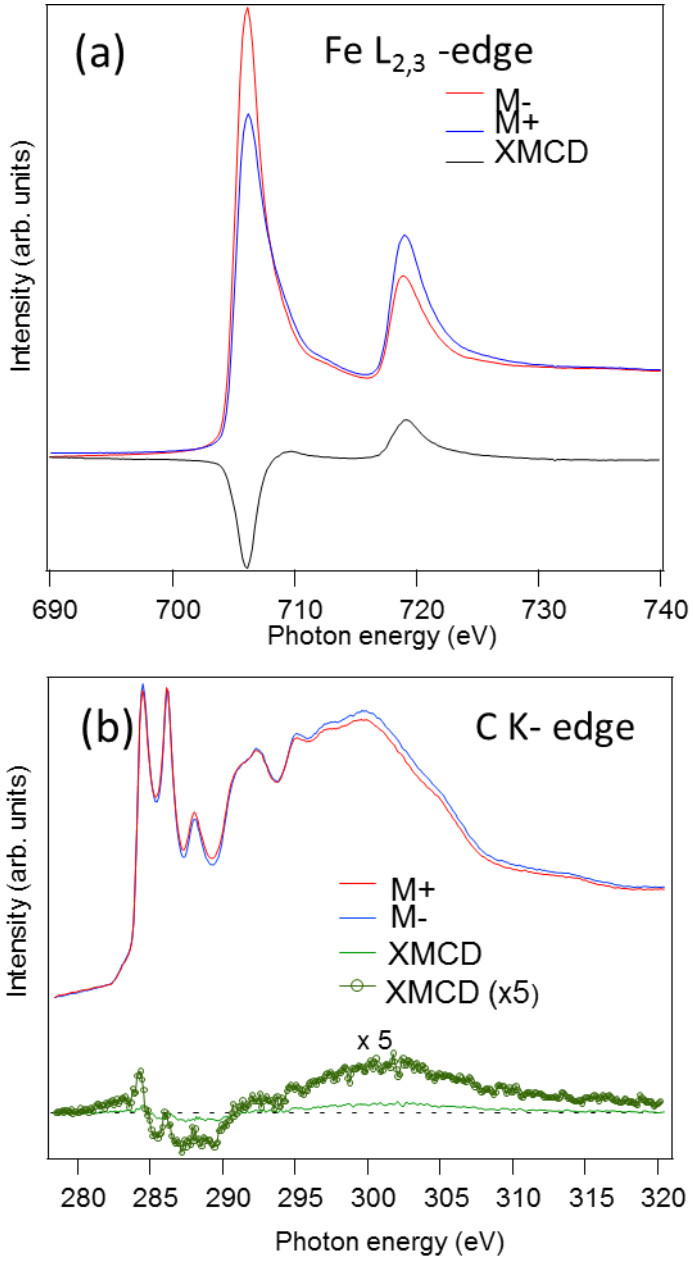

Figure 4.5 Fe L-edge (a) and C K- edge (b) XAS and XMCD spectra of a ML C_{60}/Fe(001). The XMCD spectra (green) were obtained by taking the difference between the XAS data recorded with parallel and antiparallel alignment of the magnetization and photon helicity.

Figure 4.6 shows the corresponding Fe L-edge XMCD spectra, of the same sample before and after the deposition of a C_{60} overlayer. The spectra are normalized to the L_3-peak height of the XAS sum spectra for parallel and antiparallel alignment between the magnetization and photon helicity. After adsorbing C_{60}, the Fe L_3-edge XMCD signal is somewhat suppressed, while the L_2 edge remains unaffected (within the experimental error), indicating a reduction of, in particular, the orbital magnetic moments on the Fe atoms due to hybridization between Fe- and C_{60} electronic states. Applying the XMCD sum rules[27] to the integrated XMCD spectra shows a slight reduction of the spin magnetic moment (of about 1-2 %), consistent with partial electron transfer to the C_{60} molecule. The orbital moment, which is especially sensitive to hybridization effects, is reduced by roughly a factor of three. It should be pointed out, however, that this experiment does not provide direct quantitative information on the effects of C_{60} adsorption on the spin and orbital magnetic moments of an actual Fe(001) surface. However, it serves to illustrate the qualitative effects of chemical bonding between C_{60} and Fe on the Fe magnetic moments, and is in agreement with our observations of a strong, hybridization-induced XMCD effect at the C K-edge of ML C_{60}/Fe(001) samples. The results are also in qualitative agreement with the bonding-induced modification of the spin polarized Fe 3*d*-derived interfacial electronic structure of aromatic molecules on Fe/W(110) reported in Ref. 28, and the calculated reduced magnetic moments of surface Ni atoms at graphene/Ni(111) interfaces.[22]

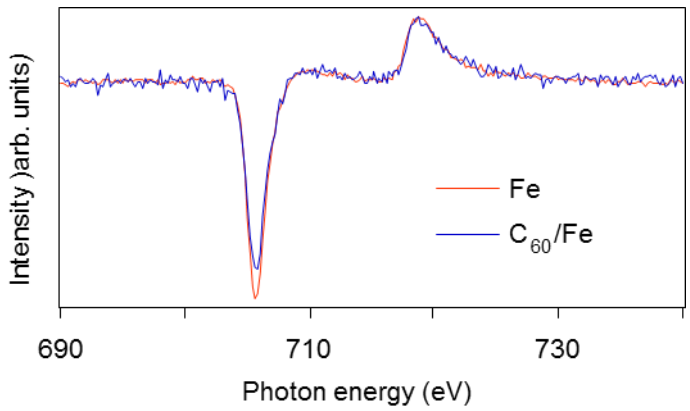

Figure 4.6 Fe L-edge XMCD spectra of sub-monolayer Fe on Co/MgO(001) before and after adsorbing C_{60}.

4.4 Conclusions

In conclusion, the C K-edge XAS spectra show evidence of significant hybridization between C_{60} orbitals and Fe continuum states, and mixing between C_{60} $\pi(\pi^*)$ orbitals and Fe 3*d* wave functions leads to a distinct, oscillatory magnetic moment of C_{60}-derived interfacial electronic states due to spin-orbit coupling in the hybridized final state, as is evident from C K-edge XMCD spectra. The oscillatory nature of the polarization of these states close to E_F is important in the light of spin-polarized charge injection across the interface. Gaining control of the interfacial spin polarization at well-defined hybrid interfaces is an essential ingredient for systematically engineering the performance of future organic and molecular spintronic devices.

References

1. J. H. Shim, K. V. Raman, Y. J. Park, T. S. Santos, G. X. Miao, B. Satpati and J. S. Moodera, Phys. Rev. Lett. **100** (22), 226603 (2008).
2. M. Takahashi and J.-I. Igarashi, Phys. Rev. B **67**, 245104 (2003).
3. T. S. Santos, J. S. Lee, P. Migdal, I. C. Lekshmi, B. Satpati and J. S. Moodera, Phys. Rev. Lett. **98**, 016601 (2007).
4. N. Tombros, C. Jozsa, M. Popinciuc, H. T. Jonkman and B. J. v. Wees, Nature **448**, 571 (2007).
5. S. Steil, N. Grossmann, M. Laux, A. Ruffing, D. Steil, M. Wiesenmayer, S. Mathias, O. L. A. Monti, M. Cinchetti and M. Aeschlimann, Nat. Phys. **9** (4), 242 (2013).
6. M. Weser, Y. Rehder, K. Horn, M. Sicot, M. Fonin and A. B. Preobrajenski, Appl. Phys. Lett. **96**, 012504 (2010).
7. C. Martinez-Boubeta, J. L. Costa-Kramer and A. Cebollada, J. Phys: Condens. Matter **15**, R1123 (2003).
8. Z. H. Xiong, D. Wu, Z. V. Vardeny and J. Shi, Nature **427**, 821 (2004).
9. T. D. Nguyen, G. Hukic-Markosian, F. Wang, L. Wojcik, X.-G. Li, E. Ehrenfreund and Z. V. Vardeny, Nat. Mater. **9** (4), 345 (2010).
10. S. Parkin, X. Jiang, C. Kaiser, A. Panchula, K. Roche and M. Samant, Proc. IEEE **91** (5), 661 (2003).

11. Y. Zhan, E. Holmström, R. Lizárraga, O. Eriksson, X. LiU, E. Carlegrim, S. Stafström and M. Fahlman, Adv. Mater. **22**, 1626 (2010).
12. T. L. A. Tran, D. Cakir, P. K. Wong, A. B. Preobrajenski, G. Brocks, W. G. van der Wiel and M. P. de Jong, ACS Appl. Mater. Interfaces **5** (3), 837 (2013).
13. M. P. Seah and W. A. Dench, Surf. Interface Anal. **1** (1), 2 (1979).
14. T. L. A. Tran, T. Q. Le, J. G. M. Sanderink, W. G. van der Wiel and M. P. de Jong, Adv. Funct. Mater. **22** (6), 1180 (2012).
15. P. K. J. Wong, T. L. A. Tran, P. Brinks, W. G. van der Wiel, M. Huijben and M. P. de Jong, Organ. Electron. **14** (2), 451 (2013).
16. G. Binasch, P. Grünberg, F. Saurenbach and W. Zinn, Phys. Rev. B **39** (7), 4828 (1989).
17. B. Wästberg, S. Lunell, C. Enkvist, P. A. Brühwiler, A. J. Maxwell and N. Mårtensson, Phys. Rev. B **50** (17), 13031 (1994).
18. B. Wassermann, Philos. Mag. **83**, 1929 (2003).
19. K.-D. Tsuei, J.-Y. Yuh, C.-T. Tzeng, R.-Y. Chu, S.-C. Chung and K.-L. Tsang, Phys. Rev. B **56** (23), 15412 (1997).
20. T. Urano and T. Kanaji, J. Phys. Soc. Jpn. **57**, 3043 (1988).
21. T. Shimada, H. Nogawa, T. Noguchi, Y. Furubayashi, Y. Yamamoto, Y. Hirose, T. Hitosugi and T. Hasegawa, Jpn. J. Appl. Phys. **47** (2), 1184 (2008).
22. A. J. Maxwell, P. A. Brühwiler, D. Arvanitis, J. Hasselström, M. K.-J. Johansson and N. Mårtensson, Phys. Rev. B **57** (12), 7312 (1998).
23. D. Liu, Y. Hu, H. Guo and X. F. Han, Phys. Rev. B **78**, 193307 (2008).
24. X. Sun, A. Pratt and Y. Yamauchi, J. Phys. D: Appl. Phys. **43**, 385002 (2010).
25. B. Dieny, V. S. Speriosu, S. S. P. Parkin, B. A. Gurney, D. R. Wilhoit and D. Mauri, Phys. Rev. B **43** (1), 1297 (1991).
26. J. S. Moodera, L. R. Kinder, T. M. Wong and R. Meservey, Phys. Rev. Lett. **74** (16), 3273 (1995).
27. A. J. Maxwell, P. A. Brühwiler, D. Arvanitis, J. Hasselström and N. Mårtensson, Chem. Phys. Lett. **260** (1–2), 71 (1996).

CHAPTER 5

Magnetic properties of bcc- Fe(001)/C_{60} interfaces for organic spintronics

The magnetic structure of the interfaces between organic semiconductors and ferromagnetic contacts plays a key role in the spin injection and extraction processes in organic spintronic devices. We present a combined computational (density functional theory) and experimental (x-ray magnetic circular dichroism) study on the magnetic properties of interfaces between bcc-Fe(001) and C_{60} molecules. C_{60} is an interesting candidate for application in organic spintronics due to the absence of hydrogen atoms and the associated hyperfine fields. Adsorption of C_{60} on Fe(001) reduces the magnetic moments on the top Fe layers by ∼6%, while inducing an anti-parrallel magnetic moment of $\sim -0.2\ \mu_B$ on C_{60}. Adsorption of C_{60} on a model ferromagnetic substrate consisting of three Fe monolayers on W(001) leads to a different structure, but to very similar interface magnetic properties.

This chapter has been published, in slightly modified form, as T.L.A. Tran, D. Çakır, P.K.J. Wong, A.B. Preobrajenski, G. Brocks, W.G. van der Wiel, and M.P. de Jong, ACS Appl. Mater. Interfaces 5, 837 (2013)

5.1 Introduction

Organic semiconductor spintronics, which focuses on information processing via charge carrier spins in carbon-based, molecular semiconductors, is a new and exciting field of nanoelectronics.[1, 2] Organic semiconductors (OSCs) are suitable hosts for spin polarized carriers, because the spin- orbit coupling and hyperfine interactions in these materials are relatively weak. This leads to long spin relaxation- and dephasing times (> 1 μs) compared to those attainable in inorganic semiconductors, which in principle allows for robust spin operations and read-out.[2, 3] Large magnetoresistance (MR) effects have been observed in vertical organic spin valves, where OSCs are sandwiched between two ferromagnetic (FM) electrodes, and are used either as a tunnel barrier,[4-6] or as charge/spin transport medium.[5, 7] Substantial MR at room temperature has been reported in spin valves based on tris(8-hydroxy-quinolinato) aluminium (Alq_3) [4, 5, 7-9] and on C_{60}.[10-12] Phenomenological models for the observed magneto-transport effects have been developed,[5, 9] yet the microscopic physical mechanisms remain poorly understood. It has become clear that the electronic structure, in particular the spin polarization, of the hybrid interfaces between the OSC and the ferromagnetic metal electrodes, plays a key role in spin injection and spin extraction. [5] Consequently, an important obstacle in developing a microscopic understanding of these processes is formed by the challenge of fabricating devices with electronically, magnetically and structurally well-defined hybrid interfaces. Incorporating such well-defined interfaces into organic spintronic devices would allow for a direct comparison with theoretical modeling, and is therefore of great importance to advance the understanding of the operation mechanisms of these devices. Furthermore, systematic studies of various relevant OSC/FM interfaces are required to exploit the full potential of *tailoring* the interfacial spin polarization via hybridization effects, an approach that has been coined "spinterface science".[13] Such spin dependent hybridization can give rise to large magnetoresistance effects, as has been shown recently by scanning tunneling microscopy experiments.[14]

Here, we present a combined computational and experimental study on the magnetic properties of interfaces between bcc-Fe(001) and C_{60} for organic spintronic devices. Fullerenes such as C_{60} are particularly interesting candidates for application in organic spintronic devices, due to the absence of hydrogen atoms which give rise to spin dephasing via hyperfine interactions. C_{60} layers can be

grown in a controlled way on a bcc-Fe(001) substrate (see chapter 3 and Ref. [15] for more details). An important issue that we wish to address is the impact of the C_{60}/Fe interaction on the spin polarization at the interface. Similar to the case of C_{60} on Cr(001),[16] a significant chemical interaction is expected, which would lead to spin polarized hybrid states. We use first-principles density functional theory (DFT) calculations to extract the magnetizations of the Fe surface, and of the C_{60}/Fe interface. Carbon *K-edge* x-ray absorption spectroscopy (XAS) and x-ray magnetic circular dichroism (XMCD) measurements of C_{60} layers on Fe(001) indicate a sizeable spin polarization of the unoccupied C_{60} states just above the Fermi level, induced by the interaction with the Fe substrate.[15] A similar Fe $L_{2,3}$ edge XAS/XMCD analysis of the interaction induced changes in the spin polarization of the Fe surface atoms is hampered by the significant contribution of the Fe bulk substrate to the XAS yield. To alleviate this problem we use here an ultrathin Fe layer substrate, consisting of three Fe monolayers (ML) deposited onto a W(001) surface. In spite of the large experimental lattice mismatch of 10.4% between Fe and W, Fe grows pseudomorphically on W(001) at coverage's below five ML.[17-19] A single Fe ML orders antiferromagnetically,[20, 21] but a coverage of two or more ML leads to ferromagnetic ordering with in-plane anisotropy.[17-19] By means of DFT calculations we study as to what extend the two substrates, Fe(001) and Fe/W(001), lead to a difference in interaction with C_{60} molecules, and to differences in the interface spin polarization.

5.2 Computational results

The electronic and magnetic properties of the C_{60}/Fe(001) and C_{60}/Fe/W(001) interfaces are studied by DFT calculations using projector augmented wave (PAW) potentials and a plane wave basis set,[22, 23] as implemented in the Vienna Ab initio Simulation Package (VASP).[24, 25] Exchange and correlation are treated within the PBE formulation of the generalized gradient approximation (GGA).[26] Inclusion of van der Waals interactions is not necessary, as the interaction between Fe and C_{60} turns out to be chemisorption. We use a plane wave kinetic energy cutoff of 400 eV and a regular *k-point* grid with a spacing of 0.02 $Å^{-1}$ for the Brillouin zone sampling. We assume convergence when the difference of the total energies between two consecutive ionic steps is less than 10^{-5} eV and the maximum force allowed on each atom is 0.01 eV/Å. The calculated lattice constants of bulk bcc Fe and W are 2.83 and 3.17 Å, and the spin magnetic

moment per atom of bulk Fe is μ_S = 2.20 μ_B, in good agreement with the experimental values of 2.87, 3.16 Å and 2.22 μ_B.[27]

In agreement with previous studies, we find that the most stable magnetic order of a single Fe ML on W(001) is antiferromagnetic, whereas that of two or more Fe ML is ferromagnetic.[20, 21, 28] The calculated layer resolved μ_S of Fe(3 ML)/W(001) are given in Figure 5.1(a) (as the numbers between brackets). The enhancement of the surface μ_S, as compared to the bulk μ_S, is comparable to that in Fe(001). Not surprisingly, there is a difference in μ_S between the subsurface layers of Fe(001) and Fe/W(001), because of the proximity of the Fe/W interface. A small oscillating magnetization is induced in the W substrate. The interface W atoms have moments that are antiferromagnetically ordered with respect to the Fe overlayer, μ_S = −0.28 μ_B.[28] The moments in the sub-interface W layers are at least an order of magnitude smaller.

We model the possible adsorption structures of one C_{60} ML on Fe(001) and Fe/W(001) substrates using a 4×4 surface unit cell containing one C_{60} molecule. The molecules are then arranged in a square lattice with a distance of 11.3 and 12.7 Å between neighboring C_{60} molecules, respectively, which is fairly close to the nearest neighbor distance of 10.1 Å in the fcc C_{60} crystal. The Fe(001) and Fe/W(001) substrates are modeled by slabs of 7 Fe ML and 3 Fe ML/5 W ML, respectively, with the C_{60} molecule absorbed on one side of the slab. A dipole correction is included to prevent spurious interactions between the repeated images of the slab. The top three Fe atomic layers, the W atomic layer at the interface, and the atoms of the C_{60} molecule are allowed to relax upon adsorption. The most favorable adsorption structure of C_{60} on the Fe surface is determined by relaxing a large number of possible adsorption structures.

The lowest energy structure of C_{60}/Fe(001) is shown in Figure 5.1(b). The edge shared by two C_{60} hexagons (a double, or 6:6 bond) is on top of a surface Fe atom, indicated by a (red) circle. The C_{60} molecule is tilted such that one of the two edge-sharing hexagons is more parallel to the surface. Several Fe-C distances for C atoms in these two hexagons are in the range 2.0-2.5 Å. The corresponding C-C distances are in the range 1.46-1.52 Å, which is significantly larger than the 1.40, 1.46 Å of the 6:6, 5:6 bonds of isolated C_{60}. Only the structure of the C_{60} faces involving C atoms directly bonded to surface Fe atoms is modified, whereas the

remaining faces are changed very little compared to isolated C_{60}. The calculated binding energy of C_{60} to the surface is 2.9 eV, which indicates a strong bonding, consistent with our previous experimental evidence for significant hybridization effects at C_{60}/Fe(001) interfaces.[15] Indeed chemisorption of C_{60} is found for many metal substrates.[29, 30]

One may expect a strained Fe lattice to be even more reactive, and the calculated binding energy, 5.1 eV, of C_{60} to Fe/W(001) confirms this. The larger in-plane lattice constant of Fe/W also allows for a stronger perturbation of the lattice upon adsorption of C_{60}, as shown in Figure 5.1(a). The surface Fe atom below the 6:6 bond closest to the surface (marked by a red circle in Figure 5.1(a)) is pushed down into a row of the second Fe layer, and other Fe atoms relax as to maximize the bonding to C_{60}. Compared to adsorption on Fe(001), the C_{60} molecule sinks considerably deeper into the Fe/W(001) substrate. Note also that in the most favorable adsorption geometry the C_{60} molecule on the Fe/W substrate is rotated by 45° compared to its orientation on the Fe substrate.

The (layer averaged) moments μ_S of the C_{60}/Fe(001) and C_{60}/Fe/W(001) structures are also shown in Figure 1. In both these cases does adsorption of C_{60} lead to a reduction of μ_S on the substrate Fe atoms. For adsorption on Fe(001) the average reduction of the surface Fe μ_S is 6%, and it drops to half that value in the third Fe layer. Within an Fe layer the change in μ_S upon C_{60} adsorption is far from homogeneous. The surface Fe atom just below the 6:6 bond (marked in red in Figure 5.1(b)) has μ_S = 1.74 μB, which means a reduction of ~ 40% compared to the clean Fe(001) surface.

The average reductions of μ_S of the top two Fe layers in C_{60}/Fe/W are comparable to those in C_{60}/Fe, i.e., ~ 6%. Again the changes are inhomogeneous. For instance, the Fe atom just below the 6:6 bond (marked in red in Figure 5.1(a)) has a much stronger reduced μ_S = 1.60 μ_B. As this atom is pushed into the second layer by C_{60} adsorption, it also perturbs the moments of the surrounding Fe atoms. Most remarkably, its largest perturbation is on its neighboring Fe atoms in the third layer, where one of the atomic moments is even forced into anti-parallel with μ_S = −1.19 μ_B. The average μ_S of the third Fe layer is then reduced by 15%, as compared to the clean Fe/W substrate.

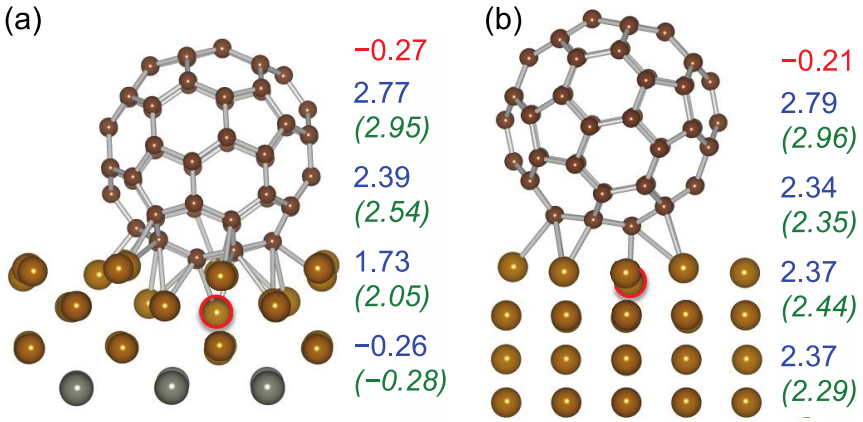

Figure 5.1 (a) C_{60}/Fe/W(001) structure viewed along the ⟨100⟩ direction. (b) C_{60}/Fe(001) structure viewed along the ⟨110⟩ direction. The numbers are the moments μ_S induced on the C_{60} molecules (red) and the layer averaged μ_S of the subsequent metal layers (blue). Between brackets are the layer resolved μ_S of the clean substrates.

5.3 Experimental results

5.3.1 Sample preparation

In situ sample preparation and measurements were carried out at beamline D1011 of the MAX- Laboratory in Lund, Sweden. The base pressure of the joint analysis/preparation chamber was 10^{-10} mbar. Ultrathin bcc-Fe films of ~3 ML were grown at room temperature onto a W(001) single crystal substrate using a mini e-beam evaporator. The samples were annealed at 460 °C to improve the structural quality of the Fe overlayers. Prior to Fe deposition, the W(001) single crystal substrate was cleaned by several oxidation and flash-annealing cycles. Oxidation of surface layers was carried out by annealing at 1000 °C for 10 minutes in 10^{-7} mbar oxygen. Subsequently, flash annealing to 1800 °C resulted in desorption of oxide layers and the recovery of a clean surface.[18]

The surface quality of the W(001) crystal and the pseudomorphic, epitaxial character of the bcc-Fe layers were monitored by low energy electron diffraction (LEED), as shown in Figure 5.2. A C_{60} layer of several nm thick was deposited

onto the annealed Fe/W(001) samples by thermal evaporation using a custom-built Knudsen-cell. The LEED pattern of the single crystal W(001) substrate after cleaning showed a sharp (1 × 1) diffraction pattern. No additional features of super-structures were observed, implying a high substrate quality.

The ultra-thin Fe film on W(001) showed already a fairly high degree of structural order as-grown, which can be observed from the clear spots in the LEED pattern of Figure 5.2(b). The crystallinity of the pseudomorphic Fe overlayers was further improved after annealing, resulting in the sharp LEED pattern of Figure 5.2(c). In line with earlier observations of strain relief setting in at a coverage of about 5 ML,[18, 19] we observed a slightly blurred LEED pattern for ~6 ML Fe (not shown). In the following, we will focus on the results obtained for the Fe(3 ML)/W(001) sample.

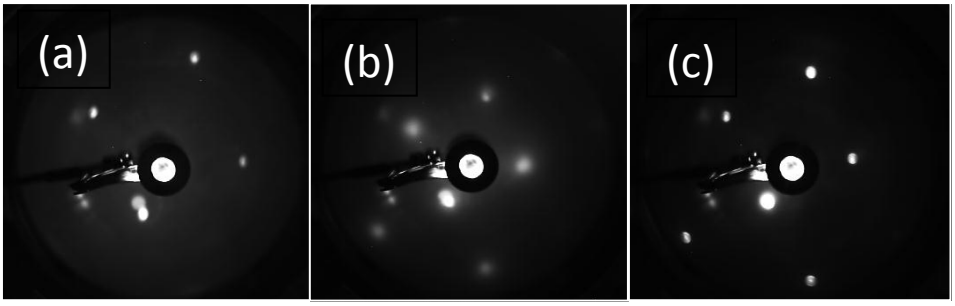

Figure 5.2 LEED patterns of (a) W(001) substrate, (b) as-grown ~3 ML Fe on W(001) and (c) after annealing at 460 °C.

5.3.2 Spin and orbital magnetic moments of Fe

In order to determine the Fe spin- and orbital magnetic moments, we used XMCD.[31-34] We measured XMCD spectra at the Fe $L_{2,3}$ edges before and after C_{60} deposition and use the XMCD sum rules to calculate the spin- and orbital magnetic moments.[33, 34] The XAS spectra were measured at room temperature in the total electron yield (TEY) mode. The angle of incidence of the photon beam was set to 60° relative to the sample normal, while the degree of circular polarization was

75%. XMCD spectra were obtained in remanence, by taking the difference between the XAS spectra recorded with opposite in-plane magnetization directions.

The samples were magnetized by applying an in-plane magnetic field pulse of 300 Oe. The magnetic field was applied at an oblique in-plane angle, in between the ⟨110⟩ and ⟨100⟩ directions, i.e. neither along the magnetic easy axis, nor along the hard axis.[18] In addition, the limited magnetic field strengths available at the beamline might be insufficient for saturating the magnetization of the films,[18] such that the remanent magnetization might be expected to be smaller than the saturation magnetization of the films. Hence we expect that the magnetic moments extracted from the XMCD data using the sum rules are underestimated. However, this is of minor importance for the present study, since we are interested in relative changes to the moments induced by C_{60} adsorption.

Figure 5.3(a) shows the XAS and XMCD spectra, as well as the integrated XMCD intensity, recorded at the Fe $L_{2,3}$ edges for Fe(3 ML)/W(001). The inset shows the sum of the XAS spectra recorded with opposite photon helicity, and its integral. The XMCD spectra have been corrected by taking into account the incident angle (30° with respect to the sample surface) and the degree of circular polarization (75%), by multiplying the measured spectra by [1/cos(30°)]/0.75, while keeping the sum spectra the same.[31] Using the established sum rules,[33, 34] we obtain the spin and orbital magnetic moments, μ_S and μ_L, from the integrals of the XAS and XMCD spectra as [31, 33, 34]

$$\mu_S = -\frac{6p-4q}{r} n_h,\ \mu_L = -\frac{4q}{3r} n_h \tag{5.1}$$

Here n_h is the number of holes, where we use n_h = 3.39.[31] The quantities p, q and r are indicated in Figure 5.3. The small term proportional to the expectation value of the magnetic dipole operator was neglected in the determination of μ_S.[31] The values we obtain for the Fe(3 ML)/W(001) sample are μ_S =0.83 μ_B and μ_L =0.038 μ_B.

These values are considerably smaller than the saturation values for Fe, as expected (see discussion above). It should be noted in passing that μ_L/μ_S = 0.046, which is only slightly higher than the bulk value of 0.043.[31] This is somewhat surprising, since for ultrathin 3d transition metal films this ratio is typically

enhanced, due to film-substrate *d-orbital* interaction, and lifting of the orbital degeneracy by symmetry reduction at the surface.[28-32] In this respect the magnetic properties of the Fe/W(001) interface are somewhat special.

The XAS and XMCD spectra recorded at the Fe $L_{2,3}$ edge of the Fe/W(001) sample, covered by a C_{60} overlayer of several nm thick, are shown in Figure 5.3(b). Using Eq. 5.1 we obtain μ_S = 0.78 μ_B and μ_L = 0.126 μ_B, leading to a ratio μ_L/μ_S = 0.161. Compared to the results obtained for the clean Fe/W(001) substrate, μ_S is reduced by 6%, whereas the μ_L/μ_S ratio is strongly increased by 250%. Enhanced orbital moments of 3d transition metal systems typically originate from an increased degree of 3d wave function localization (see, for example, Ref.[23]), which in the present case should result from hybridization between the Fe 3d states and the C_{60} orbitals.

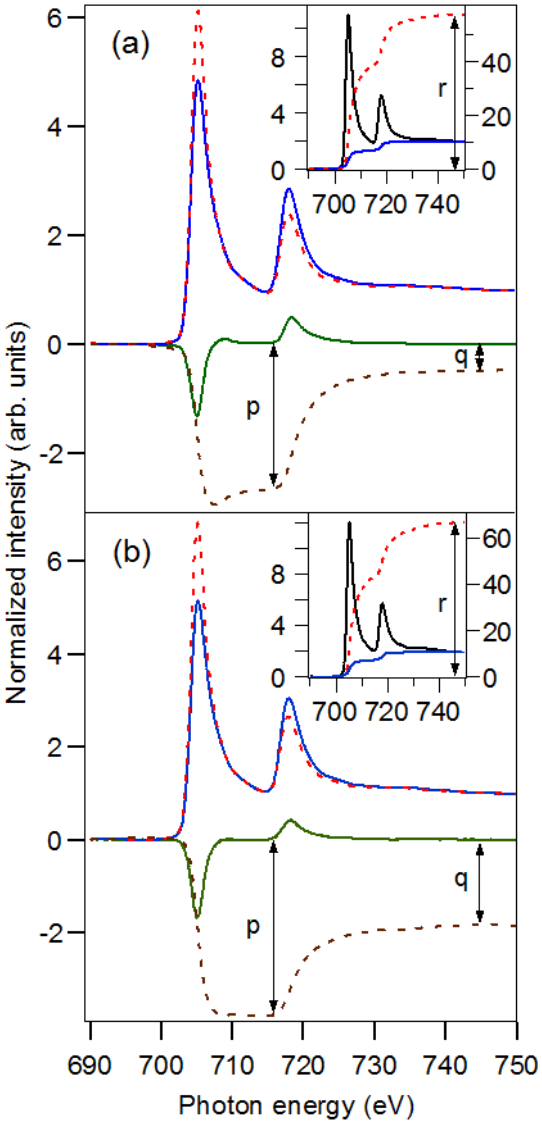

Figure 5.3 XAS spectra recorded at opposite remanent magnetization (red and blue) and the corresponding XMCD spectra (green) plus integrated XMCD intensity (brown) at the Fe $L_{2,3}$ edges, of (a) 3MLs of Fe on W(001) and (b) the same sample after deposition of several nm of C_{60}. The XAS spectra were normalized on the step height above 740 eV photon energy, where dichroic effects are absent. Insets show the summed XAS spectra and their integrals. A stepped

background (blue) was subtracted from the summed XAS spectra prior to integration, following the procedure developed by Chen *et al*.[31]

5.4 Discussion

The relative changes in μ_S upon adsorption of C_{60}, extracted from the experiment and from the calculations, agree quite well. The interfacial bonding between the Fe surface and the C_{60} molecules results from hybridization between the 3d orbitals of the Fe surface atoms and the frontier π orbitals of C_{60}, which we have previously observed using C K-edge XAS and XMCD measurements.[15] The hybrid interface states have metallic character and they give rise to a magnetic moment μ_S = −0.21, −0.27 μ_B on the C_{60} molecule for adsorption on Fe(001) and Fe/W(001), respectively. This moment is antiferromagnetically ordered with respect to those of the Fe substrate atoms, as are the moments on the W atoms in the Fe/W substrate, see Figure 5.1(a). The magnitude and sign of the spin polarization of C_{60}-derived states depends strongly on binding energy, in agreement with experiments.[15] Close to the Fermi energy (within plus or minus 0.5 eV), the maximum value reached is about 2:1 (minority:majority spin DOS of occupied orbitals).

The effect of hybridization on the Fe surface can be analyzed using the projected density of states (PDOS), as shown in Figure 5.5. Compared to the top layer of the clean Fe(001) surface, the PDOS of the Fe interface layer of the C_{60}/Fe(001) system is slightly decreased (increased) for majority (minority) spin below the Fermi level, see Figure 5.4(a), consistent with a reduced spin polarization. These changes are not homogeneous in the Fe(001) plane, as only part of the Fe atoms bind to C_{60} directly. Figure 5.4(b) shows the PDOS projected on a Fe atom that is strongly bonded to C_{60} (the atom marked red in Figure 5.1(b)), compared to a surface atom on the clean Fe(001) surface. The minority spin PDOS of the clean Fe(001) surface just above the Fermi level is dominated by peaks resulting from *d-states* that have a large amplitude (or are even localized) at the surface.

Upon adsorption of C_{60} these peaks are suppressed, as the corresponding states participate in the bonding to the adsorbate. In Figure 5.4(b), hybrid bonding states appear in the minority spin channel at an energy ~ −2 to −4 eV.

Concurrently, the majority spin PDOS in the latter energy region is reduced by bonding to the adsorbate, and an antibonding hybrid state appears just below the Fermi energy. These changes lead to a strongly reduced magnetic moment on this particular Fe atom, as discussed above.

Figure 5.4(c) shows the PDOS projected on the three Fe layers of the Fe/W(001) system before (red) and after (blue) adsorption of C_{60}. In detail the PDOS is different from that of the pure Fe substrate, Figure 5.4(a), but the overall trend is the same, and adsorption of C_{60} decreases (increases) the majority (minority) spin PDOS of the occupied states. Projecting on a Fe atom strongly involved in bonding to C_{60} (the atom marked red in Figure 5.1(a)) gives the PDOS shown in Figure 5.4(d). The pattern is quite comparable to that observed for the pure Fe substrate in Figure 5.4(b). The similarity between the C_{60}/Fe(001) and C_{60}/Fe/W(001) systems is quite remarkable, in view of the structural differences between the two substrates before and after adsorption of C_{60}. One can conclude that such structural differences are not so important for the magnetic and electronic properties of these systems.

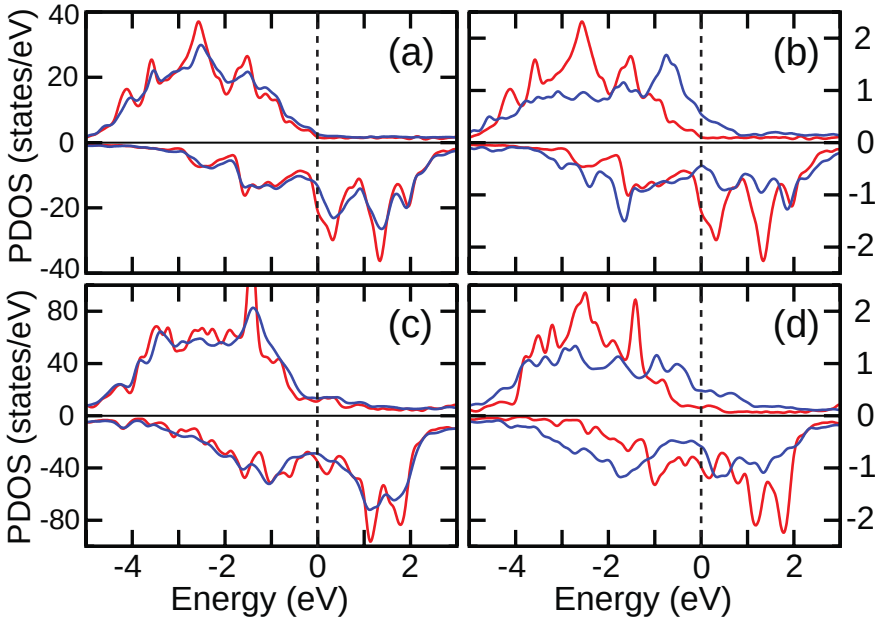

Figure 5.4 (a) PDOS of majority (top) and minority (bottom) spin states projected on the top Fe layer at the C_{60}/Fe(001) interface (blue), compared to the PDOS of a clean Fe(001) surface layer (red); (b) PDOS of the most strongly affected Fe atom (blue), compared to the PDOS of a clean Fe(001) surface atom; (c,d) as (a,b), but for the Fe/W(001) substrate.

5.5 Conclusions

By a joint computational and experimental approach, we have characterized well-defined interfaces between C_{60} molecules and Fe(001) surfaces, which have high relevance for organic spintronics. Hybridization between the frontier orbitals of C_{60} and Fe 3d states has a strong effect on the spin polarization of the interface, which underlines the potential of chemical tuning of OSC/FM "spinterfaces" for spintronic devices.

Our calculations show that the hybrid interface states lead to magnetic moments on the C_{60} molecules that are coupled antiparallel to the Fe moments: μ_S =

−0.21 and −0.27 μ_B per molecule for adsorption on Fe(001) and Fe/W(001), respectively. The moments of the Fe atoms at the interface are also affected significantly.

XMCD experiments of 3 MLs of Fe on W(001) show that the overall Fe spin moment reduces by 6% after adsorption of C_{60}. This is in good agreement with the calculated values for both C_{60}/Fe(001) and C_{60}/Fe/W(001), which show a similar spin-dependent electronic structure at the hybrid interfaces, in spite of their significant structural differences. It should be noted, however, that a direct comparison of the reduction of the magnetic moments obtained from experiments and calculations should be made with care, since the effects are far from homogeneous.

References

1. W. J. M. Naber, S. Faez and W. G. v. d. Wiel, J. Phys. D **40**, R205 (2007).
2. V. Dediu, L. E. Hueso, I. Bergenti and C. Taliani, Nat. Mater. **8**, 707 (2009).
3. R. Lin, F. Wang, M. Wohlgenannt, C. He, X. Zhai and Y. Suzuki, Synth. Met. **161** (7-8), 553 (2011).
4. T. S. Santos, J. S. Lee, P. Migdal, I. C. Lekshmi, B. Satpati and J. S. Moodera, Phys. Rev. Lett. **98**, 016601 (2007).
5. C. Barraud, P. Seneor, R. Mattana, S. Fusil, K. Bouzehouane, C. Deranlot, P. Graziosi, L. Hueso, I. Bergenti, V. Dediu, F. Petroff and A. Fert, Nat. Phys. **6** (8), 615 (2010).
6. T. L. A. Tran, T. Q. Le, J. G. M. Sanderink, W. G. van der Wiel and M. P. de Jong, Adv.Funct. Mater. **22** (6), 1180 (2012).
7. Z. H. Xiong, D. Wu, Z. V. Vardeny and J. Shi, Nature **427**, 821 (2004).
8. V. Dediu, L. E. Hueso, I. Bergenti, A. Riminucci, F. Borgatti, P. Graziosi, C. Newby, F. Casoli, M. P. d. Jong, C. Taliani and Y. Zhan, Phys. Rev. B **78**, 115203 (2008).
9. J. J. H. M. Schoonus, P. G. E. Lumens, W. Wagemans, J. T. Kohlhepp, P. A. Bobbert, H. J. M. Swagten and B. Koopmans, Phys. Rev. Lett. **103** (14), 146601 (2009).
10. M. Gobbi, F. Golmar, R. Llopis, F. Casanova and L. E. Hueso, Adv. Mater. **23** (14), 1609 (2011).

11. R. Lin, F. J. Wang, M. Wohlgenannt, C. Y. He, X. F. Zhai and Y. Suzuki, Synth. Met. **161** (7-8), 553 (2011).
12. M. Gobbi, A. Pascual, F. Golmar, R. Llopis, P. Vavassori, F. Casanova and L. E. Hueso, Org. Electron. **13** (3), 366 (2012).
13. S. Sanvito, Nat. Phys. **6**, 562 (2010).
14. Stefan Schmaus, Alexei Bagrets, Yasmine Nahas, Toyo K. Yamada, Annika Bork, Martin Bowen, Eric Beaurepaire, Ferdinand Evers and a. W. Wulfhekel, Nat. Nanotechnol. **6** (2011).
15. T. L. A. Tran, P. K. J. Wong, M. P. de Jong, W. G. van der Wiel, Y. Q. Zhan and M. Fahlman, App.l Phys. Lett. **98** (22) (2011).
16. S. L. Kawahara, J. Lagoute, V. Repain, C. Chacon, Y. Girard, S. Rousset, A. Smogunov and C. Barreteau, Nano Lett. **12** (9), 4558 (2012).
17. T. L. Jones and D. Venus, Surf. Sci. **302** (1–2), 126 (1994).
18. W. Wulfhekel, F. Zavaliche, R. Hertel, S. Bodea, G. Steierl, G. Liu, J. Kirschner and H. P. Oepen, Phys. Rev. B **68** (14) (2003).
19. K. von Bergmann, M. Bode and R. Wiesendanger, Phys. Rev. B **70** (17), 174455 (2004).
20. D. Spišák and J. Hafner, Phys. Rev. B **70** (19), 195426 (2004).
21. A. Kubetzka, P. Ferriani, M. Bode, S. Heinze, G. Bihlmayer, K. von Bergmann, O. Pietzsch, S. Blügel and R. Wiesendanger, Phys. Rev. Lett. **94** (8), 087204 (2005).
22. P. E. Blöchl, Phys. Rev. B **50** (24), 17953 (1994).
23. G. Kresse and D. Joubert, Phys. Rev. B **59** (3), 1758 (1999).
24. G. Kresse and J. Hafner, Phys. Rev. B **47** (1), 558 (1993).
25. G. Kresse and J. Furthmüller, Phys. Rev. B **54** (16), 11169 (1996).
26. J. P. Perdew, K. Burke and M. Ernzerhof, Phys. Rev. Lett. **77** (18), 3865 (1996).
27. C. Kittel, (Wiley: NewYork, 1996).
28. P. Ferriani, S. Heinze, G. Bihlmayer and S. Blügel, Phys. Rev. B **72** (2), 024452 (2005).
29. H. I. Li, K. Pussi, K. J. Hanna, L. L. Wang, D. D. Johnson, H. P. Cheng, H. Shin, S. Curtarolo, W. Moritz, J. A. Smerdon, R. McGrath and R. D. Diehl, Phys Rev Lett **103** (5), 056101 (2009).
30. X.-Q. Shi, M. A. Van Hove and R.-Q. Zhang, Phys Rev B **85** (7), 075421 (2012).

31. C. T. Chen, Y. U. Idzerda, H. J. Lin, N. V. Smith, G. Meigs, E. Chaban, G. H. Ho, E. Pellegrin and F. Sette, Phys. Rev. Lett. **75** (1), 152 (1995).
32. G. van der Laan, Phys. Rev. Lett. **82** (3), 640 (1999).
33. P. Carra, B. T. Thole, M. Altarelli and X. Wang, Phys. Rev. Lett. **70** (5), 694 (1993).
34. B. T. Thole, P. Carra, F. Sette and G. van der Laan, Phys. Rev. Lett. **68** (12), 1943 (1992).

CHAPTER 6

Highly ordered C_{60} films on epitaxial Fe/MgO(001) surfaces for organic spintronics

Hybrid interfaces between ferromagnetic surfaces and carbon-based molecules play an important role in organic spintronics. The fabrication of devices with well defined interfaces remains challenging however, hampering microscopic understanding of their operation mechanisms. We have studied the crystallinity and molecular ordering of C_{60} films on epitaxial Fe/MgO(001) surfaces, using X-ray diffraction and scanning tunneling microscopy (STM). Both techniques confirm that fcc -molecular C_{60} films with a (111)-texture can be fabricated on epitaxial bcc-Fe(001) surfaces at elevated growth temperatures (100-130 °C). STM measurements show that C_{60} monolayers deposited at 130 °C are highly ordered, exhibiting quasi-hexagonal arrangements on the Fe(001) surface oriented along the [100] and [010] directions. The mismatch between the surface lattice of the monolayer and the bulk fcc-C_{60} lattice prevents epitaxial overgrowth of multilayers.

This chapter has been published, in slightly modified form, as P. K. J. Wong, T.L.A. Tran, P. Brinks, W.G. van der Wiel, M. Huijben, and M.P. de Jong, Org. Electron. 14, 451 (2013)

6.1 Introduction

Hybrid ferromagnet (FM)/organic interfaces have become a subject of intensive research since the last decade, as fueled by observations of strong magnetoresistance (MR) effects in FM/organic spin-valves.[1-4] This has sparked the development of a new research field, which has been coined "organic spintronics", aiming to (i) establish additional functionality in organic electronic devices via active use of charge carrier spins, or (ii) to incorporate organic materials into spintronic devices.

The central motivation for utilizing organic materials as hosts for spin polarized charge carriers relies on their weak spin-orbit coupling and hyperfine interaction. This holds great promise for attaining long spin lifetimes, offering prospects for robust spin manipulation and readout in organic spintronic devices.[5, 6] It is noteworthy, however, that many of the previously examined spin-valve structures featured ill-defined FM/organic interfaces, and failed to offer a reliable picture of the physical mechanisms behind the spin-dependent effects. In order to harness the full potential of this infant yet promising field, systematic investigations of the effects of structural, electronic, and magnetic properties of the FM/organic interfaces on spin injection, transport and extraction are very important. Unlike ill-defined interfaces, which often plague experiments and hamper theoretical modeling, clean, well-characterized and structurally ordered hybrid interfaces should make studies of such kind much more informative, therefore paving the way to the understanding of novel spin physics involved at the heterojunctions.

Interfaces comprised of C_{60} and bcc-Fe(001) form interesting model systems for organic spintronics, due to the following reasons. (1) Bcc-Fe(001) features fully spin-polarized Δ_1-electrons, which produces very high tunneling MR when combined with a crystalline MgO tunnel barrier.[7] It is interesting to investigate whether similar effects can be exploited at structurally ordered Fe/organic interfaces. (2) C_{60} lacks hydrogen and the associated spin dephasing mechanism by hyperfine coupling (the predominantly present ^{12}C isotopes have zero nuclear spin). (3) The high electron affinity of C_{60} (of about 4 eV) [8] results in small energy barriers for electron injection at the interfaces with 3*d* transition metal FMs, such that devices can be operated at low bias, which is beneficial for attaining a high spin polarization of the injected current. (4) Finally, C_{60} molecules have

been observed to form well ordered (and in some cases even epitaxial) layers on a variety of surfaces as we will address below, due to the non-stringent requirements for surface energy- and lattice matching typical for organic semiconductors. In contrast to inorganic materials, epitaxial and well-ordered growth of organic semiconductors therefore might be achieved even on lattice-mismatched substrates. Our previous studies on the electronic and magnetic properties of C_{60}/bcc-Fe(001) interfaces, using synchrotron-based core-level electron spectroscopies, revealed significant hybridization between the π-electronic states of C_{60} and the 3*d*-bands of the Fe surface, which induces a strong magnetic polarization of C_{60}-derived electronic orbitals.[9] The presence of such spin-dependent hybridization is critical, since it is expected to play a decisive role in spin transport across the hybrid interface.[3] Moreover, the strong interfacial interaction will certainly exert a non-trivial impact on the growth mechanism and structural properties of C_{60} overlayers on Fe(001) surfaces, as is also the case for C_{60} on Al,[10] Cu,[11] and Ni surfaces.[12] This particularly interesting aspect forms the core of this present work. Using a combinatorial approach of X-ray diffraction (XRD) and scanning tunneling microscopy (STM), we give insight into the crystallinity and local structural ordering of C_{60} molecules, that could be accomplished atop epitaxial bcc-Fe(001) films on MgO(001) for organic spintronic applications.

6.2 Experimental methods

Our C_{60}/Fe bilayer films were prepared onto single-crystalline MgO(001) substrates in a UHV molecular-beam epitaxy system with a base pressure of 10^{-10} mbar. The commercial MgO(001) substrates used in this experiment exhibited a root mean square roughness of about 0.15 nm. Prior to any *in-situ* treatment, the substrates were ultrasonically cleaned thoroughly in acetone, ethanol and isopropanol at 50 °C. While in UHV, the substrates were thermally annealed at 450 ^{o}C for 60 min to obtain clean surfaces, on top of which a 10-nm thick epitaxial Fe(001) film was grown by e-beam evaporation at a rate of 0.9 nm/min at an elevated substrate temperature of 150 ^{o}C. C_{60} multilayers with a thickness of about 100-nm were then deposited onto the Fe(001) by thermal evaporation from a Knudsen-cell (operated at 500 ^{o}C) at a rate of 3.3 nm/min and with a substrate temperature of 100 ^{o}C. The crystallinity and structural properties of these so-fabricated film stacks were characterized *ex-situ* by XRD. The XRD measurements

were carried out on a Bruker AXS D8 DISCOVER diffractometer using Cu Kα radiation (wavelength: 0.154 nm) equipped with a four-circle goniometer.

To investigate the adsorption mechanism and local structural ordering of C_{60} on the epitaxial Fe(001) surface down to the molecular scale, we used a commercial UHV-STM with an interconnected custom-made sample preparation chamber. C_{60}/Fe/MgO(001) samples were prepared under similar experimental conditions as described above. In order to obtain reliable electrical contacts between the deposited films and the sample holder, two 30-nm thick W strips were sputtered *ex-situ* on both edges of the insulating MgO substrates using a dedicated DC-sputtering tool. These strips were found to be very stable against any thermal (cleaning) treatments, without causing any detectable diffusion of W atoms across the surface. STM images were acquired in constant current mode using mechanically cut Pt-Ir tips at room temperature (RT) with a set-point current of 0.8 nA and a bias voltage of 230 mV.

6.3 Results and discussion

6.3.1 Structural characterization by X-ray diffraction

Fig. 6.1(a) shows a XRD θ-2θ scan of a 100 nm C_{60}/10 nm Fe/MgO(001) sample, from which the diffraction peaks of fcc-C_{60} (111), (222) and (333), bcc-Fe (002), and MgO (002), as labelled, are clearly observed. When compared to the powder diffraction pattern of C_{60} [13] and XRD measurements of C_{60} films on other metal substrates,[14] the existence of only (hhh) diffraction peaks from our C_{60} film indicates a fcc-(111) texture. Figs. 6.1(b)-1(d) show the ω scans, or rocking curves, of the MgO(002), Fe(002), and C_{60} (111) diffraction peaks, respectively. We fitted each rocking curve with a Gaussian function in order to extract the full-width at half maximum (FWHM), a parameter that quantifies the crystallinity along the film normal. A small FWHM value of 0.03° for MgO(002) peak confirms the high crystallinity of the MgO(001) substrates we used in this study, while the FWHM values for Fe(002) and C_{60}(111) are larger, 1.56° and 2.51°, due to the lower thickness and higher defect density of the deposited layers. We will elaborate this specific point in later paragraphs. Interestingly, the C_{60}(111) rocking curve in Fig. 6.1(d) exhibits two parts: a sharp narrow peak superimposed on a much broader peak, which is characteristic for weakly disordered systems.[15] The lattice mismatch between the C_{60} layer and the Fe/MgO stack underneath (see further discussion

below) results in the formation of dislocations. The non-uniformity of the strains concentrated at the dislocation gives rise to diffuse scattering. When the dislocation density is large, the diffraction peak from the C_{60} layer is broadened, due to short-range correlations in positions of the atoms. The intensity of the narrow coherent peak, reflecting the long-range correlations, is small. The φ-scans of the same sample in Fig. 6.1(e), which probe the in-plane lattice matching of substrate and adlayers, reveal an epitaxial relationship between the MgO substrate and the Fe layer. As shown, the in-plane signals corresponding to the Fe epitaxial film are always 45° off from those detected from the MgO(001) substrate, which is in good agreement with the previously reported epitaxial relationship of Fe(001)[100]//MgO(001)[110].[16] However, no diffraction peaks containing an in-plane component could be detected for the (100 nm thick) C_{60} layer, indicating the absence of an in-plane structural relationship between the C_{60} layer and the Fe/MgO stack underneath. This suggests either a complete in-plane disorder, or the presence of only short-range molecular order in the plane of the C_{60} film. Given that the sensitivity of XRD for the interface region is limited, however, some degree of in-plane ordering may be present for ultrathin films. We will address this issue next, using STM measurements.

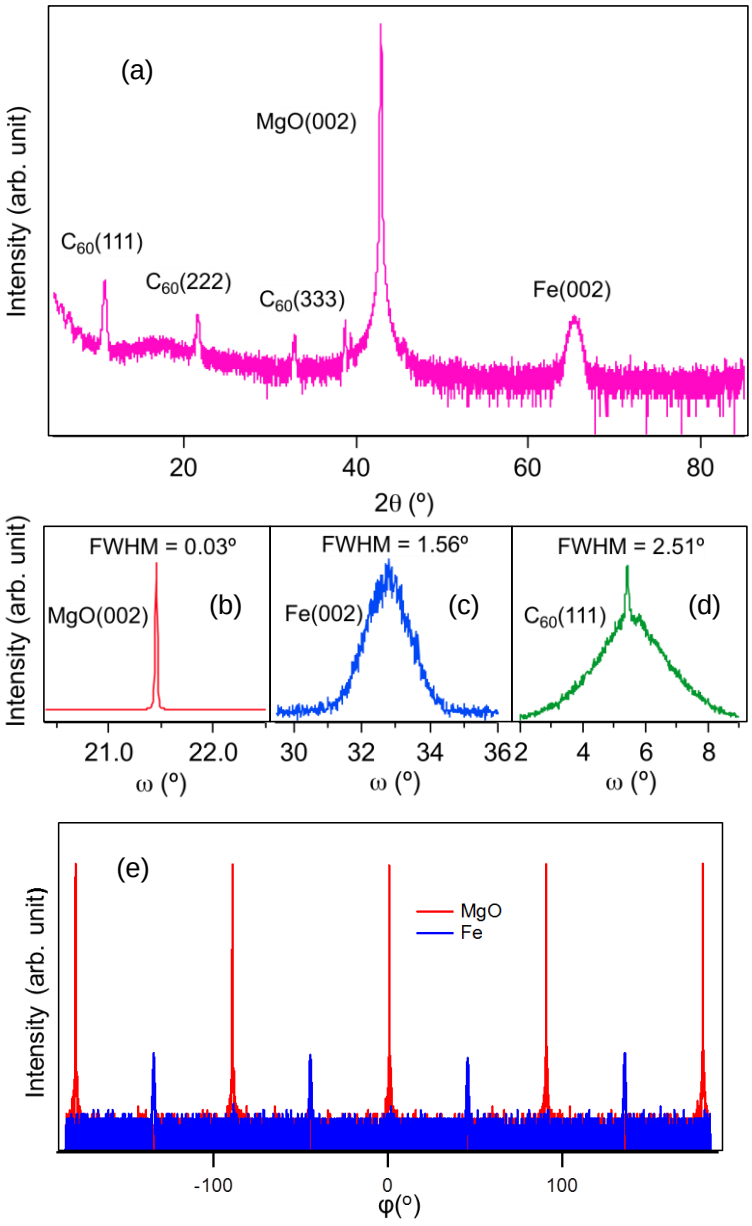

Figure 6.1. XRD measurements of 100-nm C_{60}/10-nm Fe/MgO(001). (a) Wide-angle θ-2θ scan; (b)-(d) ω-scans or rocking curves for MgO(002), Fe(002) and C_{60}(111) diffraction peaks; (e) φ-scan for MgO(022) and C_{60}-capped Fe(022) peaks.

6.3.2 Surface morphology and molecular ordering by scanning tunneling microscopy

Fig. 6.2 shows a series of STM images, capturing the surface morphology at different stages of C_{60} monolayer (ML) fabrication by thermal desorption of its multilayers (deposited at RT) on an Fe(001) surface. Similar procedures have been adopted and described in our previous report on the electronic/magnetic structure at the ML C_{60}/Fe(001) interface.[9] Fig. 6.2(a) depicts an STM image of a 10-nm thick Fe(001) film epitaxially grown on a clean MgO(001) surface at 150 °C. Previous studies have shown that two-dimensional growth of bcc-Fe on MgO(001) is only possible at or above a critical temperature such that the Schwöbel barrier for downward step diffusion can be overcome.[17, 18] Indeed, the observation of an atomically flat Fe film surface, with well-defined terraces and step structures that align along the Fe[100] or MgO[110] crystallographic directions confirms this thermodynamic growth process, and also serves as evidence for high-quality epitaxial growth. The pits observed in the film are due to screw dislocations, which are structural defects that result from the lattice mismatch of 3.8% between bcc-Fe and the (45º rotated) rock-salt structure of MgO(001). Although larger Fe terraces could be obtained using a higher growth temperature than that used in this present experiment, as revealed by our AFM measurements (not shown), the resulting films consisted of many discontinuous Fe terraces, hampering any STM measurement due to poor electrical conductivity. Fig. 6.2(b) illustrates the sample morphology with a C_{60} multilayer on top of the Fe surface. The C_{60} deposition at RT essentially washes out the atomic step structures of the Fe film, although the deep pits due to screw dislocations remain discernable. The high density of voids also suggests that the C_{60} growth proceeded with a three-dimensional island-growth mode. At this point, we conclude that no structural ordering of the C_{60} film exists, and that the multilayer can thus be described as amorphous-like. With a brief anneal at 280 °C for 3 minutes, a substantial part of the C_{60} molecules appear to have been desorbed from the surface, judging from the partial recovery of the Fe surface morphology (Fig. 6.2(c)). This is in good agreement with our x-ray absorption spectroscopy data in Ref. 10, (refer to chapter 4) which shows that annealing at or above 280 °C results in desorption of C_{60} overlayers, while a ML of chemisorbed C_{60} molecules is retained at the surface. These molecules are bound by the strong interaction with the underlying Fe layer, which is apparent from the

hybridization-induced modifications of the C_{60} π^*-orbitals.[9] A close-up image of the annealed film, Fig. 6.2(d), reveals that the residual C_{60} molecules remain largely disordered. Figs. 6.2(e) and 6.2(f) show the same surface after an additional 3 minutes of annealing at the same temperature. Now, short-ranged ordered areas can be observed, such as those marked with blue arrows in Fig. 6.2(f), embedded in a still largely disordered environment.

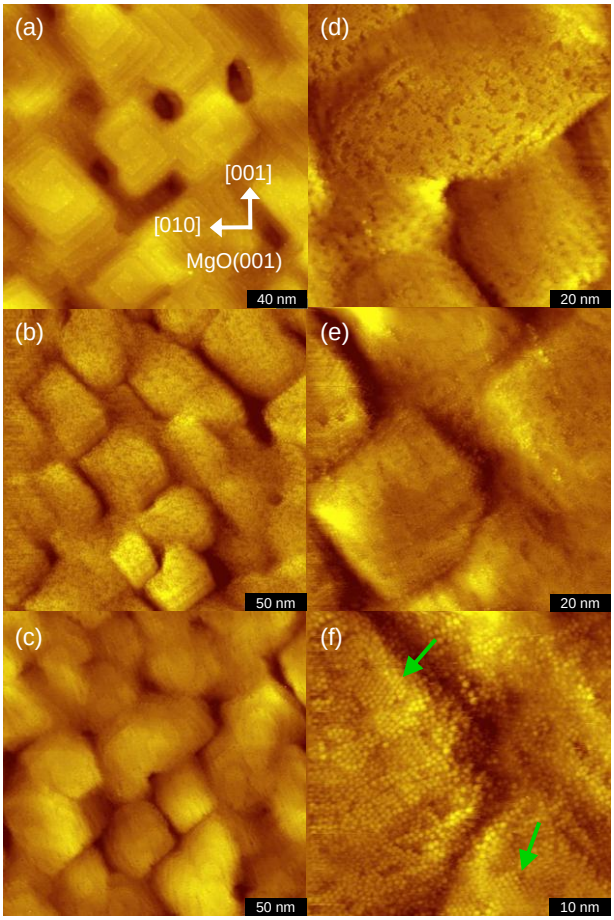

Figure 6.2. Surface morphology of C_{60}/10-nm Fe/MgO(001) acquired by STM at RT. (a) Epitaxial Fe(001) surface grown on MgO(001). The arrows show the crystallographic directions of the MgO(001) substrate; (b) after C_{60} multilayer deposition at RT; (c) after annealing at 280 °C for 3 min; (d) molecular resolution image of (c); (e) after further annealing at 280 °C for 3 min; (f) molecular resolution image of (e). The blue arrows indicate areas where (short-range) C_{60} molecular ordering can be seen.

Next, we consider the case of a (partial) C_{60} monolayer obtained by adsorbing molecules onto a hot Fe(001) surface. Dosing C_{60} molecules onto substrates held at elevated temperatures is known to result in the growth of highly ordered monolayer films on various metal substrates that feature different interaction strengths with C_{60}.[10-12, 19, 20] Depending on the nature of the interfacial interaction, the adsorbed molecules may require a higher thermal energy to attain an equilibrium arrangement on a given substrate surface, which defines a temperature window within which growth of highly ordered MLs may be realized.

Figs. 6.3(a) and 6.3(b) show molecular resolution STM images of a C_{60} ML on Fe(001) grown at a deposition temperature of 130 °C (comparable to the growth temperature of the 100 nm C_{60} film that was analyzed with XRD). Fast Fourier transform (FFT) images for several selected areas, marked by contours, are shown as insets in Figs. 6.3(a) and 6.3(b). The STM images and their FFTs clearly reveal that the ML is highly ordered, and that the C_{60} molecules are packed in a quasi-hexagonal arrangement. Intermolecular distances determined from the various STM images that we recorded are consistently close to 1 nm, while the slightly asymmetric FFT spot patterns indicate a periodic structure consisting of distorted hexagons, with aspect ratios of 1.1 for the long/short diagonals connecting the corner points. Two distinct orientations of the C_{60} adsorbate lattice on the Fe(001) surface could be observed, rotated by 90 degrees, such as those shown within the red and green contours in Fig. 6.3(b) containing rows of molecules that are either along the Fe[100] or [010] directions (indicated by the blue arrows). These findings are consistent with the proposed structure shown in Fig. 6.3(c), comprising C_{60} molecules in equivalent adsorption sites on the Fe(001) surface. The description of the unit cell of this quasi-hexagonal overlayer structure requires matrix notation:

$$\begin{bmatrix} \overrightarrow{b_1} \\ \overrightarrow{b_2} \end{bmatrix} = \begin{pmatrix} 4 & 0 \\ 2 & 3 \end{pmatrix} \begin{bmatrix} \overrightarrow{a_1} \\ \overrightarrow{a_2} \end{bmatrix},$$

where $\boldsymbol{a}_1$, $\boldsymbol{a}_2$ and $\boldsymbol{b}_1$, $\boldsymbol{b}_2$ are the unit cell vectors of the Fe and C_{60} lattices, respectively. Taking the Fe lattice constant to be 0.287 nm, the lengths of the C_{60} unit cell vectors are 1.148 nm and 1.035 nm, implying an aspect ratio 1.109 of the distorted hexagonal lattice, in good agreement with the experiments. The length of the shorter unit cell vector is very close to the intermolecular distance of 1.002 nm

in the (111) planes of the fcc lattice of bulk C_{60} (which has a lattice constant of 1.417 nm), while the length of the longer unit cell vector deviates by more than 10%.

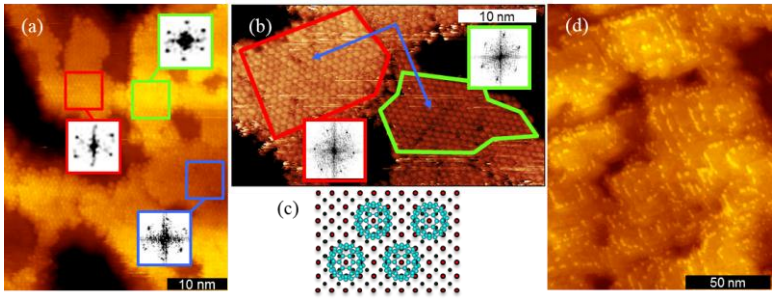

Figure 6.3. (a) Surface morphology of a ML of C_{60} on 10-nm Fe/MgO(001) with C_{60} deposited at a substrate temperature of 130 °C. The insets show FFT images of selected areas as marked by contours; (b) Another area of the same sample as in (a) where different orientations of the C_{60} surface structure on Fe(001) are observed, rotated by 90 degrees relative to each other. The blue arrows indicate the Fe [100] and [010] directions, the insets show FFT images of the areas enclosed by the red/green contours; (c) proposed surface structure of the C_{60} ML on Fe(001). Red (blue) dots indicate the positions of the Fe atoms in the first (second) layer of the bcc surface; (d) Surface structure of a sub-ML C_{60} on 10-nm Fe/MgO(001), where atomic steps are preferentially occupied by C_{60}, forming chains of molecules.

We propose that the lattice mismatch between the first ML of C_{60} on Fe(001) and the bulk structure is a primary cause for the absence of a well-defined in-plane ordering in multilayer films. Sakurai *et al.* reported that epitaxial C_{60} films can be obtained on lattice-mismatched substrates such as MoS_2,[21] due to the weak van der Waals-type interfacial interaction, such that C_{60} molecules can arrange themselves incommensurate with the MoS_2 lattice. On the contrary, for systems featuring a strong interaction, such as in the present case or, for example, C_{60} on Ni(110),[16] a good lattice match becomes a prerequisite for epitaxial growth. It should be noted that strong chemical interactions, involving spin polarized hybrid orbitals, typically occur at interfaces between transition metal ferromagnets and π-conjugated carbon systems.[3, 9, 22-24] A further complication is the non-negligible disorder that is observed in the STM images of the ML C_{60} films (see Fig. 6.3).

By examining the adsorption mechanism and molecular arrangement of C_{60} at the sub-ML regime, we conclude that atomic step structures on the Fe(001)

surface may partly account for this disorder. It is shown in Fig. 6.3(d) that the most probable sites for C_{60} nucleation are atomic steps, where the adsorbed molecules form chains in parallel to those of the edges. Such initial nucleation has been similarly observed on Bi(001)/Si(111), where a high density of screw dislocations is also present.[25] Diffusing adatoms or molecules, which encounter a step can either be reflected at the step or cross the step. In the latter situation, they can then either continue diffusing or adsorb at the step edge. For C_{60} on Fe/MgO(001), adsorption of impinging molecules at the steps is efficient, as supported by Fig. 6.3(d). At higher coverages, we expect that the steps will firstly be saturated before the molecules occupy the flat terraces, which may hamper the formation of highly ordered structures on these terraces.

6.4 Conclusion

Using XRD and STM, we have investigated the structural properties and local molecular ordering of C_{60} grown on epitaxial Fe/MgO(001). XRD analysis of 100 nm thick C_{60} molecular films shows that a strongly (111)-textured layer is obtained when growth is carried out at elevated temperature (100 °C). No long-range in-plane structural order could be detected in these 100 nm thick films. In contrast, STM measurements show that C_{60} forms a highly ordered monolayer on Fe(001). The molecules are arranged in a quasi-hexagonal pattern that superficially resembles the (111) plane of bulk fcc C_{60} but shows a considerable lattice mismatch with that structure. Most probably, this mismatch prevents epitaxial overgrowth of C_{60} films, consistent with our XRD measurements. It should be pointed out, however, that in-plane structural order might persist for ultrathin films. The (spin-dependent) electronic hybridization effects that we have discussed in Chapters 4 and 5for interfaces between C_{60} and Fe(001) result in strong interfacial interactions, which in turn have a profound impact on the growth mechanism in this hybrid system. Furthermore, STM measurements of MLs prepared under different conditions underline the important role of the kinetics of the adsorbed C_{60} molecules on the Fe surface in defining the structural properties of the first layer. The highly ordered surface structures are interesting within the context of spin polarized charge transport across the interface, since the well-defined molecular arrangement allows for direct comparison with theory (see Chapter 5). We expect that spin transport experiments on systems involving C_{60}/Fe(001) interfaces, and/or

similarly well- defined and well characterized interfaces, will generate important information for the further development of organic spintronic devices.

References

1. Z. H. Xiong, D. Wu, Z.V. Vardeny and J. Shi, Nature **427**, 821 (2004).
2. T. S. Santos, J. S. Lee, P. Migdal, I. C. Lekshmi, B. Satpati and J. S. Moodera, Phys. Rev. Lett. **98** (1), 016601 (2007).
3. C. Barraud, P. Seneor, R. Mattana, S. Fusil, K. Bouzehouane, C. Deranlot, P. Graziosi, L. Hueso, I. Bergenti, V. Dediu, F. Petroff and A. Fert, Nature. Phys. **6** (8), 615 (2010).
4. V. Dediu, L. E. Hueso, I. Bergenti, A. Riminucci, F. Borgatti, P. Graziosi, C. Newby, F. Casoli, M. P. De Jong, C. Taliani and Y. Zhan, Phys. Rev. B **78** (11), 115203 (2008).
5. W. J. M. Naber, S. Faez and W. G. v. d. Wiel, J. Phys. D: Appl. Phys. **40**, R205 (2007).
6. V. A. Dediu, L. E. Hueso, I. Bergenti and C. Taliani, Nat. Mat. **8** (9), 707 (2009).
7. S. Yuasa, T. Nagahama, A. Fukushima, Y. Suzuki and K. Ando, Nat. Mater. **3** (12), 868 (2004).
8. P. Rudolf, M. S. Golden and P. A. Bruhwiler, J. Electron Spectrosc. and Relat. Phenom. **100**, 409 (1999).
9. T. L. A. Tran, P. K. J. Wong, M. P. de Jong, W. G. van der Wiel, Y. Q. Zhan and M. Fahlman, Appl. Phys. Lett. **98**, 222505 (2011).
10. A. J. Maxwell, P. A. Brühwiler, D. Arvanitis, J. Hasselström, M. K. J. Johansson and N. Mårtensson, Phys. Rev. B **57** (12), 7312 (1998).
11. M. Abel, A. Dmitriev, R. Fasel, N. Lin, J. V. Barth and K. Kern, Phys. Rev. B **67** (24), 245407 (2003).
12. C. H. Lin, K. C. Lin, T. B. Tang and W. W. Pai, J. Nanosci. Nanotechno. **8** (2), 602 (2008).
13. C. Elschner, A. A. Levin, L. Wilde, J. Grenzer, C. Schroer, K. Leo and M. Riede, J. Appl. Cryst. **44**, 983 (2011).
14. J. G. Hou, J. Zeng, Y. Q. Li and Z. Q. Wu, Thin Solid Films **320** (2), 179 (1998).

15. V. M. Kaganer, R. Kohler, M. Schmidbauer, R. Opitz and B. Jenichen, Phys. Rev. B **55** (3), 1793 (1997).
16. C. Boubeta, J. Costa-Kramer and A. Cebollada, J. Phys-Condens. Mater. **15**, R1123 (2003).
17. J. F. Lawler, R. Schad, S. Jordan and H. van Kempen, J. Magn. Magn. Mater. **165** (1-3), 224 (1997).
18. B. Wassermann, Phi. Mag. **83** (16), 1929 (2003).
19. M. R. C. Hunt, S. Modesti, P. Rudolf and R. E. Palmer, Phys. Rev. B **51** (15), 10039 (1995).
20. J. K. Gimzewski, S. Modesti and R. R. Schlittler, Phys. Rev. Lett. **72** (7), 1036 (1994).
21. M. Sakurai, H. Tada, K. Saiki and A. Koma, Jpn. J.of Appl.Phys. **30** (11A), L1892 (1991).
22. S. Javaid, M. Bowen, S. Boukari, L. Joly, J. B. Beaufrand, X. Chen, Y. J. Dappe, F. Scheurer, J. P. Kappler, J. Arabski, W. Wulfhekel, M. Alouani and E. Beaurepaire, Phys. Rev. Lett. **105** (7), 077201 (2010).
23. N. Atodiresei, J. Brede, P. Lazić, V. Caciuc, G. Hoffmann, R. Wiesendanger and S. Blügel, Phys. Rev. Lett. **105** (6), 066601 (2010).
24. Y. R. M. Weser, K. Horn, M. Sicot, M. Fonin et al., Appl. Phys. Lett. **96**, 012504 (2010).
25. J. T. Sadowski, R. Z. Bakhtizin, A. I. Oreshkin, T. Nishihara, A. Al-Mahboob, Y. Fujikawa, K. Nakajima and T. Sakurai, Surf. Sci. **601** (23), L136 (2007).

SUMMARY

Carbon-based materials are promising for spintronic applications due to the weak spin-orbit coupling in these materials, potentially providing a long spin life time. An additional advantage is that organic materials exhibit non-critical requirements for high quality interface formation and film growth on various substrates. The research described in this thesis focuses on spin polarized transport through thin films of C_{60} fullerene molecules in vertical spin valves, spin polarized hybridization effects at C_{60}/bcc-Fe(001) interfaces, and the ordering of C_{60} molecules on epitaxial bcc-Fe(001) thin films.

Chapter 1 gives an overview of recent progress on spintronics, including an introduction of the main concepts and challenges for semiconductor-based spintronic devices. Subsequently, the selection of appropriate carbon-based materials (including C_{60} fullerenes) for spintronic applications, and the advantages of using well-defined interfaces in organic spin valves are discussed.

Chapter 2 provides a description of the major experimental methods used in this thesis work, including fabrication techniques, magnetotransport measurement tools, materials characterization tools, and synchrotron radiation techniques.

Chapter 3 of this thesis deals with spin polarized transport in C_{60}-based spin valves (vertical Co/Al_2O_3/C_{60}/NiFe junctions), studied by both experiments and modelling. The experimental results have been interpreted using a model based on a superposition of direct- and multi-step tunnelling via a Gaussian density of intermediate states in the C_{60} layer. We find that, analogous to conductivity mismatch in the diffusive regime, the junction magnetoresistance (JMR) drops continuously as the amount of intermediate tunnelling steps increases, regardless of the spin lifetime and spin diffusion length. In addition to the intrinsic loss of the JMR due to multi-step tunnelling, our temperature- and bias dependent measurements of the magnetotransport properties indicate that spin relaxation and dephasing in the intermediate states on the C_{60} molecules also affect the JMR. We

propose that a possible mechanism that underlies this is spin precession in the inhomogeneous magnetostatic fields that arise from finite roughness at the ferromagnetic interfaces, which is supported by measurements of JMR versus magnetic field, recorded at different bias voltages.

The electronic and magnetic properties of the interface between C_{60} molecules and a Fe(001) surface are described in chapter 4. Photoemission spectroscopy (PES) and C K-edge X-ray absorption spectroscopy (XAS) show charge transfer from the Fe substrate to C_{60} molecules, and strong interfacial bonding between C_{60} and Fe (in case of a monolayer C_{60} on Fe). The mixing between C_{60} $\pi(\pi^*)$ orbitals and Fe 3*d* wave functions leads to a distinct, oscillatory magnetic moment (changing sign for different states) of C_{60}-derived interfacial electronic states, as is evident from C K-edge x-ray magnetic circular dichroism (XMCD) spectra. The oscillatory nature of the polarization of these states close to E_F is important in the light of spin-polarized charge injection across the interface. Hybridization between the frontier orbitals of C_{60} and Fe 3d states has a strong effect on the spin polarization of the interface, which underlines the potential of chemical tuning of the organic semiconductor/ferromagnetic "spinterface" for spintronic devices.

In chapter 5 of this thesis, a combined computational (density functional theory) and experimental (XMCD) study on the magnetic properties of interfaces between bcc-Fe(001) and C_{60} molecules is presented. To study the magnetic moments of Fe surface atoms at C_{60}/bcc-Fe(001) interfaces, we used ultrathin Fe layers, consisting of three Fe monolayers (MLs) deposited onto a W(001) surface, to avoid the significant contribution of Fe bulk atoms to the XAS yield at the Fe $L_{2,3}$-edge. The calculations show (i) that the hybrid interface states lead to magnetic moments on the C_{60} molecules that are coupled antiparallel to the Fe moments, and (ii) that the adsorption of C_{60} on Fe(001) reduces the magnetic moment of the top Fe layer by ~6%. XMCD experiments of 3 MLs of Fe on W(001) show that the overall Fe spin moment reduces by 6% after adsorption of C_{60}. This is in good agreement with the calculated values for both C_{60}/Fe(001) and C_{60}/Fe/W(001), which show a similar spin-dependent electronic structure at the hybrid interfaces, in spite of their significant structural differences.

In chapter 6, we describe studies of the crystallinity and molecular ordering of C_{60} films on epitaxial Fe/MgO(001) surfaces, using X-ray diffraction (XRD) and

scanning tunnelling microscopy (STM). XRD analysis of 100 nm thick C_{60} molecular films shows that a strongly (111)-textured layer is obtained when growth is carried out at elevated temperature (100 °C). No long-range in-plane structural order could be detected in these 100 nm thick films. In contrast, STM measurements show that C_{60} forms a highly ordered monolayer on Fe(001). The molecules are arranged in a quasi-hexagonal pattern that superficially resembles the (111) plane of bulk fcc C_{60} but shows a considerable lattice mismatch with that structure. The C_{60} monolayers exhibit quasi-hexagonal arrangements on the Fe(001) surface oriented along the [100] and [010] directions. The highly ordered surface structures are interesting within the context of spin polarized charge transport across the interface, since the well-defined molecular arrangement allows for direct comparison with theory.

In conclusion, spin polarized transport in C_{60}-based vertical spin valves and the magnetic polarization at C_{60}/ferromagnetic interfaces were studied. Significant understanding of the physics of C_{60}-based vertical spin valves has been generated, however certain aspects such as the determination of spin relaxation length and -time require further study. The realization of well-defined interfaces in devices is also required to fulfill the potential of organic/carbon based materials for spintronic applications.

SAMENVATTING

Op koolstof gebaseerde materialen zijn veelbelovend voor spintronica vanwege de zwakke spin-baan wisselwerking, waardoor de spin-levensduur naar verwachting lang zal zijn. Een bijkomend voordeel is dat de condities voor het vormen van kwalitatief goede grensvlakken en dunne films op verschillende substraten niet kritisch zijn. Het onderzoek dat in dit proefschrift beschreven wordt richt zich op spingepolariseerd ladingstransport door dunne films bestaande uit C_{60} moleculen in verticale "spin valves", spingepolariseerde hybridisatie-effecten aan C_{60}/bcc-Fe(001) grensvlakken, en de manier waarop C_{60} moleculen zich ordenen op epitaxiale bcc-Fe(001) dunne films.

Hoofdstuk 1 geeft een overzicht van de recente ontwikkelingen in de spintronica, waaronder een inleiding van de belangrijkste concepten en uitdagingen voor op halfgeleiders gebaseerde spintronica. Vervolgens wordt de selectie van geschikte op koolstof gebaseerde materialen voor spintronica-toepassingen bediscussieerd, alsmede de voordelen van het gebruiken van goed gedefinieerde grensvlakken in organische spin valves.

Hoofdstuk 2 beschrijft de belangrijkste experimentele technieken die in dit werk worden gebruikt, zoals fabricagetechnieken, magnetotransportmetingen, karakterisatie van materialen, en technieken die gebruik maken van synchrotronstraling.

Hoofdstuk 3 van dit proefschrift richt zich op spingepolariseerd ladingstransport in op C_{60} gebaseerde spin valves (verticale Co/Al_2O_3/C_{60}/NiFe juncties), bestudeerd met experimenten en modellering. De experimentele resultaten zijn geïnterpreteerd met een model gebaseerd op een superpositie van directe- en meerstapstunneling van elektronen via een Gaussische toestandsdichtheid in de C_{60}-laag. We vinden dat, in analogie met het concept "conductivity mismatch" bij diffusief transport, de magnetoweerstand van de juncties (JMR) afvalt als het aantal tunnelingstappen toeneemt, ongeacht de spinlevensduur of spindiffusielengte. Naast dit intrinsieke verlies van de JMR door meerstapstunneling, laten onze metingen van de temperatuurs- en

spanningsafhankelijkheid van de magnetoweerstand zien dat spin-relaxatie in de tussentoestanden in de C_{60}-laag ook een rol speelt. We stellen een mogelijk mechanisme dat hieraan ten grondslag ligt voor, namelijk de precessie van spins in het inhomogene magnetische veld dat wordt veroorzaakt door de ruwheid aan de ferromagnetische grensvlakken. Dit wordt ondersteund door metingen van de JMR versus het magneetveld, gedaan bij verschillende spanningen over de juncties.

De elektronische en magnetische eigenschappen van het grensvlak tussen C_{60}-moleculen en een Fe(001)-oppervlak zijn beschreven in hoofdstuk 4. Photoemission spectroscopy (PES) en C K-edge X-ray absorption spectroscopy (XAS) laten zien dat er ladingsoverdracht plaatsvindt van het Fe-substraat naar de C_{60}-moleculen, die sterk worden gebonden aan het Fe-oppervlak (in het geval van een monolaag C_{60} op Fe). De hybridisatie van C_{60} $\pi(\pi^*)$ en Fe-3*d*-golffuncties leidt tot een kenmerkend, oscillerend magnetisch moment (van teken wisselend voor verschillende toestanden) voor toestanden op het C_{60}-molecuul. Dit is aangetoond met C K-edge x-ray magnetic circular dichroism (XMCD) metingen. Het oscillerende gedrag van de polarisatie van deze toestanden dichtbij E_F heeft belangrijke consequenties voor spingepolariseerde ladingsinjectie aan het grensvlak. De hybridisatie van de orbitalen van de C_{60}moleculen met de 3d-toestanden van Fe heeft een sterk effect op de spinpolarisatie aan het grensvlak, hetgeen het potentieel van chemische beïnvloeding van "spinterfaces" (spingepolariseerde grensvlakken) tussen organische halfgeleiders en ferromagnetische metalen onderschrijft.

In hoofdstuk 5 van dit proefschrift wordt een gecombineerde studie door middel van berekeningen (density functional theory) en experimenten (XMCD) aan de magnetische eigenschappen van grensvlakken tussen bcc-Fe(001) en C_{60} moleculen gepresenteerd. Om de magnetische momenten van Fe-oppervlakte-atomen aan C_{60}/bcc-Fe(001) grensvlakken te kunnen bestuderen, gebruikten we extreem dunne Fe-lagen, bestaande uit drie monolagen Fe gedeponeerd op een W(001)-oppervlak. Dit om de significante bijdrage van bulk Fe-atomen aan de XAS opbrengst aan de Fe $L_{2,3}$-edge te vermijden. De berekeningen laten zien dat (i) de hybridisatie van toestanden aan het grensvlak leidt tot magnetische momenten op C_{60}-moleculen die antiparallel zijn ten opzichte van de Fe-momenten, en (ii) dat de adsorptie van C_{60}-moleculen het magnetisch moment van de Fe-toplaag reduceert met 6%. XMCD metingen aan 3 monolagen Fe op W(001) laten zien dat het gemiddelde spinmagnetisch moment van Fe afneemt met 6% na

adsorptie van C_{60}. Dit komt goed overeen met de berekende waarden voor zowel C_{60}/Fe(001) als C_{60}/Fe/W(001), waarvoor de spingepolariseerde elektronenstructuren vergelijkbaar zijn, ondanks de significante verschillen in de structuur.

In hoofdstuk 6, beschrijven we de kristalliniteit en moleculaire ordening van C_{60}-films op epitaxiale Fe/MgO-oppervlakken, bestudeerd met X-ray diffraction (XRD) en scanning tunnelling microscopy (STM). XRD metingen aan een C_{60}-film van 100 nm tonen een sterke (111)-textuur aan als de groei wordt uitgevoerd bij verhoogde temperatuur (100 °C). Ordening in het vlak van de film wordt niet waargenomen voor deze 100 nm films. In contrast hiermee, laten STM-metingen zien dat C_{60}-moleculen een goed-geordende monolaag vormen op Fe(001). De moleculen zijn gerangschikt in een quasihexagonaal patroon, dat een oppervlakkige gelijkenis vertoont met het (111)-vlak van bulk fcc C_{60}, maar dat aanzienlijk van deze structuur afwijkt. De quasi hexagonale C_{60} patronen zijn langs de [100] en [010] kristalrichtingen georiënteerd. Deze sterk geordende oppervlaktestructuren zijn interessant in de context van spin gepolariseerd ladingstransport door het grensvlak, omdat een directe vergelijking met theorie mogelijk is.

Concluderend: we bestudeerden spingepolariseerd ladingstransport in verticale spin valves gebaseerd op C_{60}, alsmede de magnetische polarisatie van C_{60}/ferromagnetische-grensvlakken. Hierbij is begrip van de fysische werking van de spin valves verkregen, hoewel aspecten als spinrelaxatielengte en spinlevensduur verdere studies behoeven. De realisatie van goed-gedefinieerde grensvlakken in devices is belangrijk om het potentieel van organische/op-koolstof-gebaseerde halfgeleiders voor spintronica tot bloei te laten komen.

ACKNOWLEDGEMENTS

This doctoral thesis could not have been completed without contributions and supports from many people around me, to some of whom it is possible to give particular mention here.

First and foremost, I wish to thank my daily supervisor and assistant promotor, Dr. Michel de Jong. Thank you very much for giving me the chance to work in your interesting research project. With your enthusiastic guidance, valuable suggestions and appreciation, I have become more confident and motivated in my studies. With all my respect, I would like to share that you are an example of "super" scientist, you have not only deep knowledge in many scientific aspects but also show an excellent engineer. In four years of my PhD, there have been four times I travelled with you to Sweden for X-ray adsorption measurements, thank for your enthusiasm, inspiring ideas and awesome technical skills, we got a reasonable number of publications afterwards and some parts of results were to put in this thesis. Dear Michel, I really appreciate your supports during last few months of my PhD. Your intensive reading and critical comments and corrections on every part of my thesis helped me to complete and increase the quality of this work. I would like to thank you again for translating my Summary into Samenvatting. Working with you is my great pleasure, I enjoyed very much during the last four years.

I would like to acknowledge my supervisor and promotor, Prof. Wilfred van der Wiel for giving me a great opportunity to carry out research in NanoElectronics (NE) group and the support for my graduation. Dear Wilfred, thank you very much for your valuable advices, thoughtful guidance, warm encouragement and motivation in each and every stage of my PhD.

I would like to thank Prof. A.J. Mouthaan, Prof. E.J. ten Elshof, Prof. A. Brinkman, and Prof. B. Koopmans, the members of my doctoral graduation committee who have taken time out of their busy schedules to evaluate this work, specially to Prof. L.E. Hueso who travelling from abroad.

I would like to express my sincere thanks to Dr. D. Çakır (Computational Materials Science group) for the calculation model in Chapter 5 and Dr. Johnny Wong for STM data in Chapter 6 of this thesis. Dear Johnny W, thank you very much for handling of our manuscript to finish and sent to Michel (de Jong) for correction during my maternity leave. Without your and Michel's help, our results could not be published and then finish my PhD thesis in time. I also enjoyed working with you in Sweden. We were there together three times, each time we spent one week for doing experiment from morning to the next morning. Luckily, you are very good at cooking that's why we all survived. The XRD measurements in Chapter 6 were carried out by Mr. Peter Brinks (IMS group), thank you very much for your cooperation and wish you success in your PhD project. Mr. Kai Wang, thank you for all your help during the last year of my PhD and wish you to be very fruitful with your research project.

I have got great technical supports from many people during 4 years. I am grateful to Johnny Sanderink for his kind training in operating MBE and helping me when I faced problems with friendly smile. I am thankful to Thijs Bolhuis for all his supports and guidance in magneto transport measurements, VSM and computer software. Thanks Martin Siekman for his help on AFM measurements. I would like to extend my sincere thanks to other technical staffs in NanoLab and cleanroom for their technical support: Rico Keim (for TEM image), Gerard Kip (for XPS measurements). I would like to thank Hans Mertens, Robert Wijn, Samantha and Marion for their training and help in clean room.

Tu Quyen Le did her master thesis under my daily supervision. Quyen, thank you very much for your hard work in the low temperature transport measurements and data analyses. Fabrication of devices are difficult but characterization their properties are even harder and very time consuming. Thank you very much for your contribution in Chapter 3 of this thesis. I wish you all good luck in the US.

Janine and Elmer, thank you very much for being my paranymphs. Janine, thanks for our friendship since you joined lab course with me, also during your master thesis and now we are both doing PhD at NE. Good luck with your project. I want to thank Elmer again for your translation my Dutch letters and correction Dutch errors on my Samenvatting. Thank Serkan (my former office mate) for

helping me with the design of my thesis cover. Thank Michel (Zoontjes) for being my Dutch translator and preparing SiO_2 wafers for me. Thanks to my (former) office mates, Yunjae, Wouter, Ina, Elia, Kai, Bojian, Frank and Rabindra (Robin) for sharing your thought and for all the fun we have had together. Robin, thank you very much for your help on my propositions. Thanks Frank for translating Dutch letters (you came to our office just in time when Elmer and Michel (Zoontjes) moved their office far away from me). I am also grateful to all other (former) members of NE groups for their supports and accompany during travelling to conferences, coffee breaks and NE events: Floris, Tian, Derya, Saurabh, Ksenia, Peter (Eerkes), Zhihua, Matthias, Liang Du, Filipp, Chris, Joost (Ridderbos), Dilu, Frans, Wen, Maarten, Mostafa, Bernarduz, Shahina, Jelle, Koert, Sajor, Sandeep, Lucky, Joost (Hoff), Zelmer, Jean-Christophe, and Ivan Marun. I wish all of you happy and success.

I would like to take this opportunity to sincere thanks to NE (former) secretaries: Carolien, Joyce, Susan and Karen, HR assistant of EWI: Odette Scholten and Ine Buter-Snijder, and staffs in international employee office: Cecile and Ellen for helping me with administrative procedures.

I gratefully acknowledge the financial support from the European project MINOTOR, the European Research Council and the NOW VIDI program.

During these years, I have made many friends who helped me a very pleasant social life. First of all, I would like to thank Dr. Duc Minh Nguyen, a big brother in MESA+, for his advice on social life and useful discussion on research topics whenever we had coffee together. I would like to thank Hao and Loan for letting their daughter, Phuong Anh to play and teach Du with English and Maths after school time. Thank you Phuong Anh very much, your parents must be proud of you. Thanks Hao again for checking errors on my thesis at last minutes. I will never forget the help from Tan- Dao, our neighbours, for their unconditional help on the day I delivered my daughter. Tan-Dao, we promised to be parents of Dieu Le and Gia Khang. Chau Hoang, thank you for making cakes at every our family occasions and for spending time together in the garden in many late evenings. Thanks Tram Nguyen for looking after our daughter in the last month of your stay in Netherlands, we all miss you. I would like to extend my thanks to anh Ha and

chi Hanh for picking me up form airport, cooking delicious meals when I came to the Netherlands for the PhD interview.

Last but not least, I would like to thank all other my Vietnamese friends in Twente for their friendship, supports and for all parties we have joined at many weekends and occasions. Good luck to all of you: So Pham, anh Hien, anh Phong, chi Giang, Tuan Nguyen, Huong Nguyen, Trang Pham, Viet Anh, Viet Duc, Tuan Tran, Hieu Vu, Son Nguyen, Hang Nguyen, Tuan Zin, Bach Le, Anh Van, Minh Hanh, Dung, Giang.

I would like to thank all my big-family members: my uncles, my aunts, my cousin, my brother, my brothers in law, sisters in law, my nephews and my nieces for their supports and encouragement. Special thanks to my youngest brother in law, Huấn for visiting us in Netherlands last few months.

I would like to thank all my friends, who I might have forgotten to mention in this thesis.

This thesis is dedicated to my parents Trần Văn Thắng and Phan Thị Đào, and my parents in law Nguyễn Huệ and Vương Thị Hiền, for their unconditional support and endless love.

Bố mẹ kính mến

Sau khi trở về từ Hàn quốc chưa được bao lâu, nỗi nhớ mong chưa thỏa thì chúng con lại khăn gói lên đường sang Hà Lan. Cảm ơn bố mẹ đã yêu thương, tin tưởng và khích lệ con tiếp tục con đường khoa học. Lần này con đã trưởng thành hơn và bên cạnh con có chồng và con trai yêu, con không còn cảm thấy cô đơn như những năm về trước. Con biết 4 năm qua bố mẹ vẫn luôn luôn lo lắng cho cuộc sống chúng con nhiều lắm, nhất là lúc con sinh con bên này chỉ một mình chồng con chăm sóc. Giờ thì các con của chúng con đang lớn dần trong bàn tay của bố mẹ, và con đã hoàn thành luận văn tiến sỹ của mình. Với tất cả sự thành kính của mình, con muốn dành tặng bố mẹ tất cả những lời yêu thương này.

This thesis is dedicated to my husband Tiến Hành and our children Du (Tôm) and Diệu Lê (Tép) who have always stood by me, dealt with all my absence from many occasions with a smile.

Chồng yêu,

Em cảm ơn anh vì đã hi sinh bao năm cho em và các con. Anh bảo có anh bên cạnh em đã thành công hơn nhiều, em hiểu em thành công hơn thì cũng đồng nghĩa là anh đã phải hi sinh nhiều hơn.

Tôm và Tép, cảm ơn hai con của mẹ đã ngoan ngoãn và khỏe mạnh, vui vẻ bên cạnh bố nhưng lúc mẹ vắng nhà. Các con là động lực lớn nhất giúp bố mẹ nỗ lực để vượt qua mọi khó khăn trong cuộc sống.

This thesis is dedicated to my younger sister who is gazing at me in other world.

Enschede, November 2013

Lan Anh

LIST OF PUBLICATIONS

This thesis is based on the publications:

The multi-step tunneling analogue of conductivity mismatch in organic spin valves
T.L.A. Tran, T.Q. Le, J.G.M. Sanderink, W.G. van der Wiel, and M. P. de Jong
Adv. Funct. Mater. 22, 1180 (2012) (chapter 3)

Hybridization-induced oscillatory magnetic polarization of C_{60}-orbitals at the C_{60}/Fe(001)interface
T.L.A. Tran, P.K.J. Wong, M.P. de Jong, W. G. van der Wiel, Y. Q. Zhan, and M. Fahlman

Appl. Phys. Lett. 98, 222505 (2011) (chapter 4)

Magnetic properties of bcc-Fe(001)/C_{60} interfaces for organic spintronics
T.L.A. Tran, D. Çakır, P.K.J. Wong, A.B. Preobrajenski, G. Brocks, W.G. van der Wiel, and M.P. de Jong
ACS Appl. Mater. Interfaces 5, 837 (2013) (chapter 5)

Highly ordered C_{60} films on epitaxial Fe/MgO(001) surfaces for organic spintronics
P. K. J. Wong, **T.L.A. Tran**, P. Brinks, W.G. van der Wiel, M. Huijben, and M.P. de Jong
Org. Electron. 14, 451 (2013) (chapter 6)

Other publications:

Tunneling anisotropic magnetoresistance in Co/AlO_x/Al tunnel junctions with fcc Co (111) electrodes
K. Wang, **T.L.A. Tran**, P. Brinks, J.G.M. Sanderink, T. Bolhuis, W. G. van der Wiel and M.P. de Jong*
Phys. Rev. B 88, 054407 (2013).

Crystalline CoFeB/Graphite Interfaces for Carbon Spintronics Fabricated by Solid Phase Epitaxy
P. K. Johnny Wong, Wen Zhang, **T. Lan Anh Tran**, Anton A. Starikov, Johnny G. M. Sanderink, Martin H. Siekman, Geerts Brocks, Paul J. Kelly, Wilfred G. van der Wiel, and Michel P. de Jong
Adv. Funct. Mater.23, 4933 (2013).

Magnetism in $Si_{1-x}Mn_x$ diluted magnetic semiconductor thin films
Tran Thi Lan Anh, Sang Soo Yu, Young Eon Ihm, Dojin Kim and Hyojin Kim,
Thin solid films, 518, 309 (2009)

Electrical and magnetic properties of Mn-doped Si thin films
T. T. Lan Anh, S. S. Yu, Y. E. Ihm, D. J. Kim, H. J. Kim and S. K. Hong,
Physica B, 404, 1686 (2009)

Magnetoresitance of $Si_{1-x}Mn_x$ semiconductor thin films grown by Molecular beam epitaxy
Tran Thi Lan Anh, Hyeong Kyu Lim, Byeong Choel Lee, Dong Hwi Kim, Kui Jong Baek, Young Eon Ihm, Dojin Kim, Hyojin Kim, Jin Hee Kim
Journal of the Korean Physics Society,55, 309(2009).

Magnetic and magneto transport properties of annealed amorphous $Ge_{1-x}Mn_x$ semiconductor thin films
Sang Soo Yu, **Tran Thi Lan Anh**, Young Eon Ihm, Dojin Kim, Hyojin Kim, Soon Ku Hong
IEEE NTC Review of advanced in micro, nano and molecular system.

Magneto-transport properties of amorphous $Ge_{1-x}Mn_x$ thin films
Sang Soo Yu, **Tran Thi Lan Anh**, Young Eon Ihm, Dojin Kim, Hyojin Kim, Soon Ku Hong, Sangjun Oh, Chang Soo Kim, Hwack Joo Lee, Byung Chill Woo,
Current Applied Physics, 6, 545 (2006).

Ferromagnetism in amorphous $Ge_{1-x}Mn_x$ grown by low temperature vapor deposition
Sang Soo Yu, **Tran Thi Lan Anh**, Young Eon Ihm, Dojin Kim, Hyojin Kim, Sangjun Oh, Chang Soo Kim, Hyun Ryu
Solid State Communications, 134 642 (2005).

Propositions accompanying the thesis

Spintronics using C_{60} fullerenes: Interfaces and devices by **Trần Thị Lan Anh**

1. Not spin relaxation, but the number of tunnelling steps is the main limiting factor for the magnetoresistance of C_{60}-based spin valves. (Chapter 3 of this thesis)

2. The presence of (local) stray magnetic fields due to the roughness at the C_{60}/ferromagnetic layer interface causes spin relaxation and dephasing in C_{60}-based spin vales. (Chapter 3 of this thesis)

3. To optimize the spin injection efficiency, the hybrid organic/ferromagnetic layer interface needs to be engineered and controlled in a such way that the spin-dependent states at the interface act as a spin filter. (Chapters 4 and 5 of this thesis)

4. Highly ordered adsorbed C_{60} monolayers on Fe surfaces are interesting in the context of spin-polarized transport through C_{60}/Fe interfaces. (Chapter 5 and 6 of this thesis)

5. Attempting to avoid snails from eating plants by simply increasing the number of plants in a garden is similar to attempting to let devices survive longer by just fabricating more and more devices in the same time period.

6. Energy exists in everything and everywhere.

7. The more plants you grow, the more you save the society from global warming.

8. Women need to work much harder than men to be equally successful in scientific research. (*Nature* **495,** 28-31(2013))

9. Men and women are equally responsible for the development of a nation.

These propositions are considered opposable and defendable and as such have been approved by the supervisor Prof. dr. ir. W. G. van der Wiel.